University of Milano
Physics department

Detection techniques
for the RICHs of LHCb

Candidate
Mario Alemi

Tutors:
Prof. Clara Matteuzzi

At CERN (The European Laboratory for Particle Physics) the Large Electron-Positron Collider LEP will be substituted by LHC: a Large Hadron Collider. It will be installed in the same tunnel, will collide proton beams with energies around 7-on-7 TeV with a nominal luminosity over the range $1 \Leftrightarrow 5 \cdot 10^{34} cm^{-2} s^{-1}$ or heavy ions such as lead with a total collision energy in excess of 1250 TeV/nucleus.

Four experiments will be installed around LHC: ATLAS (A Toroidal Lhc Apparatus), CMS (Compact Muon Solenoid), ALICE (A Large Ion Collider Experiment) and LHCb (the Large Hadron Collider Beauty experiment).

The present thesis will describe, after a brief introduction about the whole experiment LHCb and the physics motivations that have led to propose such a detector, the R&D work made on the RICH (Ring Imaging CHerenkov detector) of LHCb to which the author has participated to.

Contents

List of Figures

List of Tables

Chapter 1

An Experiment on CP Violation

1.1 What is LHCb?

LHCb[1] is a single-arm spectrometer with a forward angular coverage from approximately 10 mrad to 300 (250) mrad in the bending (non-bending) plane. The choice of the detector geometry is motivated by the fact that at high energies both the b- and $\overline{\text{b}}$-hadrons are predominantly produced in the same forward cone, a feature exploited in the flavour tag. This is demonstrated in Fig. 1.1 where the polar angles of the b- and $\overline{\text{b}}$-hadrons are plotted. The polar angle is defined with respect to the beam axis in the pp centre-of-mass system.

Figure 1.2 shows the momentum distributions for $B_d^0 \to \pi^+ \pi^-$ decays in the full angle of emission, and for those where the momenta of both pions are measured in the spectrometer. The decrease of the detector acceptance for high momenta is due to the loss of particles below 10 mrad. In the low momentum region, the loss of acceptance is due to slow pions that do not hit enough tracking stations for their momenta to be measured.

To determine the momentum range required for the spectrometer, the $B_s^0 \to D_s^- \pi^+$ decay is studied. The π^+ defines the high end of the momentum range, and the π^- from the D_s^- decay the low end. Figure 1.3 shows the momentum distributions for both pions, when they are within the spectrometer acceptance. Few tracks have momenta beyond 150 GeV/c.
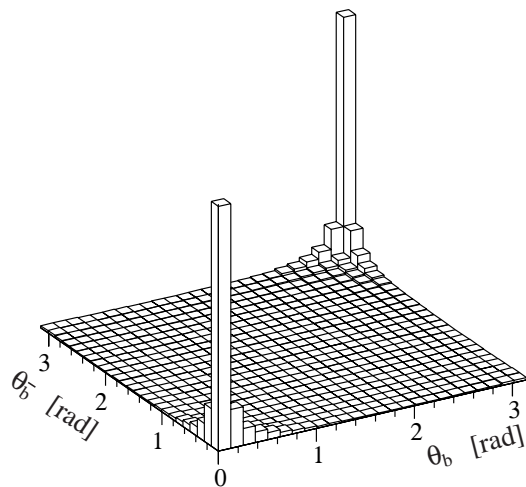
Figure 1.1: Polar angles of the b- and $\overline{\text{b}}$-hadrons calculated with the PYTHIA event generator[1].
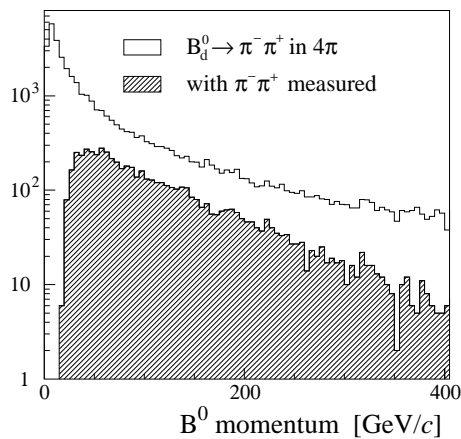
Figure 1.2: Momentum distributions for $B_d^0 \rightarrow \pi^+\pi^-$ decays in the full angle of emission, and for those where the momenta of both pions are measured in the spectrometer.[1]

1.2   Layout

The layout of the LHCb spectrometer is shown in Fig. 1.4. Intersection Point 8 of the collider, currently used by DELPHI, has been allocated to the
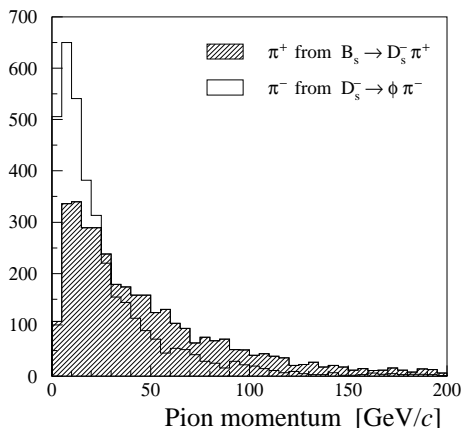
Figure 1.3: Momentum distributions for the π^+ from $B_s^0 \to D_s^- \pi^+$ decays and for the π^- from the subsequent D_s^- decay, where the momenta are measured in the spectrometer.[1]

experiment. A modification to the LHC optics, displacing the interaction point by 11.25 m from the centre, has permitted maximum use of the existing cavern by freeing 19.7 m for the LHCb detector components. A right-handed coordinate system is defined centred on the interaction point, with z along the beam axis and y pointing upwards and x toward the center of the ring.

LHCb comprises a vertex detector system, a tracking system, aerogel and gas RICH counters, an electromagnetic calorimeter with preshower detector, a hadron calorimeter and a muon filter.

A brief description of each subdetector is presented, except for the RICH's which will be discussed in more details in Chap. 3.

1.2.1 Magnet

The spectrometer dipole is placed close to the interaction region, in order to keep its size small. Since tracks in the vertex detector are used in the trigger, it is desirable to have the vertex detector in a region of no magnetic field for fast track finding. The first RICH counter is designed to cover the momentum range down to 1 GeV/c. To maintain the necessary RICH 1 acceptance and to avoid tracks bending in the gas radiator, RICH 1 is also required to be in a region of low magnetic field. The magnet is therefore placed downstream
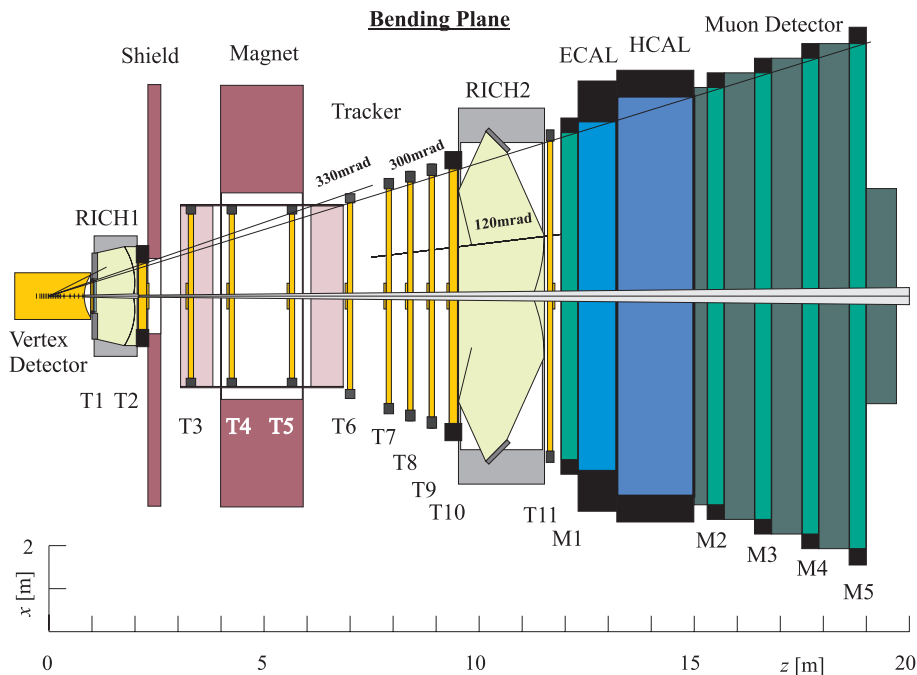
Figure 1.4: The LHCb detector seen from above (cut in the bending plane)[1].

of RICH 1, allowing an acceptance of 330 mrad in both projections upstream of the magnet.

A warm coil magnet is chosen to obtain a high field integral of 4 Tm with a short length. Figure 1.5 shows a schematic drawing of the magnet. The field is oriented vertically and has a maximum value of 1.1 T. The polarity of the field can be changed to reduce systematic errors in the CP-violation measurements that could result from a left-right asymmetry of the detector. The free aperture is 4.3 m horizontally and 3.6 m vertically. The coil is designed to maximise the field homogeneity. An iron shield upstream of the magnet is foreseen in order to reduce the stray field in the vicinity of the vertex detector and of RICH 1. In chapeter 6 is described a possible passive magnetic shielding for RICH 2.

1.2.2   Vertex detector system

The vertex detector system comprises a silicon vertex detector and a pile-up veto counter. The vertex detector has to provide precise information on the
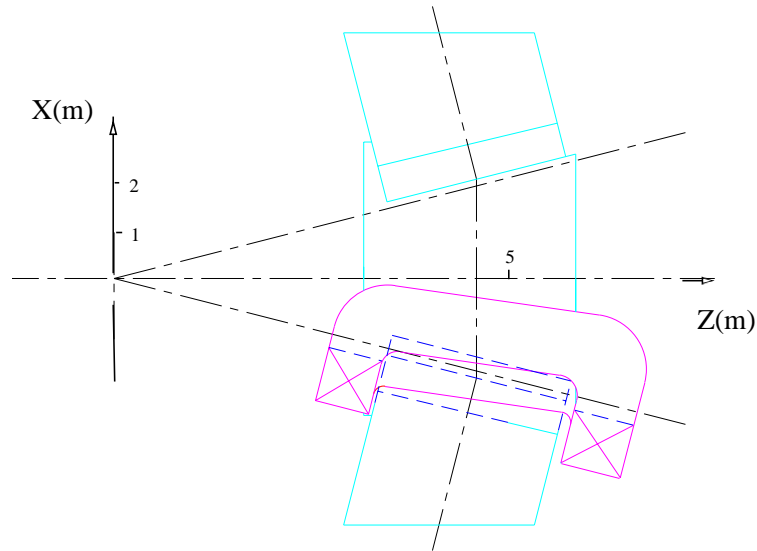
Figure 1.5: Schematic drawing of the warm coil magnet of LHCb (Jacques Andre, CERN).

production and decay vertices of b-hadrons both offline and for the level 1 trigger. The latter requires all channels to be read out within $1\,\mu$s. The pile-up veto counter is used in the level 0 trigger to suppress events containing multiple pp interactions in a single bunch-crossing, by counting the number of primary vertices.

1.2.3 Tracking system

The tracking system, consisting of Inner and Outer Tracker, provides efficient reconstruction and precise momentum measurement of charged tracks [4], track directions for ring reconstruction in the RICH, and information for the level 1 and higher level triggers.

The system comprises 11 stations (T1–T11 in Fig. 1.4) between the vertex detector and the calorimeters. Precise coordinates in the bending plane are obtained from straw tubes at $0°$ and $\pm5°$ with respect to the vertical. Stations immediately up- and downstream of the RICH counters contain additional planes, providing precise measurements in the non-bending plane (wires/strips along x).

The expected momentum resolution for the chosen design is approximately 0.3% for momenta from 5 to $200\,\mathrm{GeV}/c$, limited mainly by multiple scattering. Mass resolutions are good, e.g. $17\,\mathrm{MeV}/c^2$ for $\mathrm{B}_\mathrm{d}^0 \to \pi^+\pi^-$.

1.2.4   Calorimeters

The main purpose of the calorimeters is to provide identification of electrons and hadrons for trigger and offline analysis, with measurements of position and energy. The required level 0 trigger selectivity demands a longitudinal segmentation of the electromagnetic calorimeter (ECAL). The structure consists of a single-layer preshower detector followed by a Shashlik ECAL [2]. A scintillating-tile geometry is used for the hadron calorimeter (HCAL).

Acceptance and lateral detector segmentation of the three subsystems are geometrically matched to facilitate trigger formation. Polar acceptance starts at 30 mrad.

1.2.5   Muon detector

The Muon detector provides muon identification and level 0 trigger information. It consists of four stations M2–M5 embedded in an iron filter and a special station M1 in front of the calorimeter. The sizes of the logical pads (used for triggering and reconstruction) vary from $1\,\mathrm{cm} \times 2\,\mathrm{cm}$ to $8\,\mathrm{cm} \times 16\,\mathrm{cm}$. To reduce capacitive noise, the largest logical pads have to be formed by combining the information from four physical pads, each connected to a separate amplifier. Multigap Resistive Plate Chambers (MRPC's) are proposed for most of the coverage of M2–M5, where particle fluxes are below $5 \times 10^3\,\mathrm{cm}^{-2}\mathrm{s}^{-1}$. Station M1 and the inner regions of stations M2–M5 experience the highest fluxes and are therefore constructed with Cathode Pad Chambers (CPC's). These chambers extend down to 25 mrad in x and 15 mrad in y. The complete Muon Detector has 45,000 readout channels formed from 230,000 physical pads.

1.2.6   Front-end electronics

The subdetectors will use a common architecture for the front-end electronics [3], which has to accommodate the specific trigger requirements of LHCb, making maximum use of existing components. All analogue and digital signals arriving at 40 MHz will be stored in level 0 pipelined buffers, 128 cells

deep, to await the level 0 trigger decision taken after a fixed delay of $3.2\,\mu$s. Events accepted at an average rate of 1 MHz are transmitted to short derandomising buffers to avoid overflow due to limited output speed. The data are then multiplexed and digitised, if they were still analogue, and sent to level 1 buffers, 256 events deep, to allow up to $256\,\mu$s for the next trigger selection. The average rate of events accepted by level 1 is 40 kHz. Accepted events pass zero suppression and data formatting, are multiplexed and sent via the "front-end links" to the data acquisition system, located approximately 60 m from the detector.

The front-end electronics mounted inside the detector must be radiation hard or tolerant, the dose integrated over 10 years amounting to 0.2 Mrad at 30 cm. Part of the electronics, probably from the level 1 buffer onwards, will be mounted at least 4 m from the beam to permit standard components to be used.

Bibliography

[1] LHCb Technical Proposal.

[2] LHCb Note 96-08.

[3] LHCb Note 96-02.

[4] LHCb Notes 97-09 and 97-11.

Chapter 2

Some motivation

2.1 Introduction

CP violation is one of the central problems of subatomic-particle physics. Different B-factories are under operation around the world. Even if CP violation is known since many years, no clear explanation exists to improve the understanding of the effect in the Standard Model.

A subtle difference between the properties of particles and of antiparticles has been postulated (by Andrei Sakharov [1]) to have been responsible for the development, shortly after the Big Bang, of the excess of matter over antimatter from which the entire material universe has since evolved.

CP violation was first directly observed in neutral kaon decays in 1964 [2].

The Standard Model with three quark families can naturally generate CP violation in weak interaction.

Being the eigenstates of the strong Hamiltonian different from the eigenstates of the weak one, one can define a transformation matrix for these two bases. This matrix was introduced for six quarks by Kobayashi and Maskawa [3] and is called the Cabibbo-Kobayashi-Maskawa because one of the parameter was previously introduced by Cabibbo [4].

The idea of Cabibbo originated from needs to explain two phenomena:

- the transitions $u \leftrightarrow d$, $e \leftrightarrow \nu_e$, $\mu \leftrightarrow \nu_\mu$ had similar amplitudes.

- the transitions with variation of strangeness $\Delta S=1$ had amplitudes equal to 1/4 of those with $\Delta S=0$.

He proposed to consider the charged hadronic current as a sum of two currents, one with $\Delta S=1$, the other with $\Delta S=0$:

$$J_\mu^{Hadronic} = J_\mu^{\Delta S=0} cos\theta_c + J_\mu^{\Delta S=1} sin\theta_c \qquad (2.1)$$

where θ_c is called the Cabibbo angle. Equation 2.1 for a base of quark becomes:

$$J_\mu^{Quark} = \bar{u}\gamma_\mu(1 \Leftrightarrow \gamma_5)(d\ cos\theta_c + s\ sin\theta_c). \qquad (2.2)$$

A fourth quark was not foreseen by Cabibbo. But taking in account the existence of the *charm*, the Cabibbo angle can be seen as a mixing angle between two families of quark: *up* and *down*, *strange* and *charm*:

$$J_\mu^{Quark} = \bar{u}\gamma_\mu(1 \Leftrightarrow \gamma_5)d' + \bar{c}\gamma_\mu(1 \Leftrightarrow \gamma_5)s' \qquad (2.3)$$

where

$$d' = d\ cos\theta_c + s\ sin\theta_c \quad \text{and} \quad s' = \Leftrightarrow d\ sin\theta_c + s\ cos\theta_c. \qquad (2.4)$$

In 1973, one year before the discovery of the *charm*, the existence of a third family of quarks was introduced by Kobayashi and Maskawa in order to explain the CP-violation phenomena observed in the neutral-kaon system. This was an *ad hoc* hypothesis, because at that time no component of this third family was observed.

By introducing a mixing for the new family the parameters of the transformation matrix become four: three Eulero angles and one phase. It is this phase that can explain CP-violating phenomena in the neutral-kaon system. But other mechanisms has been proposed. Hence it is of great interest to study whether the pattern of CP-violating effects that can be observed in B decays follows the predictions of the minimal standard model, or instead requires the introduction of beyond Standard Model.

2.2   CP violation

By convention the mixing is defined for the fields *down, strange* and *beauty*:

$$V_{CKM} = \left(\begin{array}{ccc} V_{ud} & V_{us} & V_{ub} \\ V_{cd} & V_{cs} & V_{cb} \\ V_{td} & V_{ts} & V_{tb} \end{array} \right),$$

All the values V_{ij} can be determined by measuring the weak transition ij of the quarks through decays or by studing the neutrino inelastic scattering. Many parametrizations are possible, but the most convenient one is that proposed by Wolfenstein [5]:

$$V_{\mathrm{CKM}} \approx V_{\mathrm{CKM}}^{(3)} + \delta V_{\mathrm{CKM}}$$

where the expansion up to third order in λ is given by

$$V_{\mathrm{CKM}}^{(3)} = \begin{pmatrix} 1 - \lambda^2/2 & \lambda & A\lambda^3\left(\rho - i\,\eta\right) \\ -\lambda & 1 - \lambda^2/2 & A\lambda^2 \\ A\lambda^3\left(1 - \rho - i\,\eta\right) & -A\lambda^2 & 1 \end{pmatrix}.$$

The parameter λ is given by the sine of the Cabibbo angle, $\sin\theta_c$, measured to be 0.221 ± 0.002 [6] from decays involving s-quarks. $\eta \neq 0$ is required to generate CP violation.

For a qualitative discussion of CP violation in B-meson systems, $V_{\mathrm{CKM}}^{(3)}$ is sufficient and the second term δV_{CKM}, which is given by

$$\begin{pmatrix} 0 & 0 & 0 \\ -i\,A^2\lambda^5\eta & 0 & 0 \\ A\left(\rho + i\,\eta\right)\lambda^5/2 & \left(1/2 - \rho\right)A\lambda^4 - i\,A\lambda^4\eta & 0 \end{pmatrix},$$

is usually ignored. For CP violation in K^0-$\overline{\mathrm{K}}^0$ oscillations, the correction to V_{cd} is important. For B-meson systems, the correction to V_{td} and V_{ts} becomes relevant once the sensitivity of experiments to measure CP-violation parameters becomes 10^{-2} or less.

Six of the nine unitarity conditions of the CKM matrix can be drawn as triangles in the complex plane. The two triangles relevant for the B-meson systems are shown in Figure 2.1. The related unitarity conditions are given by

$$\begin{aligned} V_{\mathrm{ud}}V_{\mathrm{ub}}^* + V_{\mathrm{cd}}V_{\mathrm{cb}}^* + V_{\mathrm{td}}V_{\mathrm{tb}}^* &= 0 \\ V_{\mathrm{tb}}V_{\mathrm{ub}}^* + V_{\mathrm{ts}}V_{\mathrm{us}}^* + V_{\mathrm{td}}V_{\mathrm{ud}}^* &= 0. \end{aligned}$$

The two triangles become identical if δV_{CKM} is ignored. The angles of the triangles can be extracted either indirectly by measuring the lengths of the sides, or, within the Standard Model, directly from CP asymmetries. If the angles extracted by the two different methods disagree, this would indicate new physics.

Im $V_{ud}V_{ub}^* + V_{cd}V_{cb}^* + V_{td}V_{tb}^* = 0$

$\eta(1-\lambda^2/2)$

$\dfrac{(1-\lambda^2/2)V_{ub}^*}{\lambda\,/V_{cb}/}$

α

$\dfrac{V_{td}}{\lambda\,/V_{cb}/}$

γ

β

0      $\rho(1-\lambda^2/2)$ 1   Re

Im $V_{tb}V_{ub}^* + V_{ts}V_{us}^* + V_{td}V_{ud}^* = 0$

η

$\dfrac{V_{ub}^*}{\lambda\,/V_{cb}/}$

$\dfrac{(1-\lambda^2/2)V_{td}}{\lambda\,/V_{cb}/}$

$\eta\lambda^2$ γ'

$\delta\gamma$ $\dfrac{V_{ts}}{/V_{cb}/}$ Re

0   ρ $(1-\lambda^2/2+\rho\lambda^2)$
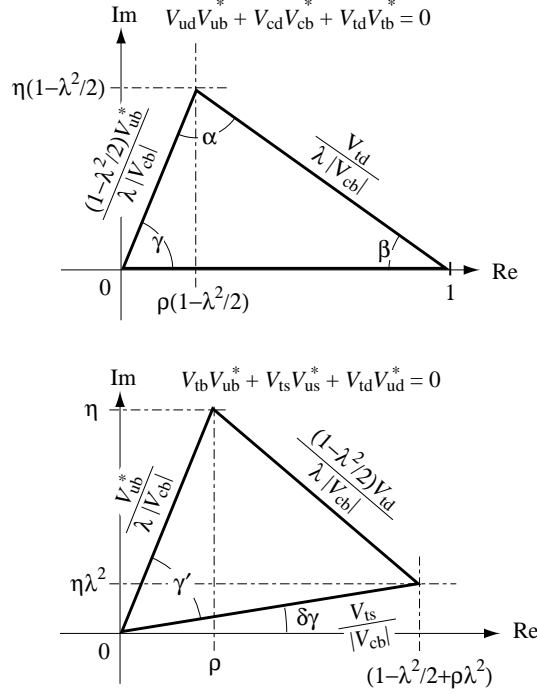
Figure 2.1: Two unitarity triangles in the Wolfenstein's parameterisation with an approximation valid up to $\mathcal{O}(\lambda^5)$.

Since λ is well known, the two triangles are completely determined by ρ and η, which can be derived from $|V_{cb}|$, $|V_{ub}|$ and $|V_{td}|$, as seen from Figure 2.1. The parameter A is extracted from measurements of $|V_{cb}|$ and λ. Values of $|V_{cb}|$ and $|V_{ub}|$ are extracted from various B-meson decays and are currently known to be 0.0395 ± 0.0017 and $0.0033 \pm 0.0004_{stat} \pm 0.0007_{syst}$ [6], respectively. The large error on $|V_{ub}|$ is due to the limited experimental data available and theoretical uncertainties in the evaluation of strong interaction effects. Experiments at e^+e^- machines running at the $\Upsilon(4S)$, i.e. CLEO, BABAR and BELLE, will reduce the errors on these elements. Their precision will ultimately be limited by the theoretical uncertainties.

The value of $|V_{td}|$ is currently determined from the frequency of B_d^0-$\overline{B}_d^0$ oscillations. Due to difficulties in evaluating the effects of hadronic interactions, the extracted value has a large uncertainty, $|V_{td}| = 0.009 \pm 0.003$ [6]. This situation can be improved considerably once $|V_{ts}|$ is extracted from the frequency of B_s^0-$\overline{B}_s^0$ oscillations and $|V_{td}/V_{ts}|$ is used instead of $|V_{td}|$, since the

Standard Model calculation of this ratio has a much reduced hadronic uncertainty. Experimentally, CDF, D0, HERA-B, SLD and LEP experiments are trying to measure the B_s^0-$\overline{B}_s^0$ oscillation frequency. However, this may not be possible before LHCb becomes operational, if the frequency is high.

Once ρ and η are derived from $|V_{cb}|$, $|V_{ub}|$ and $|V_{td}|$, the angles α, β, γ and $\delta\gamma$ can be calculated. At present, a non-zero value of η can only be obtained if CP violation in K^0-$\overline{K}^0$ oscillations is included in the analysis [7]. Future rare kaon decay experiments measuring $K \rightarrow \pi\nu\overline{\nu}$ will also provide information on ρ and η [8].

In the framework of the Standard Model, direct measurements can be made of the angles α, β, γ and $\delta\gamma$, or their combinations, from CP asymmetries in different final states of B-meson decays. Well known examples are [8]:

1. $\beta + \gamma$ from $B_d^0 \rightarrow \pi^+\pi^-$

2. β from $B_d^0 \rightarrow J/\psi K_S$

3. $\gamma \Leftrightarrow 2\delta\gamma$ from $B_s^0 \rightarrow D_s^\pm K^\mp$

4. $\delta\gamma$ from $B_s^0 \rightarrow J/\psi\phi$

5. γ from $B_d^0 \rightarrow \overline{D}^0 K^{*0}, D^0 K^{*0}, D_1 K^{*0}$,

where it is understood that the charge-conjugated decay processes are also measured, and D_1 is the CP $= +1$ state of the neutral D meson. The angle α is not measured directly but can be determined only through the triangle relation $\alpha = \pi \Leftrightarrow \beta \Leftrightarrow \gamma$. Within the framework of the Standard Model, β, $\gamma \Leftrightarrow 2\delta\gamma$ and γ measured from the decay channels 2, 3 and 5 have very little theoretical uncertainty.

If a new flavour-changing neutral current is introduced by physics beyond the Standard Model, it can have a large effect on B_d^0-$\overline{B}_d^0$ and B_s^0-$\overline{B}_s^0$ oscillations, since the contribution of the weak interaction is of second order. For such a case, the values of $|V_{td}|$ and $|V_{ts}|$ experimentally extracted from B-$\overline{B}$ oscillations no longer correspond to their real values. The angles $\beta + \gamma$, β, $\gamma \Leftrightarrow 2\delta\gamma$ and $\delta\gamma$, extracted from the decay channels 1–4, are also affected. These angles, measured in the two ways explained above, will no longer agree.

A disagreement between the value of γ deduced by channels 1 and 2 through B_d^0 decays and the one deduced by channels 3 and 4 through B_s^0

should give an indication of this new flavour-changing neutral current. That is because B_d^0-$\overline{B}_d^0$ and B_s^0-$\overline{B}_s^0$ oscillations can be affected differently by the new flavour-changing neutral current.

In the Standard Model, $\delta\gamma$ is expected to be of the order of 10^{-2}, and the CP asymmetry in $B_s^0 \rightarrow J/\psi\phi$ decays very small. A new flavour-changing neutral current could, however, generate a large CP-violating effect in this decay channel.

This illustrates how new physics could be detected from precise measurements of CP violation in various B-meson decays, combined with ρ and η determined from other B-meson decays. Detailed discussion can be found elsewhere [9].

B decays are also studied for checking the Superweak Model [10]. In this model it is assumed that the CKM matrix is real and that all CP-violating effects are from a contribution to the mixing that comes from beyond the Standard Model. In this case all the CP-eigenstate channels for B decay would have the same CP-violating asymmetry. This applies even to those channels predicted to have zero asymmetry in the Standard Model, as well as those for which the Standard Model prediction is complicated by the competition between tree and penguin contributions. Observation of significantly different asymmetries in any two neutral B decay CP-eigenstate channels would rule out such a model.

Charged Higgs contribution to mixing process are taken in to consideration as well. The appearance of such contributions in K mixing is already severely restricted by the K^0-$\overline{K}^0$ difference of mass. However this does not exclude additional contributions to B mixing that would destroy the relationship between the mixing phase ϕ_M and the CKM-matrix elements.

As already said, CP violation has been only observed in the neutral K system. Any observation of CP violation in B decays would be exciting. The Standard Model prediction is that direct CP-violating asymmetries are likely to be a few percent, so large effects in this channels would suggest effects beyond Standard Model.

There are many ways to look for a sign of new physics. In all cases, large numbers of both B_s^0 and B_d^0 mesons are required, and many different decay modes have to be reconstructed.

2.3 LHCb performance

Compared to other accelerators that are in operation or under construction, the LHC will be by far the most copious source of B mesons, due to the high $b\bar{b}$ cross section and high luminosity. A variety of b-hadrons, such as B_u, B_d, B_s, B_c and b-baryons,[1] are produced with high rate.

The LHCb experiment plans to operate with an average luminosity of 2×10^{32} cm^{-2} s^{-1}, which should be obtained from the beginning of LHC operation. Running at this luminosity has further advantages. The detector occupancy remains low, and radiation damage is reduced. Events are dominated by single pp interactions that are easy to analyse. The luminosity at the LHCb interaction point can be kept at its operational value while the luminosities at the other interaction points are being progressively increased to their design values. This will allow the experiment to collect data for many years under constant conditions. About 10^{12} $b\bar{b}$ pairs are expected to be produced in one year (10^7 seconds) of data taking.

The LHCb detector is designed to exploit the large number of b-hadrons produced at the LHC in order to make precision studies of CP asymmetries and of rare decays in the B-meson systems. It has a high-performance trigger which is robust and optimised to collect B mesons efficiently, based on particles with large transverse momentum and displaced decay vertices.

The detector can reconstruct a B-decay vertex with very good resolution. Excellent vertex resolution is essential for studying the rapidly oscillating B_s mesons. It also helps in reducing combinatorial background when reconstructing rare decays.

In addition LHCb should provide excellent particle identification for charged particles: without separating kaons from pions, reconstructed $B_d \to \pi^+\pi^-$ decays are heavily contaminated by $B_d \to K^\pm\pi^\mp$, $B_s \to K^\mp\pi^\pm$ and $B_s \to K^\pm K^\mp$ decays. These introduce large systematic errors in the measured CP asymmetry in $B_d \to \pi^+\pi^-$ decays, since these decay modes may well have asymmetries too. The measurement of their asymmetries is also interesting. The ability to distinguish kaons from pions is also essential for $B_s \to D_s^\pm K^\mp$, where the main background comes from $B_s \to D_s^\pm\pi^\mp$ decays. The branching fraction of $B_s \to D_s^\pm\pi^\mp$ is about ten times larger than $B_s \to D_s^\pm K^\mp$, and no CP violation is expected. Therefore, without separating the two channels, CP asymmetries in $B_s \to D_s^\pm K^\mp$ decays would be seriously diluted. Particle

---

[1]This notation refers to both particle and antiparticle states.

identification is also needed for the reconstruction of $B_d \to DK^*$ decays, to reduce combinatorial background.

With the capabilities described above, LHCb is ideally suited to determine all the angles of the two unitarity triangles using high statistics. Table 2.1 shows the expected numbers of offline-reconstructed events for various B-meson final states in one year of data taking. Simulation studies show that the LHCb detector is able to trigger and reconstruct, in addition to final states with only charged particles, also those including photon's or π^0's. This enhances the capability of the experiment to determine α without theoretical uncertainty due to penguin amplitude, and to allow the interesting radiative penguin decays to be studied.

Table 2.2 summarises the expected precision on the angles of the unitarity triangles and the sensitivity to B_s^0-$\overline{B}_s^0$ oscillations, obtained after one year of data taking. It also indicates the decay modes used and the important features of the LHCb detector discussed above.

In addition to investigating CP violation in B-meson decays, the physics programme of the LHCb experiment will include studies of rare B and τ decays, D-$\overline{D}$ oscillations and B_c-meson decays. For example, the ability to reconstruct a large number of $B_d^0 \to K^{*0}\gamma$ decays as given in Table 2.1 demonstrates that the LHCb experiment can study various other decay modes generated by the b $\to$ sγ process, such as $B_d^0 \to K^{**}\gamma$[2] and $B_s^0 \to \phi\gamma$. Triggering and reconstruction of $B_d^0 \to K^{*0}\mu^+\mu^-$ should also be possible. The large numbers of reconstructed events expected allow searches to be made for surprising effects in these rare decay modes. Events needed to study these processes will pass the standard Level-0 to Level-2 trigger cuts. Only the Level-3 algorithm will need to be tuned accordingly.

---

[2]K^{**} refers to orbitally-excited kaon states.

Decay Modes	Visible Br. fraction	Offline Reconstr.
$B_d^0 \to \pi^+\pi^-$ + tag	0.7×10^{-5}	6.9 k
$B_d^0 \to K^+\pi^-$	1.5×10^{-5}	33 k
$B_d^0 \to \rho^+\pi^-$ + tag	1.8×10^{-5}	551
$B_d^0 \to J/\psi K_S$ + tag	3.6×10^{-5}	56 k
$B_d^0 \to \overline{D}^0 K^{*0}$	3.3×10^{-7}	337
$B_d^0 \to K^{*0}\gamma$	3.2×10^{-5}	26 k
$B_s^0 \to D_s^-\pi^+$ + tag	1.2×10^{-4}	35 k
$B_s^0 \to D_s^-K^+$ + tag	8.1×10^{-6}	2.1 k
$B_s^0 \to J/\psi\phi$ + tag	5.4×10^{-5}	44 k

Table 2.1: Expected numbers of events reconstructed offline in one year of data taking with an average luminosity of 2×10^{32} cm^{-2} s^{-1}, for some channels.

Parameter	Decay Mode	σ [1 year]	Exploited features of LHCb
$\beta + \gamma$	B_d^0 and $\overline{B}_d^0 \to \pi^+\pi^-$; no penguin	0.03	K/π sep.
$(= \pi \Leftrightarrow \alpha)$	penguin/tree$= 0.20 \pm 0.02$	0.03–0.16	K/π sep.
β	B_d^0 and $\overline{B}_d^0 \to J/\psi K_S$	0.01	-
$\gamma \Leftrightarrow 2\delta\gamma$	B_s^0 and $\overline{B}_s^0 \to D_s^\pm K^\mp$	0.05–0.28	K/π sep. and σ_t
γ	$B_d^0 \to \overline{D}^0 K^{*0}, D^0 K^{*0}, D_1 K^{*0}$ and $\overline{B}_d^0 \to \overline{D}^0 \overline{K}^{*0}, D^0 \overline{K}^{*0}, D_1 \overline{K}^{*0}$	0.07–0.31	K/π sep.
$\delta\gamma$	B_s^0 and $\overline{B}_s^0 \to J/\psi\phi$	0.01	σ_t
x_s	B_s^0 and $\overline{B}_s^0 \to D_s^\pm \pi^\mp$	95% CL	σ_t

Table 2.2: Expected precision on the angles of the unitarity triangles obtained by the LHCb experiment in one year of data taking. Special features of the detector, i.e. particle identification and excellent decay time resolution (σ_t), are indicated when they are important.

Bibliography

[1] A. D. Sakharov, JETP Lett. **6** (1967) 21.

[2] J. Christenson et al., PRL **13** (1964) 138.

[3] M. Kobayashi and K. Maskawa, Prog. Theor. Phys. **49** (1973) 652.

[4] N. Cabibbo, Phys. Rev. Lett. **10** (1963) 531.

[5] L. Wolfenstein, PRL **51** (1983) 1945.

[6] C. Caso *et al*, The European Physical Journal **C3** (1998) 1

[7] P. Paganini *et al.*, DELPHI-97-137 and LAL-97-79.

[8] For a recent review, see A.J Buras, TUM-HEP-349/99 (1999).

[9] CLEO Collaboration. 34th Rencontres de Moriond : Electroweak Interactions and Unified Theories Les Arcs, France, 1999. CLNS-99-1623;
M. Gronau and D. London, Phys. Rev. **D55** (1997) 2845;
A.I. Sanda, Z.-Z. Xing , Phys. Rev. **D56** (1997) 6866;
Y. Grossman, Y. Nir, and R. Rattazzi, SLAC-PUB-7379 (1997);

[10] L. Wolfenstein, PRL **13** (1964) 562.

[11] See for example L. Wolfenstein and Y.L. Wu, Phys. Rev. Lett. **73** (1994) 2809.

[12] P. Cho, M. Misiak and D. Wyler, Phys. Rev. **D54** (1996) 3329.

Chapter 3

The richness of LHCb

3.1 Why should we be RICH?

To identify a particle means to determine charge and mass at rest. If generally the first task does not introduce problems, the second is not trivial.

At least two kinematic variables are necessary to determine the mass. The two variables to be measured are chosen depending on the energy of the phenomena and from the experimental problems that are introduced using a specific detection technique.

For energy in the range of some GeV, it is natural to measure the momentum of a particle from the radius of curvature in a magnetic field. This will be the first variable. As second variable one can choose between the velocity β and the energy.

Having an ultra-relativistic particle the precision dm/m, knowing p and β, is:

$$\frac{dm}{m} = \frac{1}{m}d\left(\frac{p}{\gamma\beta}\right) = \gamma^2\frac{d\beta}{\beta} + \frac{dp}{p} = \frac{1}{\beta^2}\frac{d\gamma}{\gamma} + \frac{dp}{p} \qquad (3.1)$$

Table 3.1 shows the precision on m needed to separate particles of mass m_1 and m_2.

Particles	$\mu \Leftrightarrow \pi$	$\pi \Leftrightarrow K$	$K \Leftrightarrow p$	$\Sigma \Leftrightarrow \Xi$
$\frac{m_2-m_1}{m_1}$	0.86	2.25	0.903	0.103

Table 3.1: Precision on m needed to separate the indicated pairs of particles.
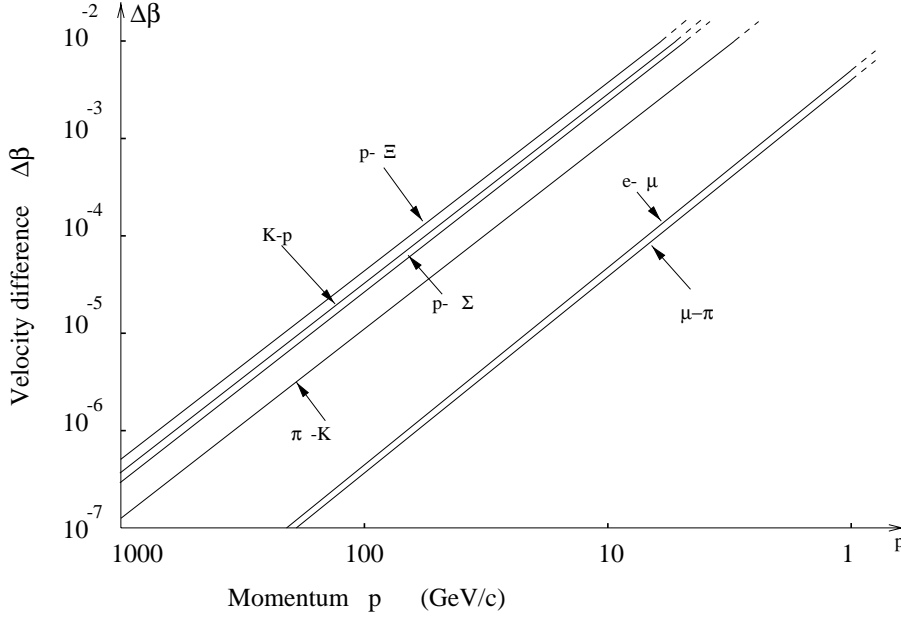
Figure 3.1: Difference on velocity needed in order to separate different pairs of particles having the same momentum.

The values in this table show, together with the relation 3.1, that the resolution on the momentum is not as crucial as the one on the mass. For the case $\pi \Leftrightarrow K$, $d(p)/p \approx 10\%$ is sufficient, while for the mass the resolution must be larger for higher momenta due to the factor γ^2.

Because

$$m_2^2 \Leftrightarrow m_1^2 = p^2 \frac{\Delta\beta(\beta_1 + \beta_2)}{(\beta_1\beta_2)^2} \qquad (3.2)$$

and, for approximation,

$$(\frac{\Delta\beta}{\beta})_{m_1,m_2} \approx \frac{m_2^2 \Leftrightarrow m_1^2}{2p^2}, \qquad (3.3)$$

one can show (Fig. 3.1) the resolution on the velocity necessary for the identification of particles having the same momentum.

There are different particle identification techniques. One can measure
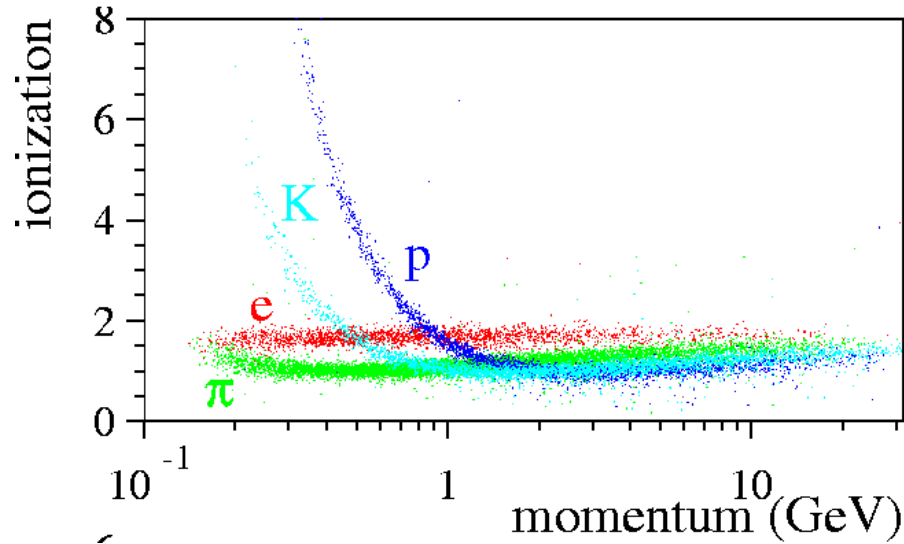
Figure 3.2: Variation of the specific ionization (MeV g^{-1} cm^2) vs. momentum.

the Time of Flight of a particle over a given distance L. We have:

$$\frac{\Delta\beta}{\beta} = \frac{\Delta\tau}{\tau} = \frac{\Delta\tau}{L}\beta c.$$

For a $\pi \Leftrightarrow K$ separation up to 3 GeV, a $\Delta\beta = 1.5 \cdot 10^{-2}\beta^2$ is needed. This separation can be reached only with a very good time precision of 50 ps over a distance of 1 m.

Another method is the measurement of the specific ionization dE/dx, which depends on the momentum and the mass. Because of the relativistic plateau, this technique can not be efficiently used above few GeV.

Last, but surely not least, we consider the Cherenkov radiation.

3.2 Cherenkov said

Until 1934 the Cherenkov light had been considered a manifestation of the well-known fluorescence phenomenon. But the newly graduated student P.A. Cherenkov, whom the teacher (P.V. Vavilov) had assign the task to study what happens when the radiation from a radium source penetrates

into and is absorbed in different fluids, was not convinced by that explanation.

His first experiments indicated that his intuition was correct. He found that the radiation was essentially independent of the composition of the liquid. This was in disagreement with the fluorescence explanation. By observing radiation even in doubly distilled water, he eliminated the possibility of minute impurities fluorescing in the liquids.

The mathematical explanation of this effect came in 1937 with the work of I.M Frank and I.Y. Tamm (and the Nobel prize for the three scientists followed in 1958).

When a particle goes through a dielectric medium it polarizes the surrounding atoms or molecules. When these go back to the initial state, they emit electromagnetic radiation. If the velocity of the particle is $\beta < 1/n$, with n the index of refraction of the medium, there is totally destructive interference. On the contrary, for $\beta > 1/n$ there is emission of photons. The photons are emitted at a fixed angle with respect to the particle propagation:

$$\cos\theta = \frac{1}{\beta n}, \tag{3.4}$$

with an intensity given by the Frank-Tamm relation:

$$\frac{d^2 N_{ph}}{dLd\lambda} = 2\pi\alpha Z^2 \frac{\sin^2\theta}{\lambda^2} \tag{3.5}$$

or:

$$\frac{d^2 N_{ph}}{dLdE} = \frac{\alpha}{\hbar c} Z^2 \sin^2\theta \tag{3.6}$$

where α is the fine structure constant and Z the charge of the particle in electronic units. There is a natural cut-off for the λ of the photons: $n = n(\lambda)$ and for X-rays we have $n < 1$, that implies no Cherenkov light emission. Combining Eq. 3.4 and 3.6:

$$\frac{d^2 N_{ph}}{dLdE} = \frac{\alpha}{\hbar c} Z^2 \left[1 \Leftrightarrow (1/n\beta)^2\right] \tag{3.7}$$

In Photomultipliers, as well as in HPD's, the photons are converted to photoelectron to be detected. It is possible to predict the final number of photoelectrons:

$$N_{p.e.} = \left(\frac{\alpha}{\hbar c}\right) L\, \epsilon_A \int Q\mathcal{R}\sin^2\theta_c\, dE_\gamma\; = N_0 \sin^2\theta_c, \tag{3.8}$$

where ϵ_A is the coverage of the photodetector active area, $\mathcal{R}, Q$ are the detector efficiency (Reflection,Quantum) averaged between the energy limits E_b and $E_t = E_b + \Delta E$. N_0 is normally referred to as the merit factor of the detector.

Being RICH

With the Cherenkov effect, one can measure the velocity by detecting the produced photons or by measuring in addition the angle at which these photons have been emitted. Of course the precision is much higher in the latter case. The precision on the Cherenkov angle for $N_{d.p.}$ detected photons is:

$$\sigma_\theta(N_{d.p.}) = \frac{1}{\sqrt{N_{d.p.} \Leftrightarrow N_{par}}} \cdot \sigma_\theta(1_{d.p.}). \tag{3.9}$$

N_{par} is the number of unknown parameters. Without a tracker $N_{par} = 3$: we need two angles for defining the particle direction plus the Cherenkov angle. With a tracker $N_{par} = 1$ because the Cherenkov angle is the only unknown quantity.

From Eq. 3.4 we find the error on the velocity for one single detected photon:

$$\frac{\sigma_\beta}{\beta} = \tan\theta \cdot \sigma_\theta(1_{d.p.}) \tag{3.10}$$

Therefore choosing different radiators it is theoretically possible to have particle identification from 1 GeV up to 150 GeV.

3.3   LHCb RICH

In high energy pp collisions the production of b hadrons is expected to be predominantly in the forward region ($\theta < 400$ mrad, cfr. Fig 1.1), with a strong correlation between particle emission angle and momentum. In section 2.3 it was stressed that LHCb should provide excellent charged particle identification.

The polar angle θ is plotted as a function of the momentum for all particles in fully simulated B events in Fig. 3.4. There is a clear correlation between particles at large angles having the softer momentum. The requirements for particle identification can be determined from the momentum spectra of the

Material		CF$_4$	C$_4$F$_{10}$	Aerogel
$\theta_{\mathrm{c}}^{\max}$	[mrad]	32	53	242
$p_{\mathrm{thresh}}(\pi)$	[GeV/c]	4.4	2.6	0.6
$p_{\mathrm{thresh}}(\mathrm{K})$	[GeV/c]	15.6	9.3	2.0
$\sigma_\theta^{\mathrm{emission}}$	[mrad]	0.21	0.54	0.36
$\sigma_\theta^{\mathrm{chromatic}}$	[mrad]	0.22	0.54	1.21
$\sigma_\theta^{\mathrm{pixel}}$	[mrad]	0.18	0.72	0.72
$\sigma_\theta^{\mathrm{total}}$	[mrad]	0.35	1.10	1.45
N_{pe}		30	55	15
$\sigma_\beta^{\mathrm{track}}$	$/10^{-6}$	1.9	7.9	92.4

Table 3.2: The three radiators that will be used in the RICH of LHCb: in the higher part some characteristics (maximum Cherenkov angle, threshold momentum for π and K), in the lower the contributions to the resolution (from emission-point, chromatic and pixel errors), the total resolution per photoelectron, the mean number of detected photoelectrons in the ring image, and the error on β per particle.

particles in representative low- and high-multiplicity decays, like $\mathrm{B}_{\mathrm{d}}^0 \to \pi^+\pi^-$ and $\mathrm{B}_{\mathrm{s}}^0 \to \mathrm{D}_{\mathrm{s}}^-\pi^+\pi^+\pi^-$ [1]. The low-multiplicity decays define the upper momentum limit required for $\pi \Leftrightarrow K$ separation. In about 90% of $\mathrm{B}_{\mathrm{d}}^0 \to \pi^+\pi^-$ neither particle has momentum greater than $150\,\mathrm{GeV}/c$ in the very forward region ($10 < \theta < 120$ mrad) or greater then $65\,\mathrm{GeV}$ over the rest of the acceptance. The high-multiplicity decays define the lower momentum limit. In about 90% of the $\mathrm{B}_{\mathrm{s}}^0 \to \mathrm{D}_{\mathrm{s}}^-\pi^+\pi^+\pi^-$ decays none of the particles have momentum less than $1\,\mathrm{GeV}/c$ over the whole acceptance. Thus one has to separate pions from kaons unambiguously over the momentum range $1 < p < 65\,GeV/c$, and up to $150\,\mathrm{GeV}/c$ in the very forward region.

These requirements are met by a RICH detector with three different radiators: two gases (CF$_4$ and C$_4$F$_{10}$), and one with silica aerogel. In Tab. 3.3 some properties of these materials are listed.

3.3.1   The RICH 1

RICH 1 is the detector dedicated to the identification of low-momentum particles. It is therefore designed to cover polar angles corresponding to the full acceptance of the LHCb spectrometer, i.e. 330 mrad in both the horizontal and vertical projections. For low momentum particles, particle identifica-
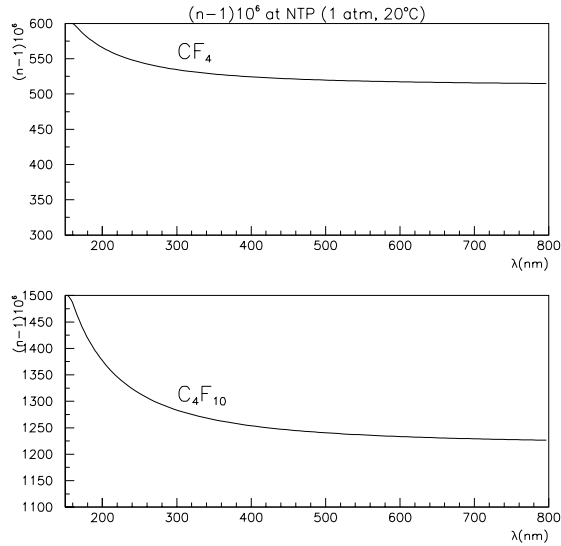
Figure 3.3: Refractive index of CF_4 and C_4F_{10}.

tion must occur upstream of the dipole magnet, before they are swept out of the acceptance (see Fig. 1.4 for a global view of LHCb and Fig. 3.5 for a schematic view of the subdetector itself).

RICH 1 combines both aerogel and C_4F_{10} radiators, with the gaseous radiator covering the inner acceptance as close as possible to the beam pipe. The inner acceptance of the aerogel is limited to 50 mrad, to reject the scattered light produced by high momentum particles with small angle. A schematic view of RICH 1 is shown in Fig. 3.5. A particle entering the detector from the interaction region first traverses a 5 cm thickness of silica aerogel, and then approximately 95 cm of C_4F_{10} gas. This is the fluorocarbon with highest refractive index (Fig. 3.3) that remains gaseous at normal temperature and pressure, and is chosen for its low chromatic dispersion. The Cherenkov light produced in the radiators is focussed by two spherical mirrors, with 190 cm radius of curvature, one on each side of the beam pipe. They are tilted by 250 mrad to bring the image planes out of the acceptance of the spectrometer, to a rectangular array of photodetectors 60 cm×100 cm on each side.
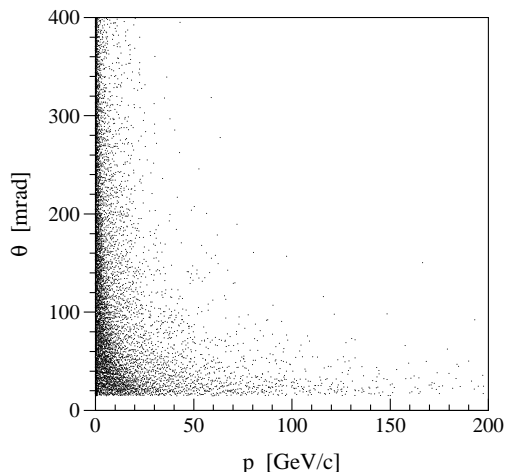
Figure 3.4: Polar angle versus momentum for all particles in fully simulated B decays events.

C_4F_{10} radiator

When reconstructing the emission angle of a detected photon from a given particle, the emission point is not known: the mid-point along the path in the radiator weighted by the trasparency is taken. As photons are emitted all along the path in the radiator, the calculated Cherenkov emission angle is smeared, as shown in Fig. 3.6 (a).

Another source of imperfect resolution is the dispersion in the refractive index of the radiator. For C_4F_{10} gas the index varies from 1.0013 at long wavelength, to 1.0015 at about 200 nm ($E_\gamma \sim 6$ eV). The wavelength spectrum of the detected photons is determined by the quantum efficiency of the photondetector. The quantum efficiency dependence on photon energy used for the LHCb Technical proposal is shown in Fig. 3.7. The entrance window of the photodetector cuts off the energy spectrum; in LHCb it is chosen to be UV glass giving $E_\gamma < 5.5$ eV. The effect of this chromatic error is shown in Fig. 3.6 (b).

Finally, there is the effect of the granularity of the photodetector. This
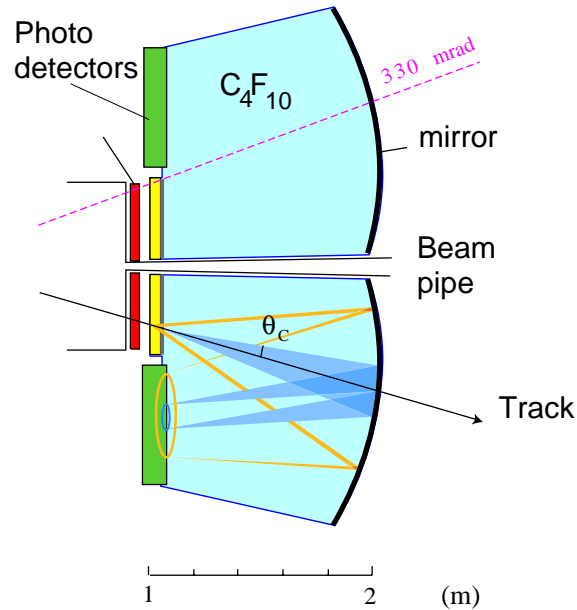
Figure 3.5: Schematic layout of the RICH 1 detector. Horizontal projection.

is chosen to be $2.5{\times}2.5\,\text{mm}^2$ taking in account the needed resolution whilst limiting the total number of channels. The final contribution is shown in Fig. 3.6 (c). Taking all three effects together, the RMS resolution per photo-electron for C_4F_{10} is 1.1 mrad, for particles with velocity $\beta \approx 1$.

The expected number of detected photoelectrons is given by Eq. 3.8, where the radiation length is $L = 95$ cm. The assumed coverage of the photodetector active area is $\epsilon_A = 0.73$ and the assumed mirror reflectivity is $\mathcal{R} = 0.95$. Using the quantum efficiency Q from Fig. 3.7, Eq. (3.8) gives approximately 55 photoelectrons/track for a saturated C_4F_{10} ring. Thus the resolution per track is about 0.15 mrad.

Aerogel radiator

An accurate description of the aerogel properties will be given in Chapt. 4, where a beam test of aerogel samples is described. Silica aerogel is a colloidal form of quartz. It is solid but with extremely low density and it has a long-established use in threshold Cherenkov counters. Its refractive index can be chosen in the range 1.01–1.10, ideal for the identification of particles with
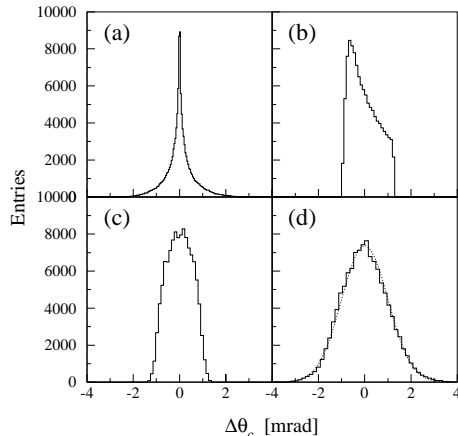
Figure 3.6: Contributions to the resolution of the C_4F_{10} radiator: (a) emission-point uncertainty; (b) chromatic error; (c) pixel size; (d) overall resolution per detected photoelectron, with superimposed a Gaussian fit.

momentum of a few GeV/c. Aerogel radiator, with a threshold $\gamma_t \approx 17$, permits positive π/K identification only above 8 GeV.

The idea of using aerogel in a ring-imaging detector [2, 3] has followed from the development of high quality, very clear, samples. Optical properties of aerogel will be described in Sec. 4.1. For a particle passing through 5 cm of aerogel with $n = 1.03$ the resulting number of detected photoelectrons in a saturated ring image is expected to be approximately 15 plus 5 scattered over the detection plane.

The contributions to the resolution have been determined for the aerogel radiator in a similar way as those for C_4F_{10}, and are listed in Table 3.3. The overall resolution per photoelectron for aerogel is 1.4 mrad, very near to the C_4F_{10} resolution, permitting the use of common photodetectors. The radiation hardness of aerogel has been studied by a group from KEK [6]. No significant degradation of the properties were observed up to 10 Mrad equivalent dose, well beyond that expected for the aerogel in LHCb. Tests have shown that the properties will not degrade significantly over the timescale of the LHCb experiment if appropriate precautions are taken during preparation, handling and storage [7]. The volume of aerogel required is anyway
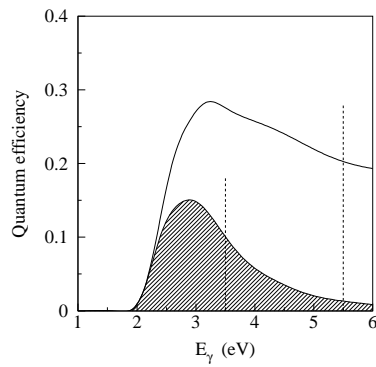
Figure 3.7: Quantum efficiency as a function of incident photon energy as-
sumed for the photodetectors used in the LHCb Technical Proposal [4] sim-
ulation (unshaded), given by Hamamatsu for bialkali photocathode. The
shaded distribution is the convolution with the probability of the photon re-
maining unscattered by the aerogel. The dashed lines indicate the assumed
window cut-offs.

modest, $\sim 30\,\ell$, so its replacement, if required, would be straightforward.

3.3.2   The RICH 2

The detector for the identification of high momentum particles, the RICH 2, is located downstream of the magnet. Since the beam pipe has a smaller opening angle (10 mrad) in this region, the detector can have a better inner acceptance. The low angle particles are also better separated far from the interaction point, and the correspondingly longer focal length of the focusing mirror allows a higher-resolution device to be constructed, as required to maximize the momentum coverage. An outer acceptance of 120 mrad in the horizontal plane and 100 mrad in the vertical plane has been chosen. The larger horizontal acceptance allows for the spreading of particles by the dipole magnet. This accepts 90% of pions from $B_d^0 \rightarrow \pi^+\pi^-$ decays with $p > 70\,\mathrm{GeV}/c$ which are beyond the limit for π–K separation in RICH 1.

A schematic view of RICH 2 is given in Fig. 3.8. A precise status of the art from a mechanical point of view will be given in Chapt. 6.

The radiator is approximately 180 cm thickness of CF_4 gas. This is chosen for its suitable refractive index (Fig. 3.3) at normal temperature and pressure, and low dispersion. The spherical focussing mirrors have a radius of curvature of 820 cm, and are tilted by 370 mrad to bring the image out of the acceptance of the spectrometer. An additional flat mirror is required on each side. The mirror positions and tilt angles have been optimised to give the best resolution for the detector, whilst keeping the flat mirror outside the RICH 2 acceptance to maximise the number of detected photoelectrons. The photodetectors are in a rectangular array of 72 cm×120 cm on each side, and the same granularity is assumed as for RICH 1.

The contributions to the resolution are listed in Table 3.3. Chromatic error is smaller, compared to RICH 1. Nevertheless RICH 2 does not need a reduced detector granularity because the focal length of the mirror is almost four times the one of RICH 1: the angle resolution is given by the ratio of the detector granularity over the mirror focal length. Then, for the same detector granularity, the pixel size error contribution in RICH 2 is 0.18 mrad and is comparable to the chromatic error of 0.22 mrad.
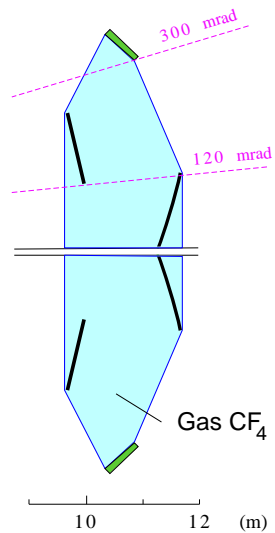
Figure 3.8: Schematic layout of the RICH 2 detector (seen from above).

3.3.3 Photodetectors

From what has been discussed in the two previous sections it is possible to summarize the requirements for the photodetectors of the RICH system as following:

- Single photoelectron sensitivity, with reasonable quantum efficiency in the visible and in the ultraviolet region.
- Pixel size must be $2.5 \times 2.5\,\mathrm{mm}^2$ in both systems
- Large area coverage ($1.2\,\mathrm{m}^2$ for RICH 1, $1.7\,\mathrm{m}^2$ for RICH 2)
- A total active area of $\approx 73\%$. This corresponds to 90% in radius for a cylindrical device (i.e. 81% in area) with a further factor of 0.9 from hexagonal close-packing the tubes.
- The photodetectors must be fast enough for the time between bunch-crossings of $25\,\mathrm{ns}$.

Other needs are the possibility to work in a low magnetic stray field, to be resisting to a radiation dose of few krad/year and to be able to survive for at least ten years in this environment.

Two detector technologies are candidates for meeting these requirements:

the hybrid photodiode (HPD) and the multianode photomultiplier (MAPMT). About the HPD's two approaches have been pursued: the "Pixel HPD", where a silicon pixel detector is bump-bonded to a binary readout electronics chip, and the "Pad HPD", where a silicon pad detector is read out using routing lines on the silicon surface, wire-bonded to separate electronics chips. Chap. 5 and 7 will be devoted to this item.

Bibliography

[1] R. Forty, "Ring-Imaging Cherenkov Detectors for LHCb", LHCb/96-5.

[2] D.E. Fields *et al.*, Nucl. Instr. Meth. **A 349** (1994) 431.

[3] LHCb Letter of Intent, "A dedicated LHC collider beauty experiment for precision measurements of CP violation", CERN/LHCC 95–5.

[4] LHCb Technical Proposal.

[5] I. Adachi *et al.*, Nucl. Instr. Meth. **A 355** (1995) 390;

[6] S.K. Sahu *et al.*, Nucl. Instr. Meth. **A 382** (1996) 441.

[7] A. K. Gougas *et al.*, Nucl. Instr. Meth. **A 421** (1999) 249.

Chapter 4

Cherenkov Rings from aerogel

The word "aerogel" was coined in 1932 by S. Klister. The following quotation, taken from Klister's first article on aerogel [1], explain clearly what an aerogel is:

"Obviously, if one wishes to produce an aerogel, he must replace the liquid with air by some means in which the surface of the liquid is never permitted to recede within the gel. If a liquid is held under pressure always greater than the vapor pressure, and the temperature is raised, it will be transformed at the critical temperature into a gas without two phases having been present at any time."

The first aerogels studied by Kistler were silica aerogels prepared by the acidic condensation of aqueous sodium silicate. Silica aerogel (aerogel from here) is used in threshold Cherenkov detector since the 1970s. Aerogel was used in the momentum range where neither NTP gases nor liquid radiators were suitable.

Before 1996 some studies [2, 3, 4, 5, 6] have been made for use aerogel in focused Cherenkov counters. In each case no real electronic method was implemented to detect the Cherenkov ring produced by a single particle.

The recent development in the 1990s of a new aerogel production technique, the so called "two-step" method [7], has improved its optical qualities with respect to the samples produced with the standard "single-step" method. Samples from the single-step method are hydrophilic, mechanically stiffer and more brittle while those from the two-step methods are hydrophobic with smaller pore size and thus less Rayleigh scattering at short wavelength. In the research and development framework for the BELLE experiment, the KEK group announced in 1994 the development of a third

39

method for production of aerogel [8]. The KEK aerogel is also hydrophobic but more transparent than aerogels produced with the previous method.

In this chapter a beam test with aerogel performed at CERN in 1996 is described. The task of the test was to prove that KEK aerogel is sufficiently transparent to produce Cherenkov rings with large signal and small background. Investigation were made to determine the number of photons inside, on, and outside the aerogel ring. The main results are described in [9]. In this thesis only the analysis mainly carried out by the author are explained in details.

Section 4.1 is devoted to the optical properties of aerogels and section 4.2 describes the apparatus used for investigating its imaging properties. Section 4.3.1 describes the photomultiplier spectra. In section 4.3.2 information from a simulation program are given. Section 4.3.3 reconstructs the Cherenkov angle by combining beam particle track and ring information to obtain optimal angle resolution (which means in our case refractive index of the radiator), and finally section 4.3.4 estimates the number of produced photoelectrons, the number of scattered and unscattered photons, and deduces from these measurements the quality of the aerogel sample.

4.1 Optical properties of aerogels

The optical properties of aerogels are best described by the phrase "aerogels are transparent". This may seem obvious, as aerogels are made of the same material as glass. However, the situation is not as simple as that comparison. While distant objects can be viewed through several centimeters of aerogel, the material displays a slight bluish haze when an illuminated piece is viewed against a dark background. These effects can be immediately attributed to Rayleigh scattering.

Rayleigh's law states that when a cone of light of wave-length λ, intensity I, and solid angle $d\omega$ is incident on a particle of polarizability β, energy at the rate

$$\frac{128\pi^5}{3\lambda^4}\beta^2 I d\omega \times \frac{3}{4}(1+\cos^2\alpha)\frac{d\omega'}{4\pi} \qquad (4.1)$$

is scattered in a direction making an angle α with the direction of incidence and in a solid angle $d\omega'$.

A macroscopic volume containing a large number of particles scattering the light has to be considered in the aerogel case. In Ref.[10] the final distribution is computed making the assumption that the scattering centers are perfectly randomly distributed. The polar angular distribution of the scattered photons is proportional to $\cos^2 \alpha$. The azimuthal angular distribution is flat.

A simple method can be used to quantitatively measure the relative contributions of Rayleigh scattering and the wavelength-independent transmission factor due to surface damage and imperfections.

The probability for a photon inside aerogel for not being scattered after having covered a path of length l is

$$T' = e^{S(\lambda) \cdot l} \tag{4.2}$$

where from Eq. 4.1 $S(\lambda) = \frac{C}{\lambda^4}$. An additional wavelength-independent factor A has to be introduced due to to surface damage and imperfections, therefore the last equation becomes:

$$T = Ae^{-\frac{Cl}{\lambda^4}} \tag{4.3}$$

where T is called the transmittance, A the wavelength independent asymptotic transmission factor and C the clarity coefficient.

An ideal aerogel would have $C = 0$ and $A \approx 1$. A could never be exactly 1 because of the reflectivity air-aerogel interface.

In aerogels, the primary particles have a diameter of 2-5 nm, and do not contribute significantly to the observed scattering. However, scattering does not necessarily arise from solid structures. There is in aerogels, a network of pores which can act, themselves, as scattering centers. The majority of these are much smaller ($\approx$20 nm) than the wavelength of visible light. There are, however, invariably a certain number of larger pores that scatter photons up to visible light. Control of the number and size of these larger pores is, to a certain degree, possible by modifying the sol-gel chemistry used to prepare the aerogel. As the Cherenkov light is peaked at short wavelength, it turns out that the crucial property required for a RICH detector is that the radiator should have scattering centers as small as possible.

The probability for Cherenkov photons, uniformly generated in a slab of thickness L , to traverse undeflected the radiator is

$$P = \frac{A}{\eta}(1 \Leftrightarrow e^{-\eta}) \tag{4.4}$$
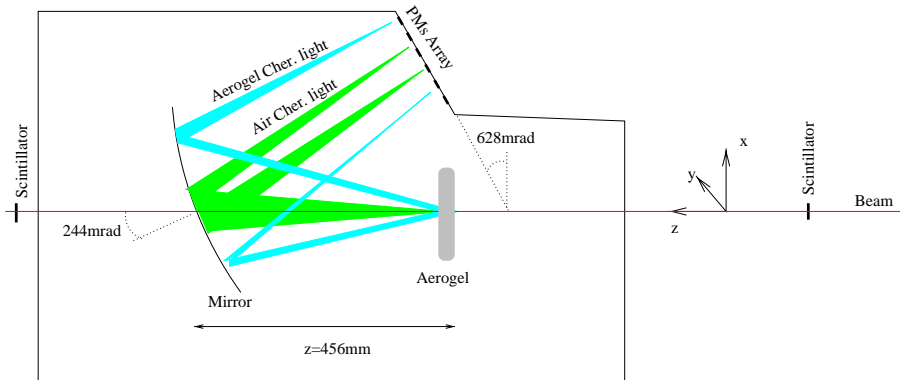
Figure 4.1: Schematic view of the RICH detector installed at the East Hall of the CERN-PS in the T9 beam with 10 GeV/c negative pions. Not to scale.

with $\eta = CL/\lambda^4$. This equation comes from the integration of Eq.4.3. If the photons are emitted at angle θ, L must be replaced with $L/\cos\theta$.

4.2　Description of the apparatus

The beam test was made in the hall T9 of the CERN-PS accelerator with a π^- beam of 10 GeV/c momentum, i.e. with $\beta = 1$. It was performed during August and September 1996.

The experimental setup, shown schematically in Fig.4.1, consists of a light-tight aluminum box (painted black and filled with NTP N_2), an aerogel radiator and a spherical mirror inclined 244 mrad to the beam direction. The mirror focused Cherenkov light from radiator on the detector plane. Because the mirror is tilted, this image is not a perfect circle but an ellipse-like, as will be showed later. To reduce unwanted interactions, both entrance and and exit walls are made of 100 μm thick Tedlar foils. The mirror reflectivity has been measured just after the production (12 Jan 1995), and is shown in Fig. 4.16. The focal length is $f = 450$ mm.

The setup is such that the center of curvature of the mirror is placed between the aerogel and the detector plane to place the latter as close as possible to the focal surface.

To detect the Cherenkov photons a matrix of 114 (see Fig. 4.2) hexagonally close packed Hamamatsu R268 Photomultipliers (PM) is used. Five

PM's were dead and two inefficient. The PM's have a 25 mm diameter photocathode on a 28 mm diameter borosilicate glass window. The quantum efficiency, provided by Hamamatsu, is shown in Fig. 4.16. The average energy of detected photons (for a uniform spectrum in energy) is $< E >=$3.1 eV.

A time coincidence between two groups of beam hodoscope, placed 3 m upstream and 1 m downstream from the entrance face of the light-tight box, provided an event trigger with negligible accidental rate. Each hodoscope consisted of two crossed, 4 mm thick, plastic scintillators. The overlap region (20×20 mm^2) of the two groups defined the particle direction with angular error $\sigma_\theta = 2$ mrad.

This test aimed to measure the aerogel Cherenkov angle from the detected ring, the number of aerogel photoelectron and the background coming from scattered photons. The information from the N$_2$ ring can be used for calibration. Various thickness of aerogel were measured in order to optimize the radiator, but the analysis described in this work has been done only on one sample of 2.5 cm thick aerogel.

An image of PM hits in one event is displayed in Fig. 4.3. It shows clearly the aerogel ring on the peripheral PM's and the unresolved N$_2$ ring. Fig 4.4 shows the integrated map in a ring of 32000 events.

4.3 Analysis of the data

4.3.1 Photomultiplier spectra

For each event, a beam track trigger generated a 50 ns wide read-out gate and the pulse hight of each PM within the gate was digitized.

The pulse-hight distribution of three PM's located in three different regions (outside the signal region, on the aerogel ring and on the N$_2$ ring) are shown in Fig. 4.5. From the χ^2/dof of a simple Gaussian fit it is possible to see the contribution from multiple photoelectron. In the first region only scattered photons are expected to contribute. In the aerogel ring and in the N$_2$ ring regions the photoelectron distributions show a contribution from multiple photoelectrons signal.

For determining the Cherenkov angle from aerogel a threshold was set for each PM at four standard deviation from the pedestal distribution, and binary information has been used (hit-PM / not hit-PM) event per event. The binary information is suitable for the estimation of the Cherenkov angle.
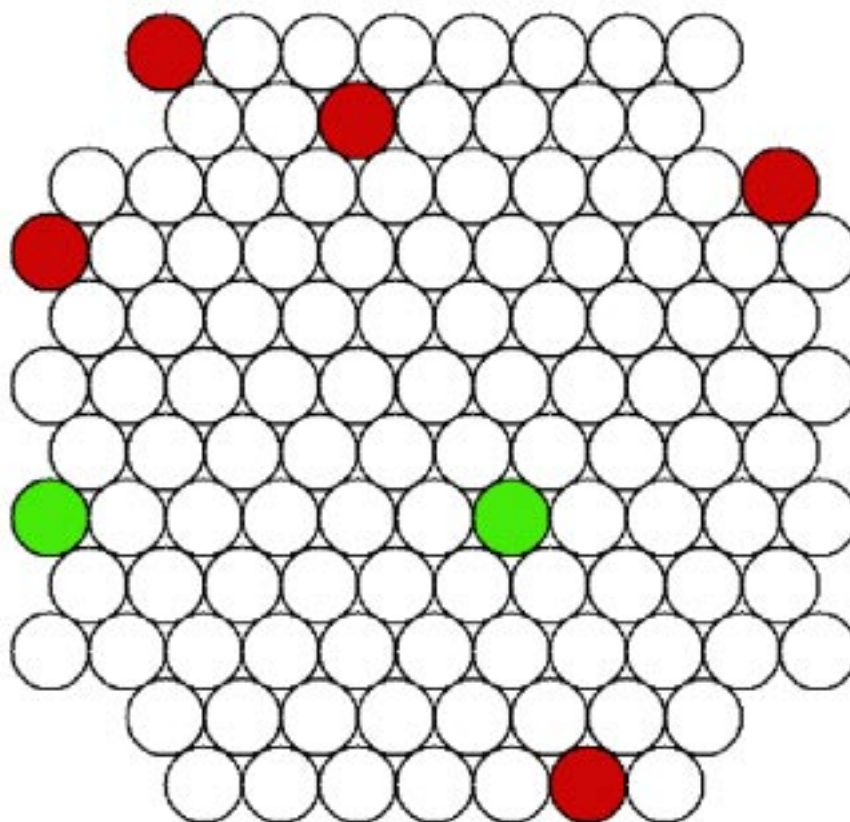
Figure 4.2: PM's array used for the beam test. Dead (red/black) and ineffi-
cient (green/gray) PM's are indicated.
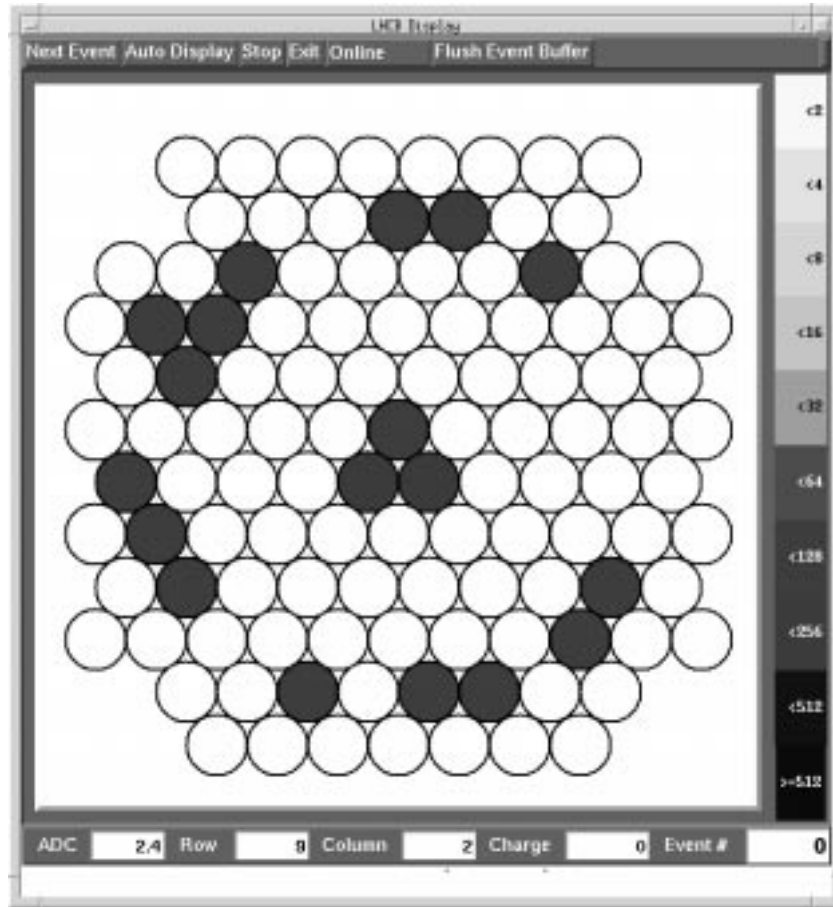
Figure 4.3: A single-event display on the PM's array. The central spot is the unresolved N_2 ring and the outer ring is from aerogel.
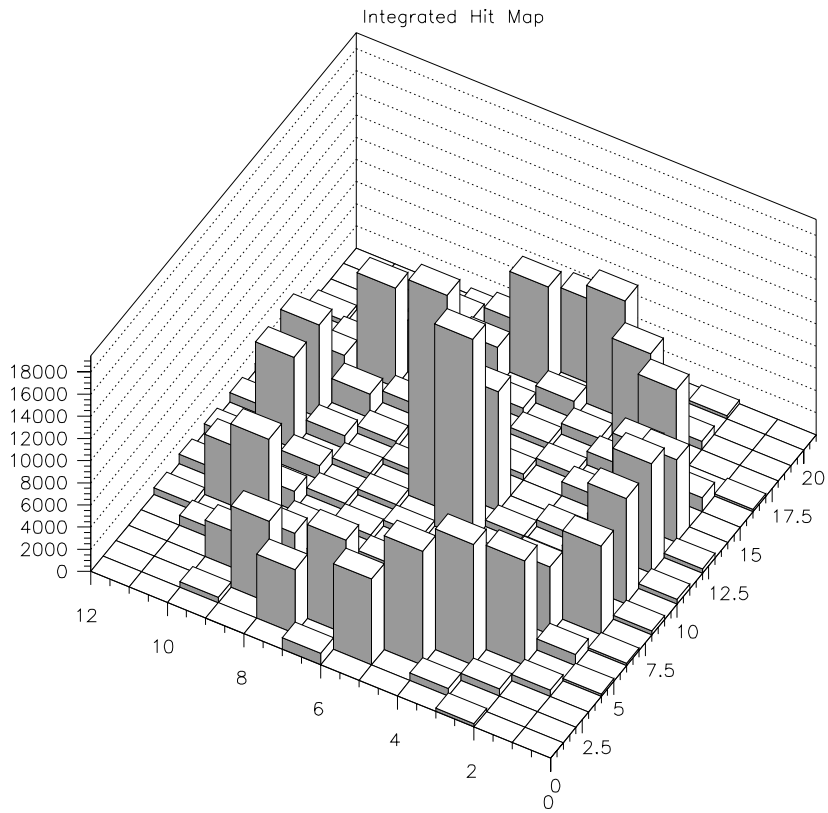
Figure 4.4: Integrated hit map in the PM's in a 32000 event run. The central spot is the unresolved N_2 ring and the peripheral ring is from aerogel.
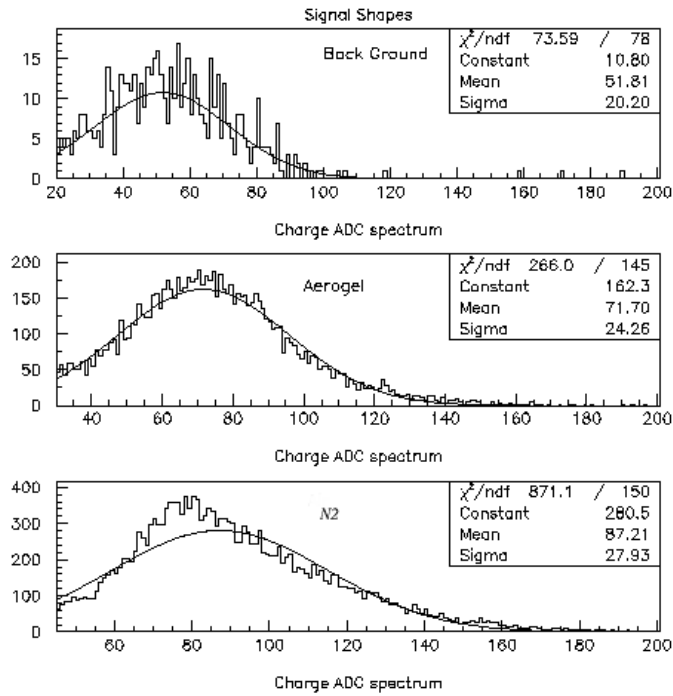
Figure 4.5: Signal shapes for PM's located outside the signal region, on the aerogel ring, on the N_2 ring. From the χ^2/dof is possible to see how well the spectra fit to a Gaussian distribution. Multiple photoelectron spectra are the sum of multiple Gaussians. This means that in the last two spectra multiple photoelectron corrections are necessary .

For the estimation of the number of photoelectrons, a more accurate analysis of the spectra is necessary.

The spectra from the PM's in the three different regions have been analyzed (Figures 4.6, 4.7, 4.8). The spectra are fitted with the following equation:

$$f(x) = N \sum_{n=0}^{\infty} \frac{e^{-\mu}\mu^n}{n!} \frac{e^{-\frac{(x-a-d(n=0)-n/b)^2}{2(\sigma_{ped}^2 + n\sigma_{din}^2)}}}{\sqrt{2\pi}(\sigma_{ped}^2 + n\sigma_{din}^2)}, \qquad (4.5)$$

which involves 7 free parameters (N, μ, a, b, σ_{ped}, σ_{dinode}, d). It is a Poisson-Gaussian convolution: the area of the n-th Gaussian is proportional to the corresponding Poisson probability, its sigma is the sum, in quadrature, of the pedestal sigma (σ_{ped}) and the fluctuation of the first dinode gain ($\sqrt{n}\sigma_{dinode}$). a is the pedestal shift, b the number of photoelectrons per channels. The 7th parameter d has been introduced because of a not perfect linearity of the photoelectron signal. That means probably that the production of secondary electrons on the first dinode is not linear.

The 2-photoelectrons contribution is not negligible neither for air nor for aerogel spectra:

- for the air spectra 18% of the pulses above threshold are generated by 2 photoelectrons and 6% by 3 photoelectrons;

- for the aerogel spectra μ varies, for different PM's, from 0.32 to 0.38. That means that the 2-photoelectrons contribution varies from 3.7 to 4.9%.

4.3.2   Simulation of the apparatus

The focal surface for a non tilted mirror is a plane. The first geometry [12] chosen for the RICH's of LHCb had no-tilted mirrors and spherical shaped aerogel up against the focusing mirror. This configuration had the disadvantage that all Cherenkov photons had to traverse the full thickness of the aerogel before reaching the detector. This lead to a significant reduction of the number of photons due to scattering. A geometry similar to the test beam set up was therefore chosen.

With a tilted mirror the image is brought out of the acceptance, where the photodetectors are placed. The drawback is that the image is no more a circle, but an ellipse-like.

For the analysis of the data, a program was written to simulate creation and refraction of the photons inside the aerogel, reflection on the mirror
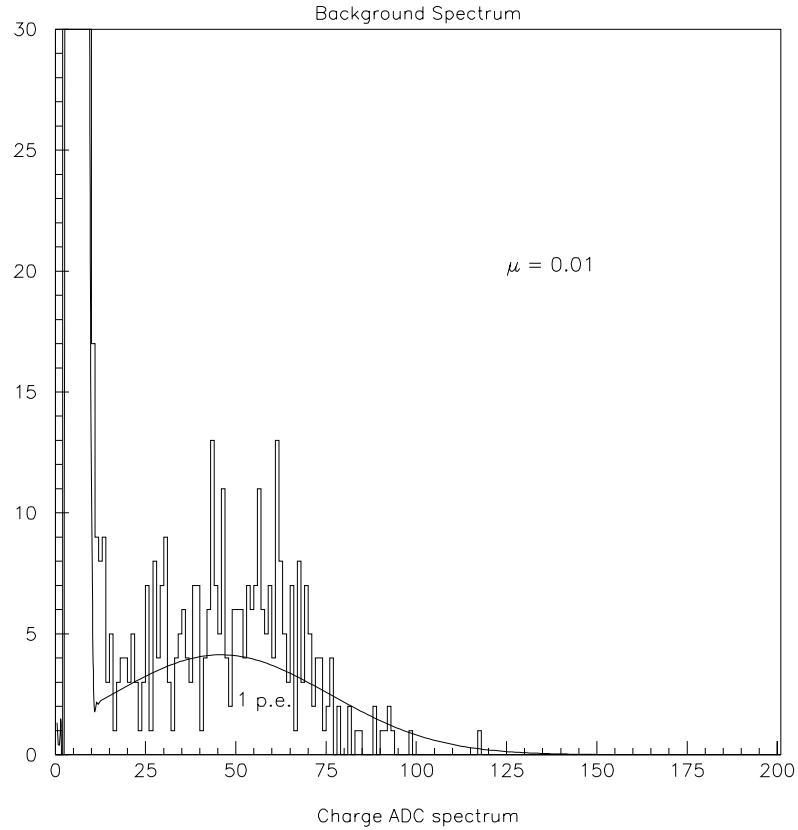
Figure 4.6: Background spectrum fitted with Eq.4.5 (N=34270, $\mu = 0.01$, a = 6.2, b = 0.06, $\sigma_{ped} = 0.98$, $\sigma_{dinode} = 30.0$, d = 22). The average number of photoelectrons is 0.009. As expected, the 2-photoelectrons contribution (computed from Poisson distribution) is almost zero.
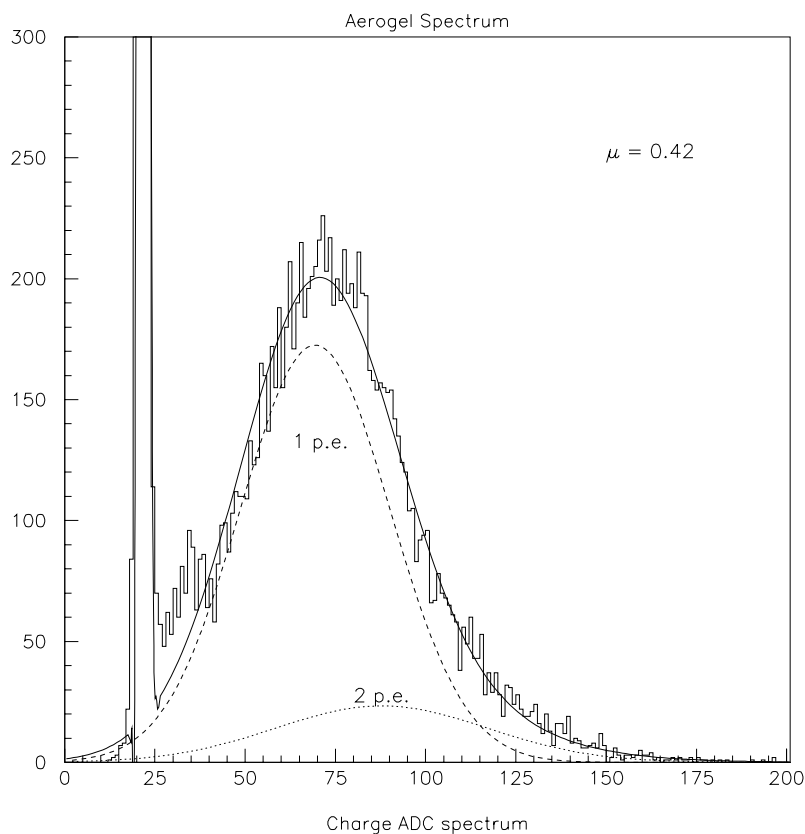
Figure 4.7: Aerogel spectrum fitted with Eq.4.5 (N=34345, μ = 0.42, a = 22, b =0.06, σ_{ped} = 0.79, σ_{dinode} = 21.5, d = 29). The average number of photoelectrons is 0.42. The 2-photoelectrons contribution (computed from Poisson distribution) is 5.8%. For other PM's on the aerogel ring, μ varies between 0.4 and 0.5
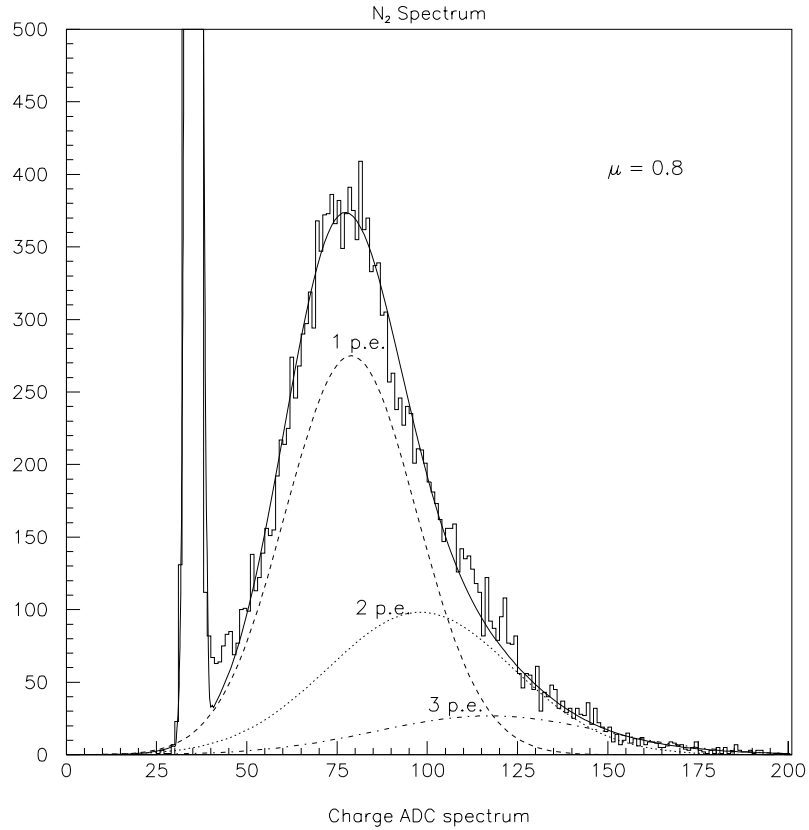
Figure 4.8: N$_2$ spectrum fitted with Eq.4.5 (N=34115, μ=0.79, a= 35.3, b = 0.047, σ_{ped} = 1.3, σ_{dinode} 15, d=19). The average number of photoelectrons is 0.8. The 2-photoelectrons contribution (computed from Poisson distribution) is 14%

and detection. The program was based on an existing one [11]. The index
of refraction of the aerogel as a function of the photon energy used in the
simulation, is shown in Fig. 4.9.

In Fig. 4.10 are shown the hits on the mirror surface of the simulated
Cherenkov photons produced in the aerogel by 1000 pions with same mo-
mentum. These photons are reflected in a perfectly geometrical way on to
the detector plane. The hits on the detector plane are shown in Fig. 4.11. It
is clearly visible that the image is not a circle but an ellipse-like 2×122 mm
wide along x direction and 2×112 mm wide along y direction

4.3.3   Cherenkov angle estimation

The reconstruction of the Cherenkov angle can be obtained with two different
methods. For both of them the aerogel ring radius is found fitting the aerogel
PM's hits in each event using the Linear Regression Method (See App. A).
At this point one can estimate the Cherenkov angle dividing the measured
mean radius by the mirror radius of curvature. This gives only an estimation
because the image is not a perfect circle. In order to have the real Cherenkov
angle one has to reconstruct from the fitted circle the original shape of the
image.

The result of the first step of the analysis is shown in Fig. 4.12 for a
3 cm thick aerogel sample. The distribution of the radii of the fitted circles
is plotted. Therefore a first estimation of the Cherenkov angle can be ob-
tained dividing this number by the mirror radius of curvature. This gives a
Cherenkov angle:

$$\theta_C = (117 \pm 8.5) \text{ mm}/450 \text{ mm} = 260 \pm 20 \text{ mrad}$$

which leads to an aerogel refraction index $n_{aerogel} = 1.035 \pm .005$, compatible
with the one given by the KEK production group ($n = 1.03$).

For the second method we use the information coming from the residuals
(the distance between the hit and the fitted circle, see Eq. A.3), called ρ.
The values of the residuals vary with the different azimuthal angle ϕ. In
Fig. 4.13 it is possible to see an average behavior of ρ: it is mainly positive
for $\phi = 0°, 180°$ and negative for $\phi = 90°, 270°$ as the image is not a circle.
To parameterize this behavior the mean value of ρ has been computed for
$n \times 45° < \rho < (n+1) \times 45°$ with $n = 0,...,7$. These eight points have then
been fitted with a simple sinusoid curve. The result is $\rho = 5.07 \cos(2\phi)$ mm.
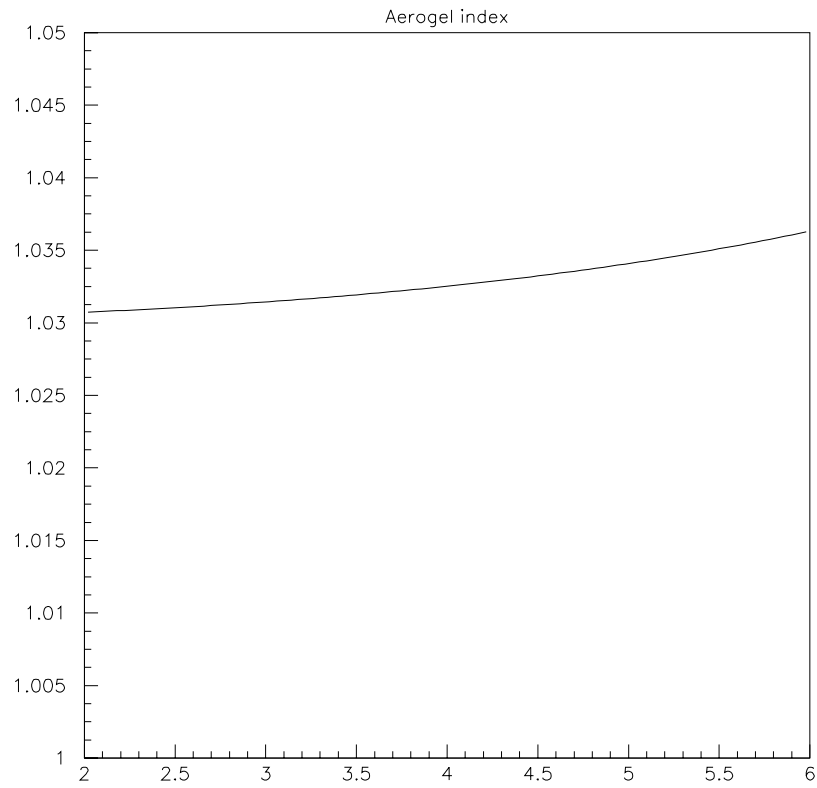
Figure 4.9: Index of refraction of the aerogel used in the simulation versus photon energy.

Mirror hits
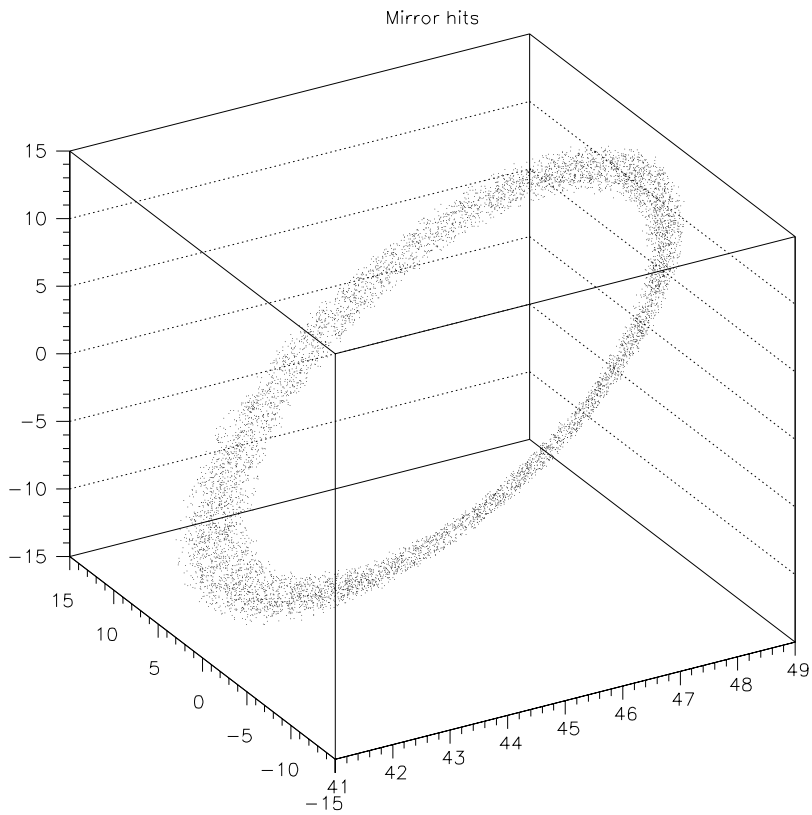
Figure 4.10: Hits of the simulated Cherenkov photons produced in the aerogel on the mirror surface.
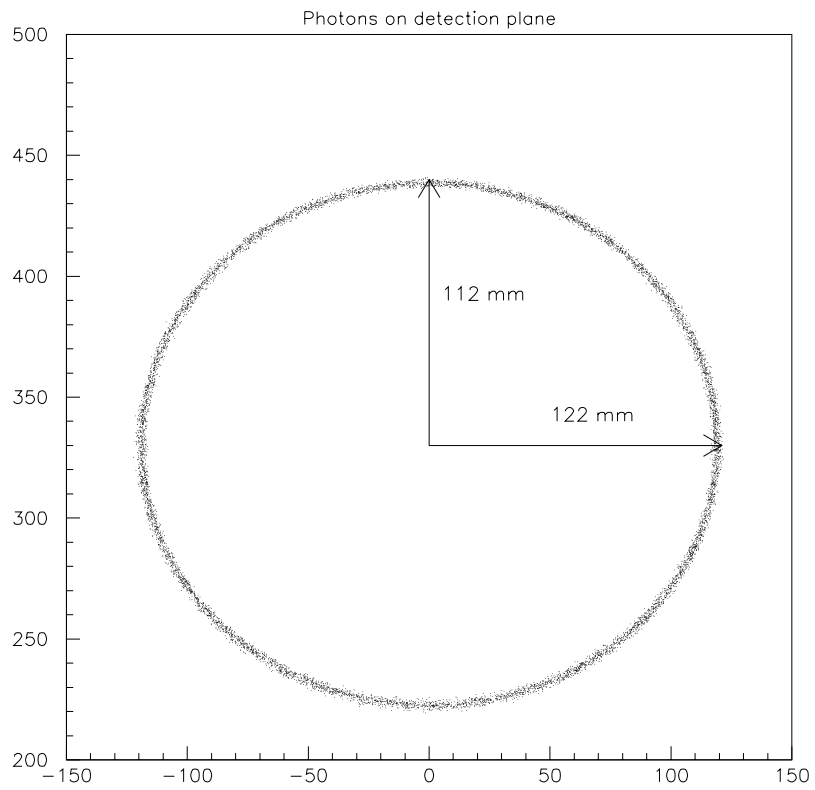
Figure 4.11: Hit of the simulated Cherenkov photons produced in the aerogel on the detector plane. The reference system in this case has x and y on the detector plane.
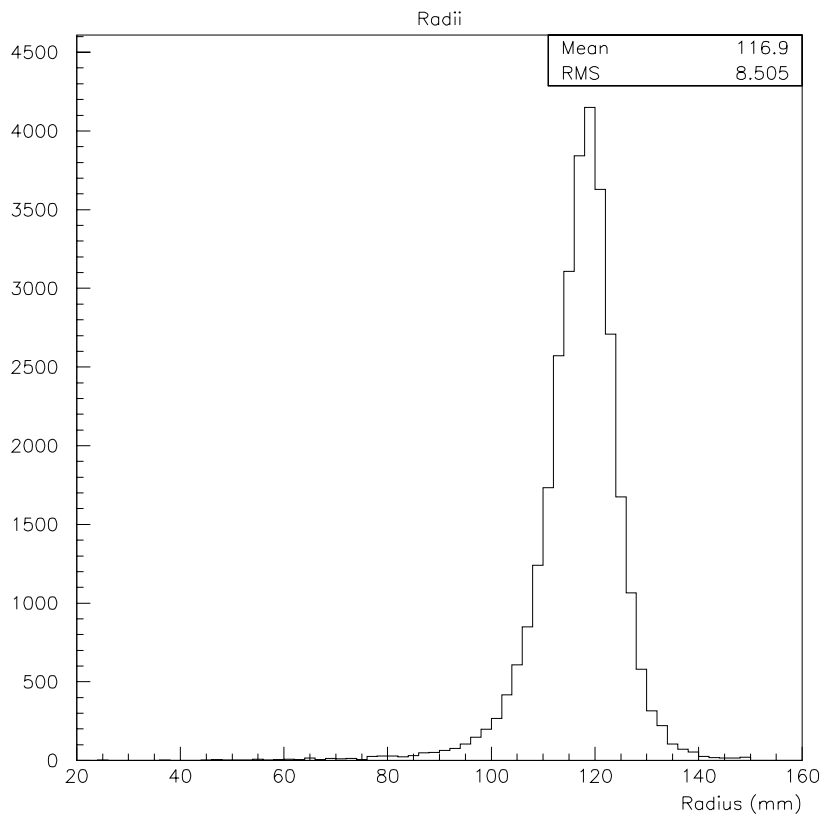
Figure 4.12: Radius fitted event per event with the Linear Regression Method (App.A) .

That means that the reconstructed ellipse-like is (107+5) mm wide along x ($\phi = 0°, 180°$) and (107-5) mm along y ($\phi = 90°, 270°$).

Once the shape of the Cherenkov image is known, we can tune the refractive index of the aerogel used in the simulation in order to have the same image from the simulation. The refractive index shown in Fig. 4.9 is the one which gives the image of Fig. 4.11. This image corresponds exactly to the one obtained from the circle fit.

4.3.4   Number of photoelectrons

The main task of the test beam was to estimate the number of photoelectrons produced and the fraction of these produced by scattered photons.

The expected number of photoelectrons produced by unscattered photons can be computed from Eq. 3.8 and Eq. 4.4:

$$N_{p.e.} = KL(\text{cm})\, \epsilon_a A \int Q(E)\mathcal{R}(\mathcal{E})\eta(E)(1 \Leftrightarrow e^{-\eta(E)}) \sin^2 \theta(E)\, dE \qquad (4.6)$$

where K is 370 cm^{-1}eV^{-1}, L is the radiator length in cm, ϵ_a the geometrical acceptance, A the asymptotic transmission, $Q(E)$ the photocathode quantum efficiency, $R(E)$ the mirror reflectivity, $\eta = \lambda^4 \cos\theta/(C(\lambda^4)L) = hc/C(E)L$, C the clarity coefficient, θ the Cherenkov angle (the photons emitted at length l have to cover a distance $(L \Leftrightarrow l)/\cos\theta$) and E the photon energy in eV.

The values used are plotted in Fig.4.16. The Rayleigh transmission probability is computed starting from a clarity coefficient value tuned in order to have a good agreement between the estimated number of scattered photons and the measured ones, as discussed below.

In this analysis first the background coming from external sources has been estimated. Figure 4.14 shows the accumulated counts for an empty target run. The peak in the middle is the N$_2$ ring which, since its radius is 8.5 mm, is seen by one or two PM's. Two kinds of background are present. The first extends up to 150 mrad and is due to mirror imperfection, it is $\approx 1\%$ of the signal. The second is flat and due to electronic noise, and it is about 0.05% of the signal.

Secondly the center of the image plane of every event has been determined, using the center of the fitted circle. Then the distance of the hits from the center has been divided by the radius of curvature of the mirror to get the approximated angle of emission θ. In the plot of Fig. 4.15 every bin
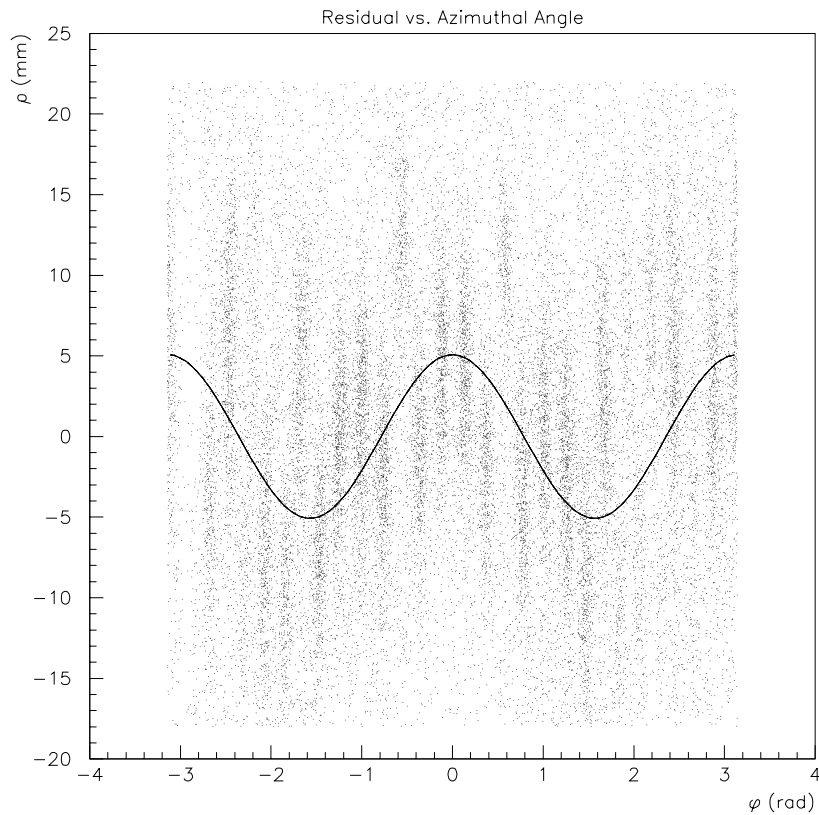
Figure 4.13: Distance of the hit PM's from the circle fitted event by event versus the polar angle ϕ ($\phi = 0$ per $y = 0$). An average has been done every $45°$ for the fit shown in the figure. The result is $\rho = 5.07\cos(2\phi)$.

was weighted by $1/\theta$. This takes into account the increase in phase space as θ increases. The distribution obtained is fitted with two Gaussians, one for the N_2 ring and one for the aerogel, and a background proportional to $\cos^2(\alpha)$ according to what explained in Sec. 4.1.

Then the number of PM hits in the region outside the N_2 ring was determined. The result is in Fig. 4.17. The mean number of photoelectrons is $<N_{pe}> = 9.0$.

This number has to be corrected for dead PM's, 2-photoelectrons contribution and background:

- 24 PM's are essentially covering the aerogel ring. Of those, only one is dead. Thus $N_{pe}^{corr} = N_{pe}^{obs} \times 24/23$;

- The fits of the spectra (Sec. 4.3.1) showed that the mean 2-photoelectrons contribution is 6%. Thus the signals obtained in the aerogel region have to be multiplied by 1.06;

- The fit to the plot of Fig. 4.15 shows that 20% of the detected photons are coming from scattered photons (the aerogel Gaussian is sitting on an almost flat background). Thus $N_{pe}^{corr} = N_{pe}^{obs} \times 0.8$;

Applying all the corrections the final result is;

$$N_{pe}^{corr} = 8.0$$

This result has to be compared to the one expected one from Eq. 4.6 for different clarity coefficient C, where the tuned refractive index of Fig. 4.9 is used. The value of A is set to 0.96 from laboratory measurement.

The final value of C is

$$C = 0.0106 \ \mu\text{m}^4\text{cm}^{-1}$$

Compatible with $C = 0.01$, obtained in [9] on the same data sample with a simulation of the Rayleigh scattering.

4.3.5   Conclusion

For the first time, focused Cherenkov rings produced by charged particles traversing aerogel have been observed in a test beam with electronic detection.

The Cherenkov angle resolution is limited by the PM size.

In this chapter a method for reconstructing Cherenkov angle without knowing the charged particle direction has been described and used. With this method an estimation of the refractive index, as a function of the energy of the emitted photon, can be done. This estimation has been used to determine the probability of Rayleigh scattering in the aerogel samples studied in the test.

The improvement in the transmittance of the commercially available aerogel, makes its use as a RICH radiator possible because it increases the fraction of undeflected photons which leave the radiator.
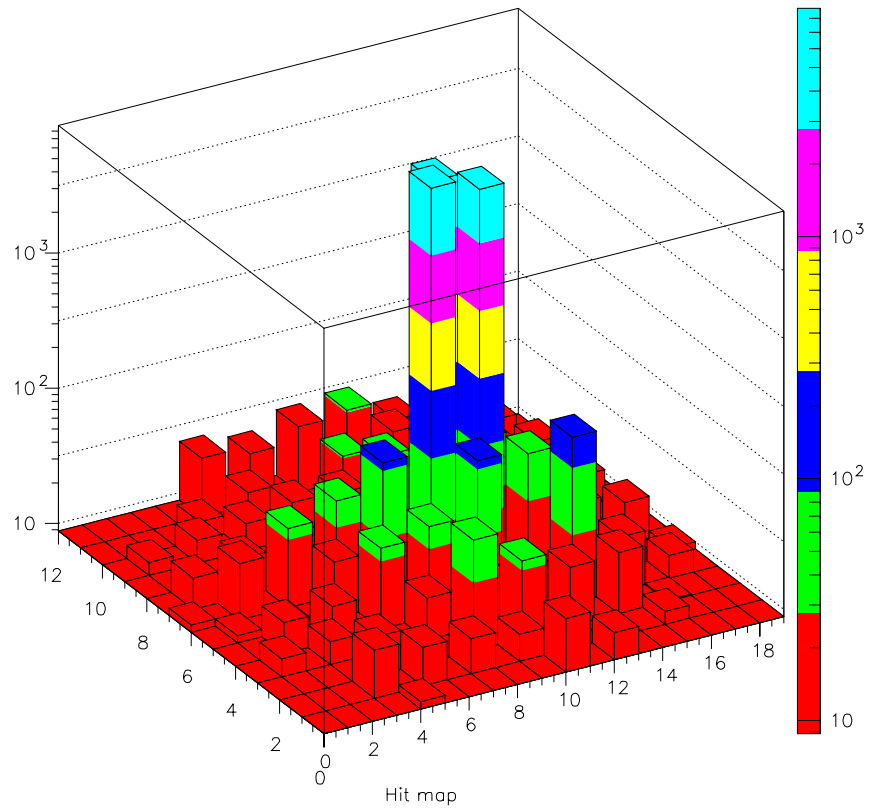
Figure 4.14: Integrated hit map of PM's array in a 10000 events run without aerogel. The central spot is the unresolved N_2 ring. The background near the ring is caused by diffuse (non-specular) reflection of the mirror ($\approx 1\%$), the flat one (0.05%) comes from electronic noise.
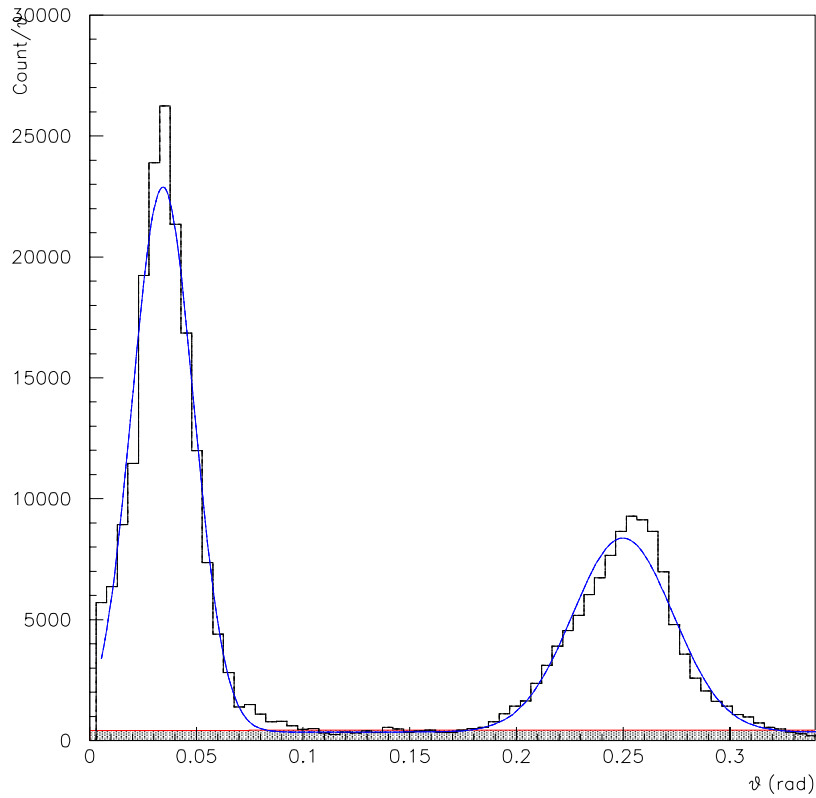
Figure 4.15: Distance of the hit points from the center of the fitted circle divided by the mirror radius of curvature ($\approx$angle of emission). Every bin was weighted by $1/\theta$ to account for the increase in phase space as θ increases. The almost flat background has bin fitted (gray filled area), for Rayleigh scattering, with a $\cos^2 \alpha$. The N_2 and aerogel photon distribution with two Gaussian. It is evident a tail due to mirror diffusion for the N_2 photon distribution and an asymmetry for the aerogel photon distribution due to the limited geometrical acceptance.
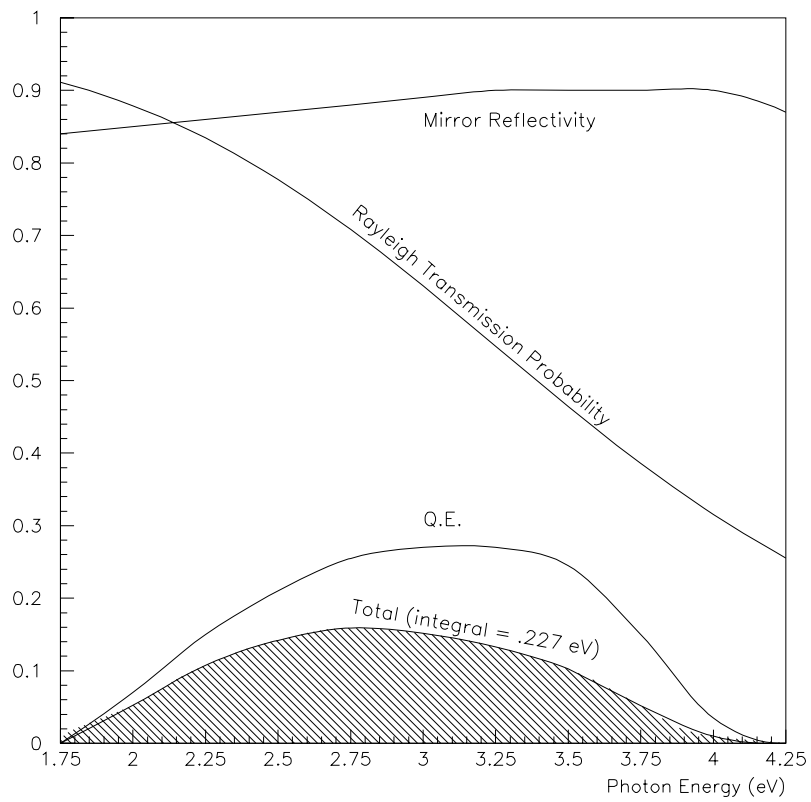
Figure 4.16: Probability (shaded region) for an emitted photon of energy E to be detected unscattered. Mirror diffusion is not taken in account.
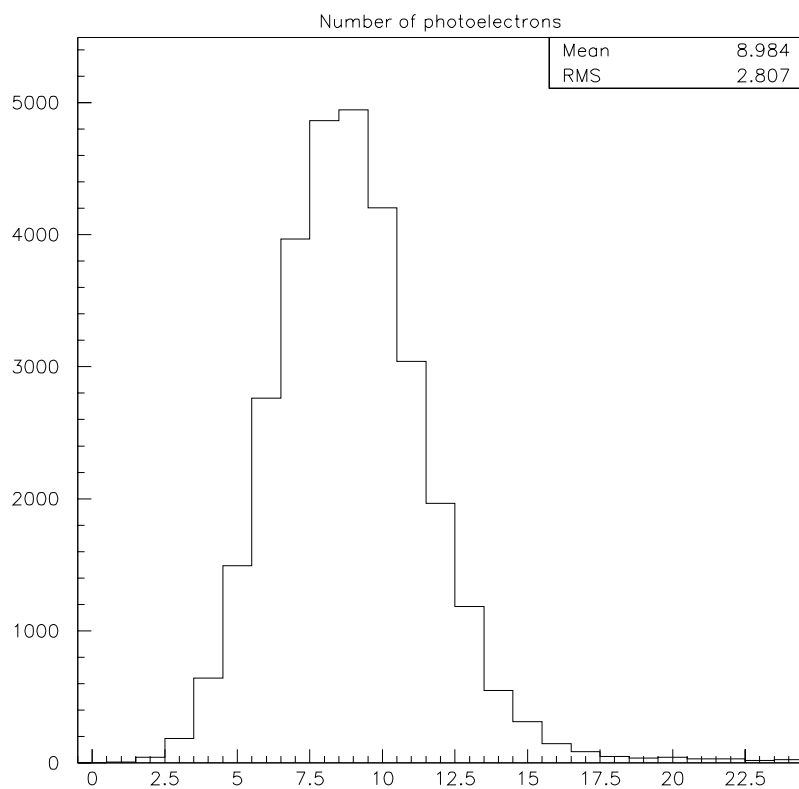
Figure 4.17: Number of photoelectrons in the range $\theta_C \pm 100$ mrad for a 2.5 cm thick sample. The mean value is 9.1. No correction for dead PM, background, or 2-photoelectrons contribution is applied.

Bibliography

[1] S.S. Klister, J. Phys. Chem. **A 34** (1932) 52.

[2] M.. Cantin *et al.*, J. Chem. Phys. **A 71** (1974) 1537.

[3] M. Ben *et al.*, Nucl. Instr. Meth. **A 154** (1978) 253.

[4] V.I. Vorobionof *et al.*, Proc. of the Workshop on Physics and detectors for DAPHNE, Report INFN-Frascati, 1991.

[5] H. van Hecke *et al.*, Nucl. Instr. Meth. **A 343** (1994) 311.

[6] D.E. Fields *et al.*, Nucl. Instr. Meth. **A 248** (1986) 118.

[7] UCRL-Ext. Abs 102518 preprint, LLL 1990.

[8] I. Adachi *et al.*, Nucl. Instr. Meth. **A 355** (1995) 390;

[9] R. De Leo *et al.*, Nucl. Instr. Meth. **A 401** (1997) 187.

[10] S. Chandrasekhar, Radiative Transfer, Oxford at the Clarendon Press 1950.

[11] R. Forty, Nucl. Instr. Meth. **A 384** (1996) 167; the term $4a(b^2 + c^2)R$ in Eq. 1 should read $4a^2(b^2 + c^2)R$.

[12] The LHCb Letter of Intent

Chapter 5

Focusing HPD's

LHCb has, as said in Chap. 3, HPD's as two over three options for photodetectors for the RICH technique: Pixel HPD and Pad HPD. In this Chapter, after a brief introduction about HPD's, the work done for the Pad option will be described.

5.1 Hybrid Photo Diode's - HPD's

HPD's are conceptually simple[1], very schematically they have two components:

- a photocathode, exactly like in the traditional phototubes

- a silicon detector (a depleted diode) as photoelectron detector

In Fig. 5.1 is possible to see a very schematic design of an HPD. As for the photomultiplier tubes the photocathode of an HPD converts energy of incident light into photoelectrons.

The diode is left at potential 0. A high, negative voltage is applied to photocathode, typically bigger than 10 kV, 20 kV in both Pad and Pixel HPD. The photoelectrons are thus accelerated on to the diode. Here they loose all the kinetic energy in thermic processes and in the creation of pairs electron-hole.

The number of electron-hole pairs, which is practially identical to the gain of the detector, is given by

$$N = HV(V)/W(eV)$$

HV being the potential of the photocathode and W being the energy required to create an electron-hole pair in silicon (3.6 eV). The actually observed number of electron-hole pairs will be a bit smaller, since some energy, typically of the order of 2 keV, will be lost in the 0.5 μmthick ohmic contact (usually called "dead layers") of the silicon sensor. In a well designed sensor, about 5000 electron-hole pairs can be detected for a voltage difference of 20 kV.

Since the gain is achieved in a single dissipative process, the fluctuations of N, i.e. $\sigma(N)$, is determined by Poisson statistics:

$$\sigma(N) = \sqrt{N} \iff \sigma(N)/N = 1/\sqrt{N}$$

That means that the intrinsic resolution of an HPD's is very high: the statistical error of the first (and last) gain stage is $\approx .014$

The drawbacks are:

- a very low signal to be detected, which makes require a pre-amplifier chain;

- to achieve the desired ratio of active to total area it is necessary to have a number of pixel per detector of $\mathcal{O}(1000)$. In this case a feed-through for each pixel out of the vacuum envelope becomes impractical and it is necessary to include miniaturized preamplifiers within the vacuum envelope;

- the necessity to deal with high-voltage, even if low-power.

The development of HPD's constitutes a major advantage for the RICH technique for different reasons:

- the possibility to have a high granularity, corresponding to a high spatial resolution;

- the sensitivity to visible light, compared to gas detector, results in better performances (cfr. "Aerogel resolution" in Sec.3.3.1);

- the excellent energy resolution on the photoelectrons, compared to photomultiplier tubes, allows a single photon counting.
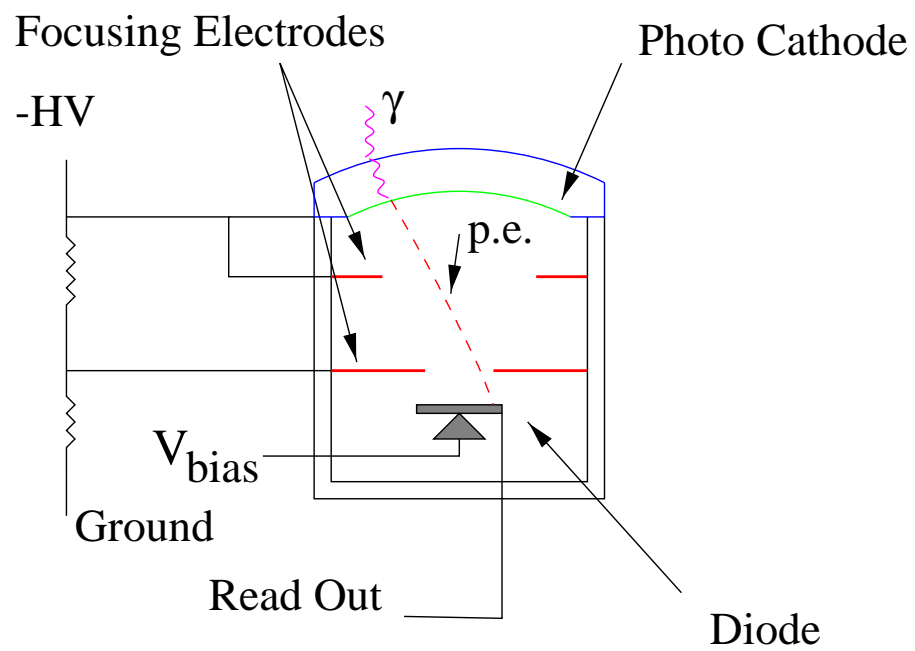
Figure 5.1: Schematic view of an HPD.

5.2   Focusing properties of the Pad HPD's

As said in Chap. 3 For the RICH of LHCb a granularity of 2.5×2.5 mm^2 is required. . That means that the photoelectrons have to be focused on the silicon detector by a well defined electrical field configuration which makes possible a photocathode mapping. Devices with the requested granularity already exist with a few pixels. External read-out electronics is possible thanks to a feed-through for each pixel out of the vacuum envelope. These devices do not fulfill the RICH request because a much to low active area.

The two options of HPD's obtain this result in two different ways. In the Pad HPD's photoelectrons emitted from the photocathode are accelerated towards the silicon sensor by an inverse fountain shaped electric field. The field configuration is such that a demagnified image of the photocathode is produced on the silicon sensor.

In Chap. 3 it is also explained that, to detect a sufficient number of phothons for the reconstruction of the Cherenkov rings, the ratio active/total surface has been chosen to be 73%. Cylindrical detectors, as the Pad HPD, if an exagonally close-packed cover 91% of the surface. That means that the active area of a single Pad HPD must be 81% of the total area. Pad HPD's have an overall diameter of 5" $= 127$ mm. The active area requested is 90% in radius, that means that all the photoelectrons emitted by the photocathode at $r < 57$ mm must be focalized on the silicon sensor. The silicon sensor has a diameter of 50 mm where 2048 pads of 1×1 mm^2 are present. To have a complete mapping of the photocathode the demagnification factor has to be then 2.3.

With an electron optical device all the electrons emitted at the same point and at the same energy hit the focal surface at the same point, then there is the possibility to map every point of the cathode with every point of the anode.

In inverse fountain focused HPD's photoelectrons emitted by the photocathode from the same point but at different angles hit the anode surface at different points (see. Fig5.9). The width of the distribution of the photoelectrons hit points on the anode is the point spread function.

The point spread function of the photoelectrons on the silicon detector can be easily computed for the Pad HPD configuration making some approximation.

Let us consider an HPD where the photoelectrons are accelerated on to the silicon detector by an uniform electric field $E = \frac{V}{l}$ (V is the High

Voltage and l the distance photocathode-silicon detector). The time for the photoelectrons hitting the silicon is

$$t = \sqrt{\frac{2l^2 m}{eV}}$$

with e the electron charge. The component of the initial velocity parallel to the electrical field does not affect the trajectory of the electron, then we consider a photoelectron with azimuthal angle of emission of $90°$ and initial energy $E_0 = eV_0$. The initial velocity is

$$v_0 = \sqrt{\frac{2eV_0}{m}},$$

and the final displacement on the silicon comes to be

$$d_{psf} = v_0 \cdot t = 2l\sqrt{\frac{V_0}{V}}. \tag{5.1}$$

For the Pad HPD's $l = 100$ mm and $V = 20\,000$ volt. Let us consider an initial energy of 1 eV and an azimuthal angle of emission of $45°$. This is the same as saying initial energy of 0.5 eV and angle of emission of $90°$. If the field were uniform would be $\sigma_{psf} = \pm 1$ mm.

We should finally consider that in the Pad HPD the accelerating field is not uniform. Applying a demagnification factor of 2.4 the final displacement becomes $\sigma_{ppd} = \pm 0.42$ mm.

The final uncertainty on the photoelectron position on the diode is

$$\sigma_{anode} = \sqrt{\sigma_{pxlsize}^2 + \sigma_{psf}^2} = 0.52 \text{ mm}$$

with $\sigma_{pxlsize}$ is the size of the silicon pixel over $\sqrt{12}$, i.e. $\sigma_{pxlsize} = 0.29$ mm.

Then in the final design of the Pad HPD's, the uncertainty on the position of the emission point of the photoelectronshould be equal to:

$$\sigma_{emission} = .52 \times 2.3 \text{ mm} = 1.2 \text{ mm}.$$

5.3 Simulation of the Pad HPD's

The properties of the first design proposed[2] by Tom Ypsilantis (Fig 5.2) were investigated with computer aided engineering systems by the japanese
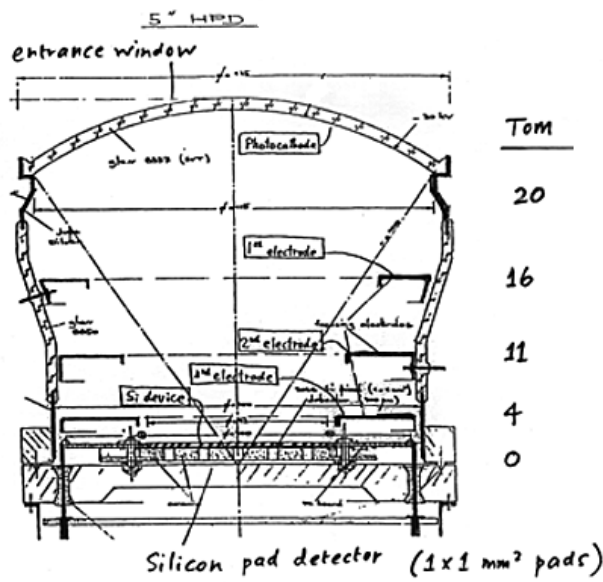
Figure 5.2: First design proposed for the Pad HPD's.

company Hamamatsu and by Thierry Gys (who used the software package POISSON). They showed some problems like cross-focused photoelectrons and an excessive factor of demagnification.

A third cross check was carried out by the author with MAFIA[3]. MAFIA is a commercial software package for solving Maxwell's equations. It discretizes the Maxwell equations on orthogonal grids. This yields a set of matrix equations, each of which is the discrete analogue to one of the original Maxwell equations. These matrix equations are then solved numerically.

The HPD's are cylindrical, then a reference system in cylindrical coordinates (r, z, θ) is used. Thanks to the symmetry on θ the Maxwell equations are solved on a bidimentional grid on r, z. The result of the simulation of the first proposed design is shown in Fig. 5.3 with z along the abscissa and r along the ordinates. From left to right is possible to see the photocathode, the metallic skirt which joins the photocathode to the glass envelope, and the three focusing electrodes.

In order to minimize the number of points only the internal surface of the photocathode window has been correctly shaped. In fact the external surface of the window is not important for the focusing electrical field, and is not rightly shaped in order to minimize the number of point of the grid used by MAFIA.

Photoelectrons are emitted by the photocathode with an initial energy of about 1 eV. At this energy they are very sensitive to changes of the electrical field. Then along the photocathode surface the field must remain as uniform as possible.

In Fig. 5.3.b the field in the region where the photocathode joins the skirt is zoomed. The transition between the two surfaces is quite abrupt, so that the electrical field deviates the photoelectrons emitted in this region to much on the inner part of the tube. The simulations carried out to study this undesired effect are now described.

MAFIA is able to compute the trajectory of a limited number (nine) of particles. The trajectories of photoelectrons outcoming from the photocathode in the range $42 < r < 55.2$ mm are shown in Fig 5.4 . The maximum r of emission corresponds to a photoelectron produced by a photon which hits the photocathode window at $r = 57$ mm with a direction parallel to the axis of the HPD (the lens effect of the 4 mm thick window has to be considered). The photoelectrons are emitted perpendicularly to the photocathode. It is possible to see in the figure that the most external photoelectrons are actually crossfocused and for all of them the demagnification factor is more than
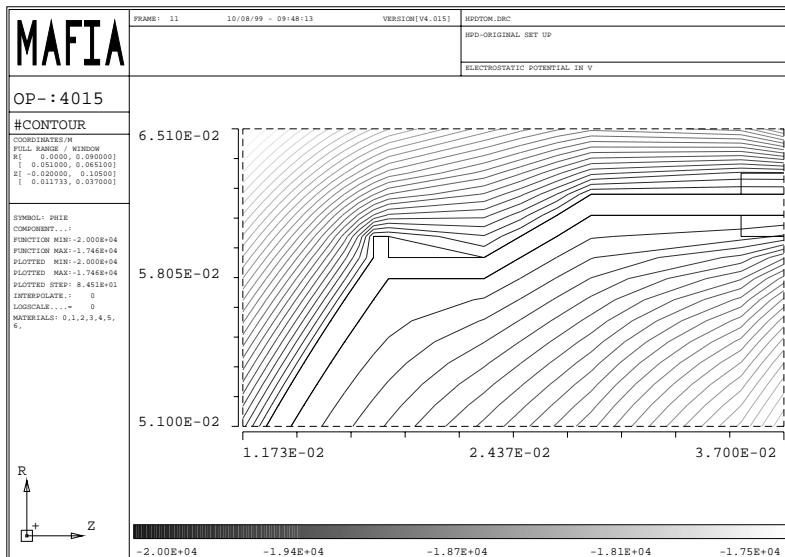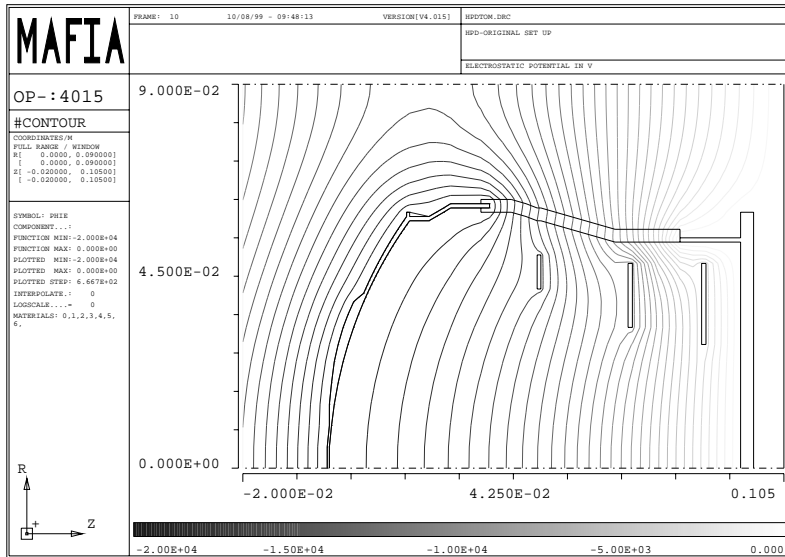
Figure 5.3: Focusing electric field for the first design of the Pad-HPD. The zoom shows the field near the join photocathode-Envelope, where there are focusing problems.

4, far beyond the requested one.
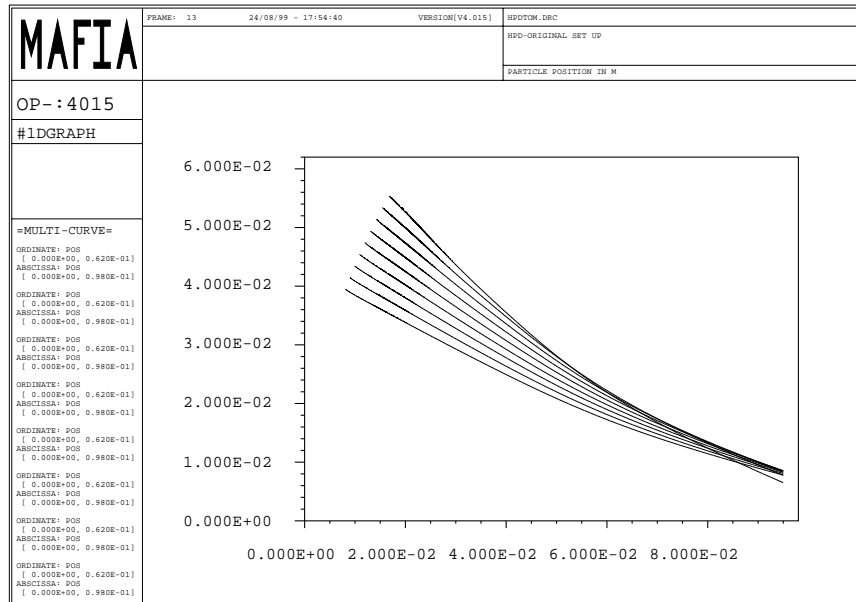
Figure 5.4: Trajectories of the photoelectrons outcoming

Hamamatsu proposed to set to 0 kV all the three electrodes. This solution was not satisfactory (Fig 5.5), therefore new designs have been planed.

The first try was simply to reduce the size of the skirt. In Fig 5.6 is shown the field in the critical region and the trajectories of the external photoelectrons. The situation is slightly improved already with the original voltage setting, but not yet satisfactory. Therefore two other solutions were investigated:

- add a fourth electrode to better shape the field in the critical region;

- reduce the size of the skirt and try to shape it in a different way.

Fig 5.7 shows the electrical field and the trajectories of the usual photoelectrons for a new design. This tube has four electrodes and a different skirt. There are no cross focused photoelectrons and the demagnification factor remains between 2.5 (photoelectronemitted at r=55.2 mm) and 2.3
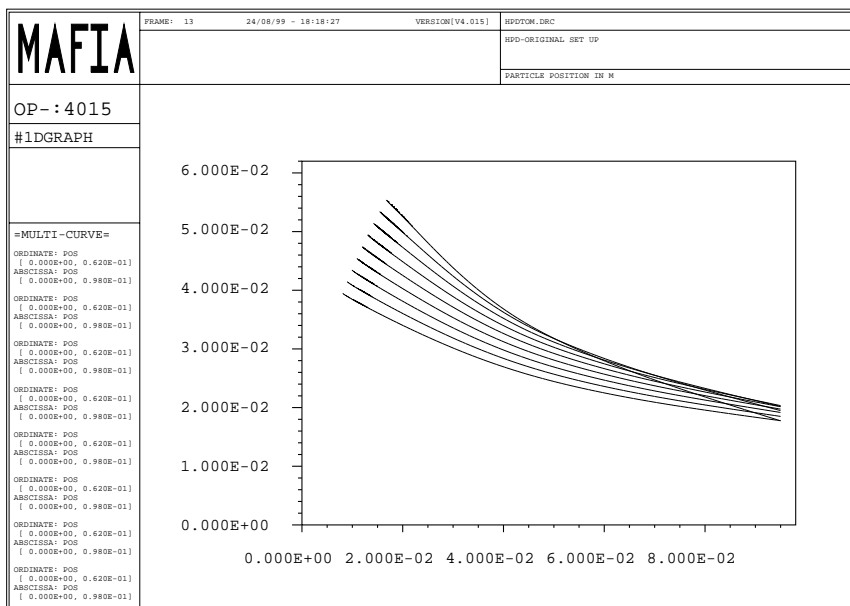
Figure 5.5: Trajectories for the setting proposed by Hamamatsu: photocathodeat 20 kV and all the electrodes at 0 kV.

Electrode	HV (kV) mod. A	HV(kV) mod. B
photocathode	-20	-20
Small	-16.5	no
1st	-12.5	-17
2nd	-7	-10.9
3rd	-3	-4.7

Table 5.1: H.V. for the HPD of Fig 5.7 (mod. A) and Fig 5.8.a (mod. B).

(photoelectronemitted at r=40 mm), as requested by the size of the silicon detector. In Tab. 5.1 the potential at which every electrode is set are reported (model A).

The search of simplicity led to the last HPD design tested with MAFIA. This design had only three focusing electrodes. These are slightly inclined to better shape the electrical field and in a different position with respect to the previous ones (Fig. 5.8.a). The photoelectrons emitted at $r \leq 55.2$ mm (Fig. 5.8.b) are rightly focused – a slightly excessive demagnification is still present for the most external trajectories. The optimized voltage of the electrodes are listed in Tab. 5.1.

Another computation has been made to have an estimate of the spread of the photoelectrons on the silicon detector. A bunch of 9 photoelectrons with an initial energy of 1 eV and a uniform angle distribution between $\pm 45^o$ is emitted[1] from the photocathode at $r = 22$ mm, about one half of the active radius (see Fig 5.9).

The final total spread is ± 0.5 mm, but it must be considered that the photoelectrons are created in the simulation in a point situated slightly before the photocathode surface. It turns out that when they pass through the photocathodesurface they are already slightly separeted. Their initial spread is ± 0.1 mm. That means that the final spread is ± 0.4 mm, which is the same value we get from Eq. 5.1

For mechanical reasons this design could not be realized: in order to join the glass envelope with the photocathode the metallic skirt had to be longer.

At this point the simulations were no more carried out by the author, and a new software was used (SIMION).

In order to shape the electrical field in the critical region a fourth elec-

---

[1]Note that all the photoelectrons are emitted in the $z - r$ plane, i.e. what one gets is the meridian point spread function.
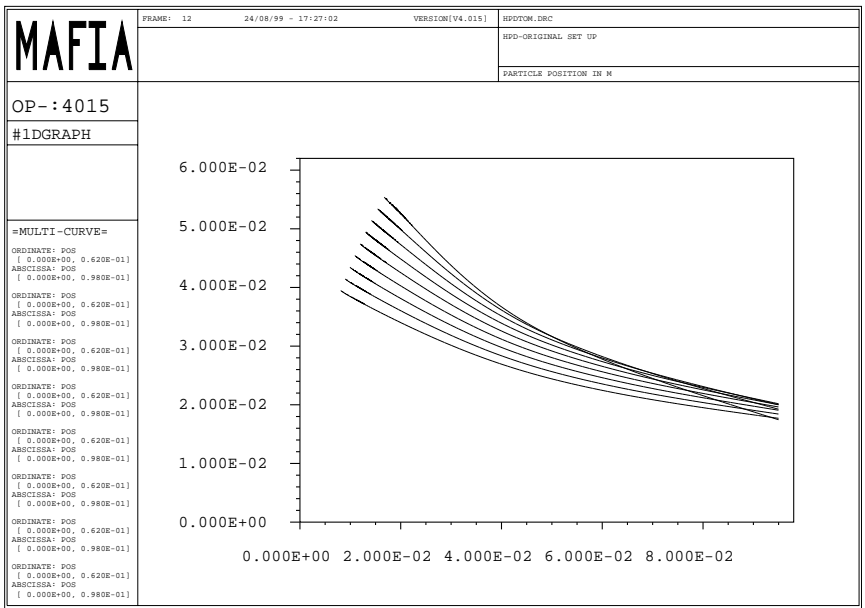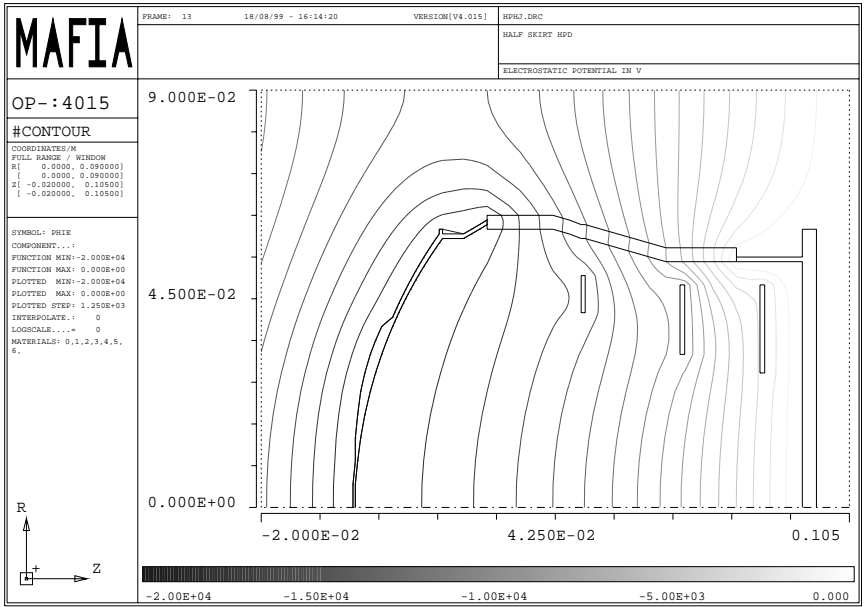
Figure 5.6: Trajectories of the photoelectrons outcoming
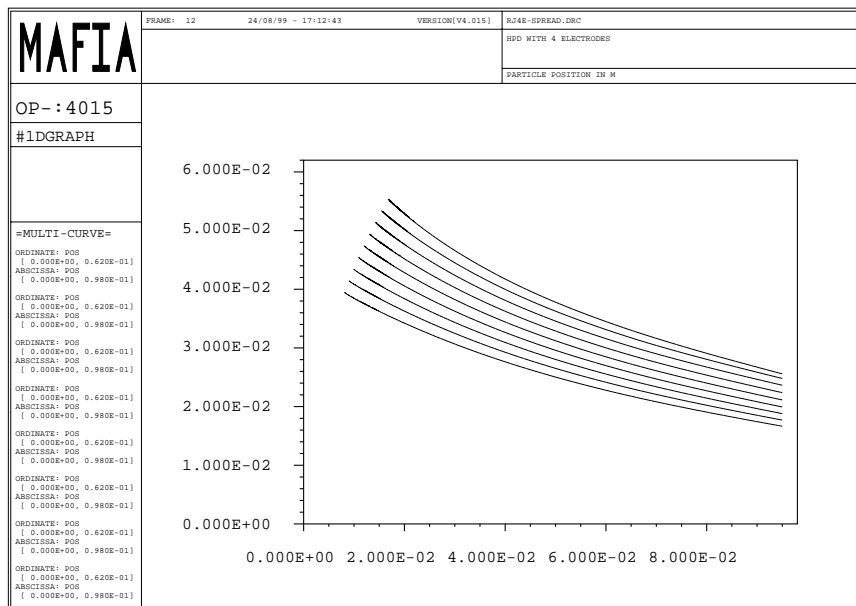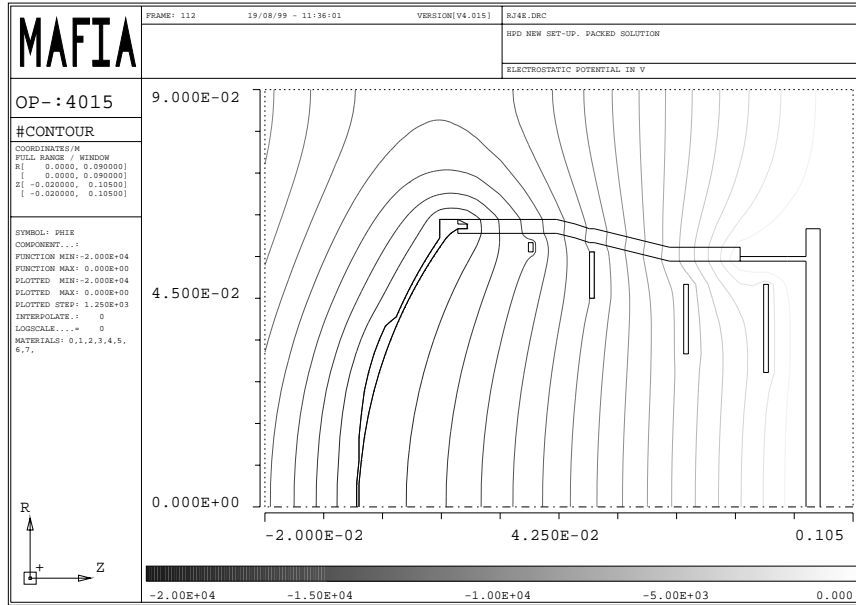
Figure 5.7: First working design. New shape of the metallic join between photocathodeand glass evelope and four focusing electrodes.

a)

b)
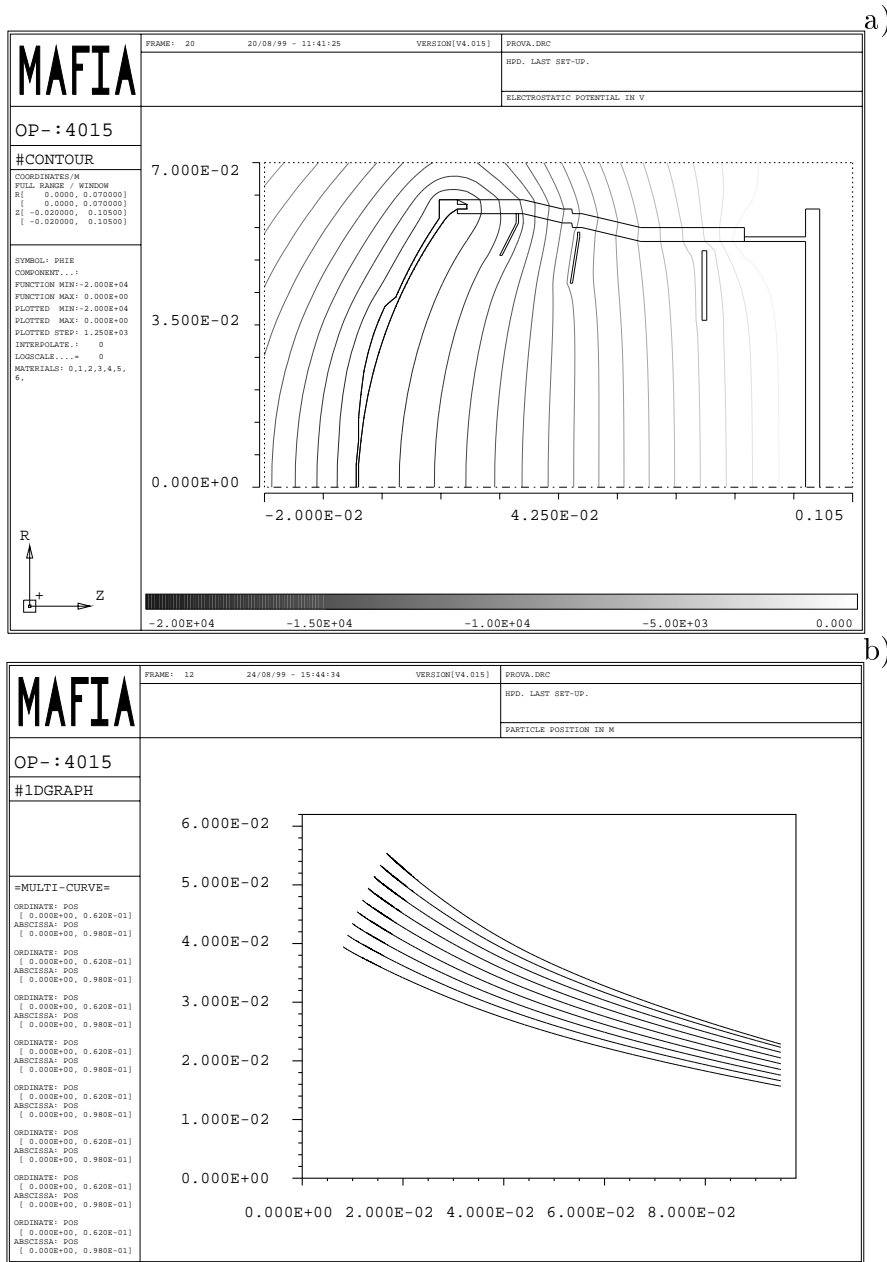
Figure 5.8: Last design. The metallic join between photocathodeand glass evelope is the same as the previous picture but number and shape of the electrodes has changed.
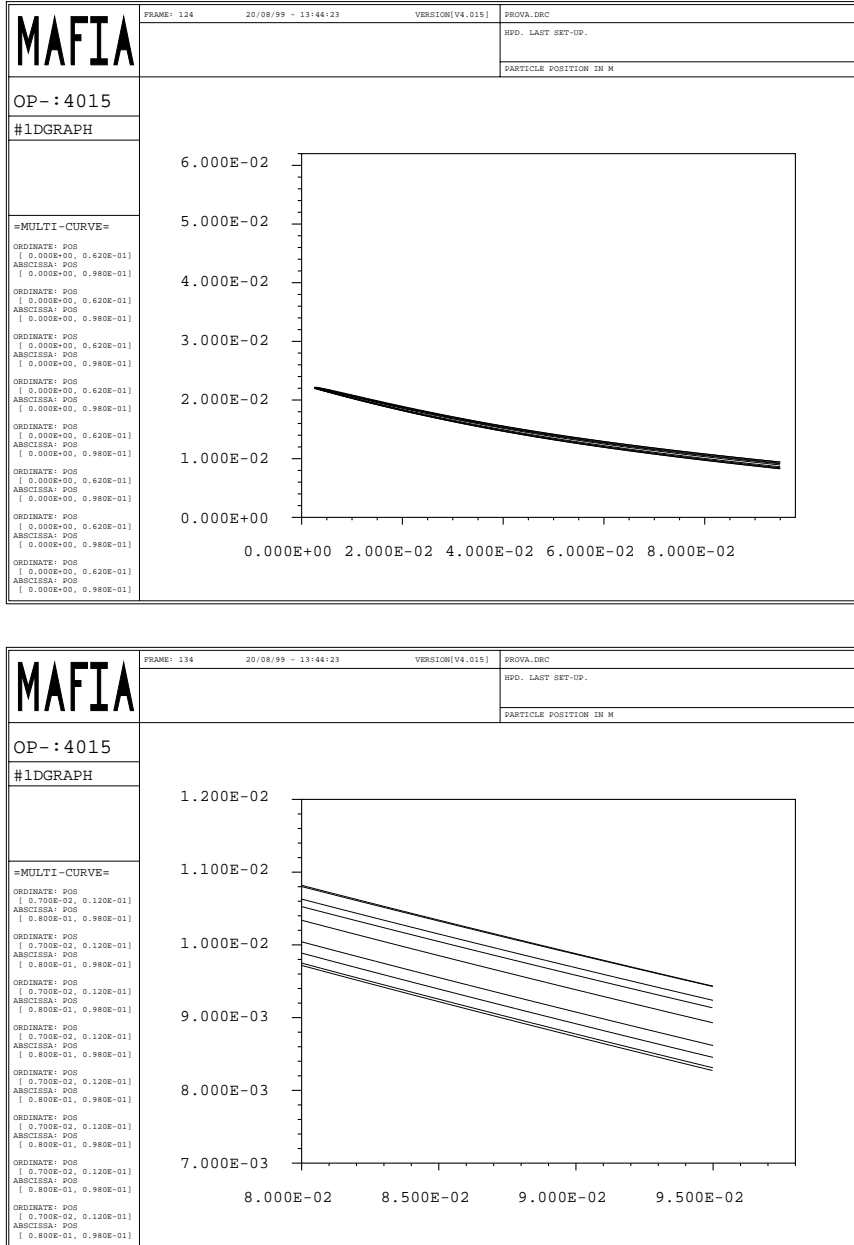
Figure 5.9: Ppoint spreaad function of the last design.

trode has been added[4]. This design (Fig. 5.10) shows the same focusing characteristics as the one in Fig. 5.8, with the advantage that the electrical field near the photocathode is better shielded from the influence of external fields. The experimental results [5] are in very good agreement with the simulations.
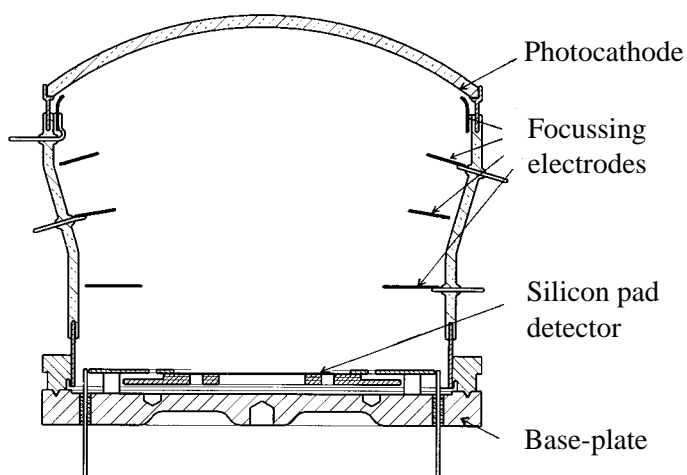
Figure 5.10: Present design of the Pad HPD.

Bibliography

[1] R. DeSalvo *et al.*, Nucl. Instr. and Meth. A 315 (1992) 375.

[2] LHC-B Week–10-14 February 1997 *enough as reference??*

[3] MAFIA is a product of the CST GmbH, Lauteshlaegerstrasse 38, D-64289 Darmstad. WWW: *http://www.cst.de* or *http://www.info.cern.ch/parc/mafia/*

[4] D. Ferenk *Poceeding on Erice workshop on new detector* (Nov 1997), World Scientific, in press

[5] LHCbNote 98-037

Chapter 6

Magnetic Shielding

The two RICH detector of LHCb are placed in a low magnetic field regions. Low magnetic field is important for two reason: the tracks should not curve appreciably whilst passing through the radiators and all the available photon detectors have a loss of efficiency if operating in magnetic field. In the region of RICH2 the B field will be in the order of 10 mT (100 G). The support of the photodetectors must therefore provide an effective magnetic shielding.

This chapter describes the work done to find an optimal solution for the photodetectors housing of RICH2. Section 6.1 explains the starting ideas, Sec. 6.2 the iterations from the first model until the conception of last model. Sec. 6.3 compares simulation data with prototype measurements. In Sec. 6.4 new simulations are done, with new input from prototype data and technical constraints. Then the new geometry proposed for RICH2 by the RICH group is described.

All the simulation are carried out using gauss (10^{-4} tesla) as unit for the magnetic flux density, and oersted (79.577 ampere per meter) for the magnetic field strength.

6.1   Multiple shell shielding

Computations of the magnetic shielding propriety of different photodetectors housing has been performed with MAFIA [1].

Nevertheless, before the computer aided analysis, an analytical approach was considered.

Differential equation coming from magnetic shielding problems can be

solved analytically only for geometry with a high degrees of symmetry, like spheres or infinite cylinders, and for material with linear relative magnetic permeability. This is not the case in the present work. Nevertheless, some analytical results [2] have direct implication on this work:

1) Although the thicker the shell becomes, the better the shielding effect is, the deflection of magnetic flux is greater for a thin shell. It is therefore unwise to make the thickness large in order to achieve a high shielding effect. Judging from the fact that the bending of magnetic flux is most pronounced along the inner boundary of the shield, one may see that more efficient shielding can be achieved by making use of multiple shells;

2) Once one has decided to use multiple shells, one has to optimize the thickness of the shells with respect to the interspace between them. In case of three concentric spheres the most efficient shielding is obtained when the interspace between them is equal to their thickness;

3) In order to better direct the field flux, we should avoid layers perpendicular to the field direction.

Even if for RICH2 a spherical shielding would be impossible, this results has been extrapolated to our case because the symmetry of the problem leads to assume that, in average, this is the best solution.

6.2 First model

The whole detector of LHCb is described in Chap. 1. A first tentative design of the photodetector housing is included in the technical proposal and shown in Fig. 6.1[1]. The material we have chosen is soft iron. The magnetic permeability μ used is the one labeled μ_A in Fig.6.2

The dipole magnet produces a field in the y direction, therefore for symmetry reason the field must be parallel to y in the plane $y = 0$. At the time when this work was started the magnet design was still at a very preliminary stage. The B field predicted in this region by the magnet group is in the

---

[1]The references axis we chose are different from the axis used in the official design. To get it: $x_{used} = -z_{official}, z_{used} = x_{official}$.
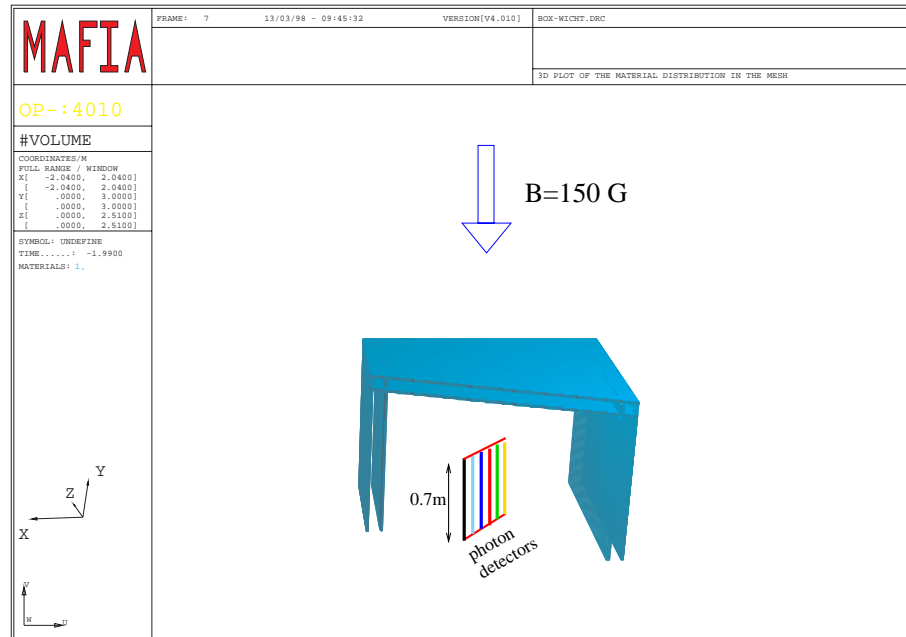
Figure 6.1: The original design. The external B field, of 150 gauss, is along y. The residual field along the seven raws drawn on the photodetector plane is plotted in Fig. 6.4.
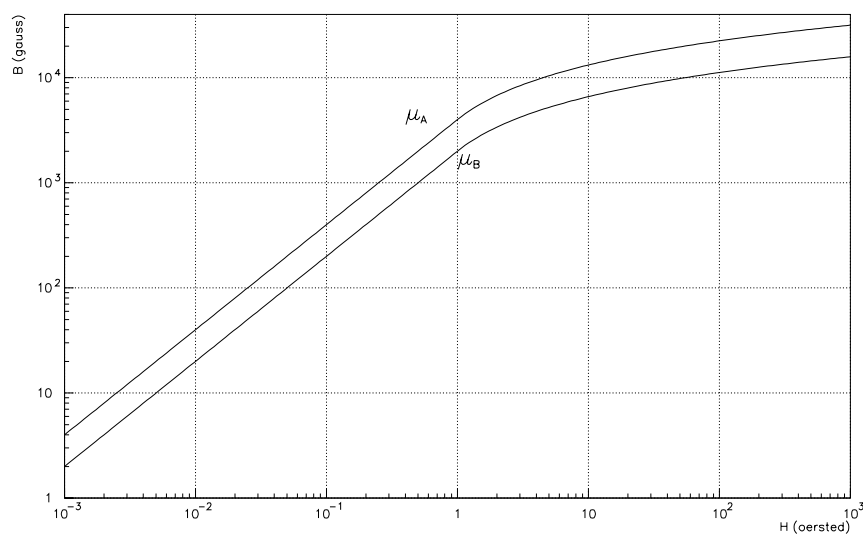
Figure 6.2: Magnetic permeability of soft iron used for the simulations. μ_A is 2000 before saturation, μ_B 4000. μ_B was used instead of μ_A after the comparison of the data of the simulation with the ones of the scaled prototype.
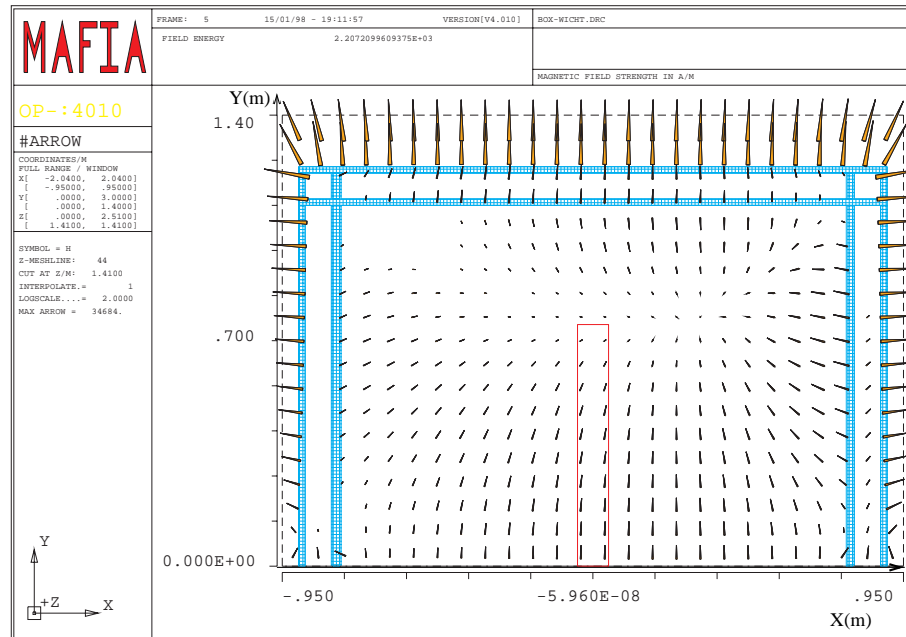
Figure 6.3: Residual B field distribution in the original design (Fig. 6.1). The plane of the section is perpendicular to z and intersect in the middle the photodetector plane. The external field is of 150 gauss along y.

order of 100 gauss. Therefore all the simulation were done with an external B field of 150 gauss along y.

The result of the first computation are in Fig. 6.3 and 6.4. In Fig. 6.3 the logarithm of the B field is shown with arrows. It can be seen that the field at y=1.15 m, near the roof, has changed direction. The field flux has to escape from the material near $x = 0$. Some of the flux escape from the top, some from the bottom.

The flux escaping from the bottom has opposite direction to the external field, therefore there is a region, near the roof, where the field is very low. This is shown in Fig. 6.4. In this figure the value of B (in gauss) versus y for six different rows of photodetectors has been plotted. The magnetic field has a minimum at $y = 0.8$ m (the photodetectors should be installed up to $y = 0.7$ m).

This is a very unstable solution as it is highly dependent on the local geometry. The first optimization was done to determine the number of layers

Figure 6.4: Residual B field (on the ordinate in gauss) vs. (on the abscissa in meter) y for different rows of photodetectors calculated for the original design (Fig. 6.1). The external field is 150 gauss along y.
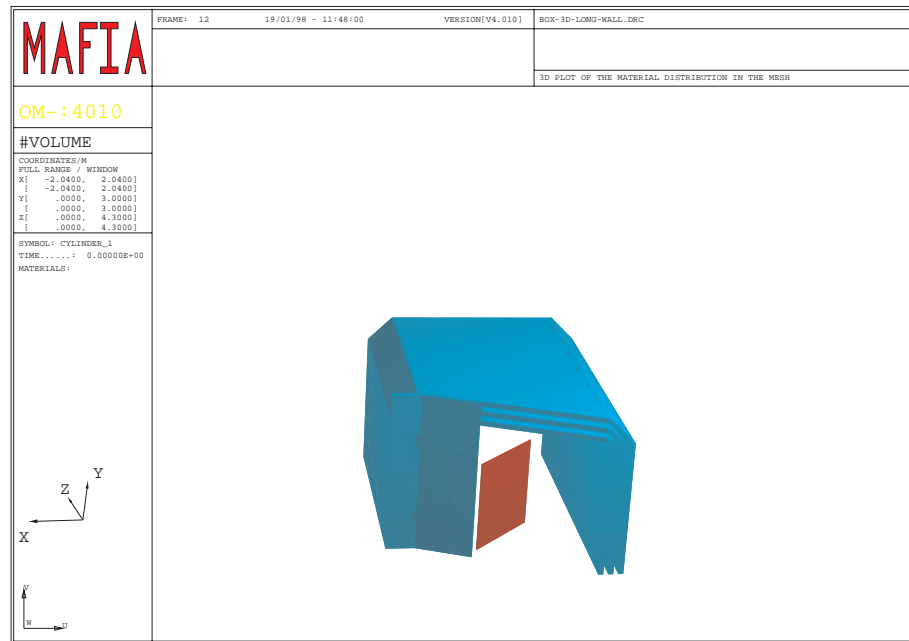
Figure 6.5: Box extended for 1 meter along z, 90° edges substituted by 45° edges. Wall in front added.

to use. We tested housing with 2, 3 and 5 shells instead of the 2 of the original design. The more robust shielding is achieved for 3 shells.

After that the shape of the box was changed as in Fig. 6.5. The thickness of the shells is 4 cm as the interspace between them. Each of the 90° edges has been substitute from two 45° edges. The box has been extended 1 meter in the z direction. An additional wall near the photodetectors has been added. The results of the simulation are shown in Fig. 6.6 (without the additional wall) and Fig. 6.7 (with the additional wall). The shielding effect is stronger and more uniform for the latter solution.

The additional wall is necessary to get a field to less than 20 gauss for the most external row of photodetectors.

The last model is shown in Fig. 6.8. The flat roof perpendicular to the external field has been substituted by a 45° oblique triangular roof. This allows an optimal funneling of the magnetic field.

The residual B field is shown in Fig. 6.9. This is a uniform and stable
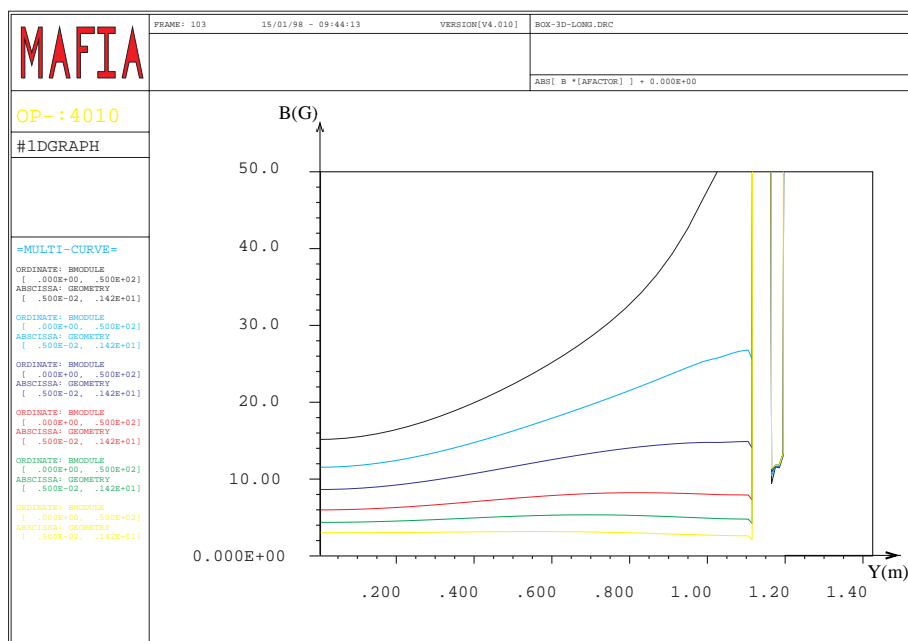
Figure 6.6: Residual B field (on the ordinate in gauss) vs. (on the abscissa in meter) y for different rows of photodetectors in the box of Fig. 6.5 without the wall in front. The external field is of 150 gauss along y.
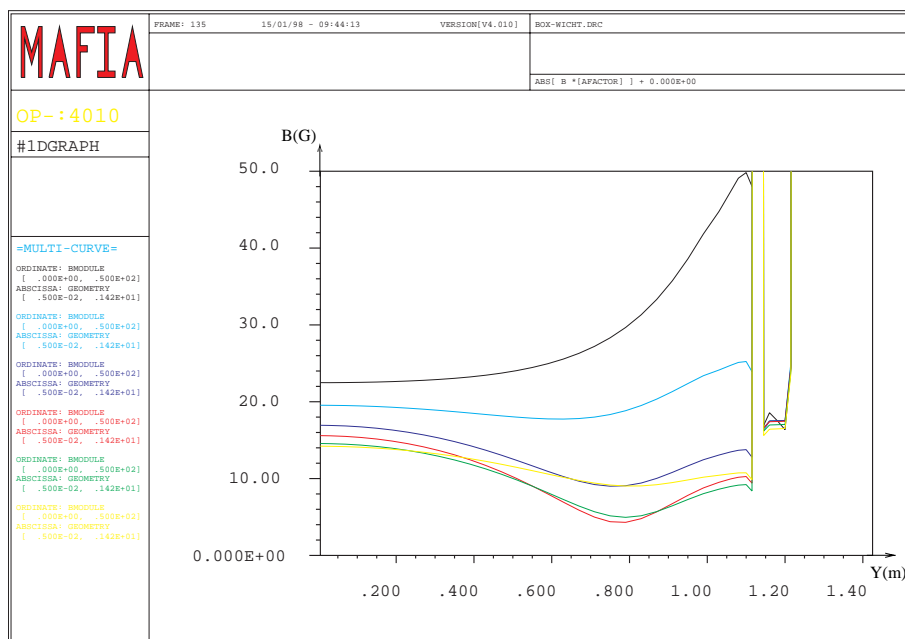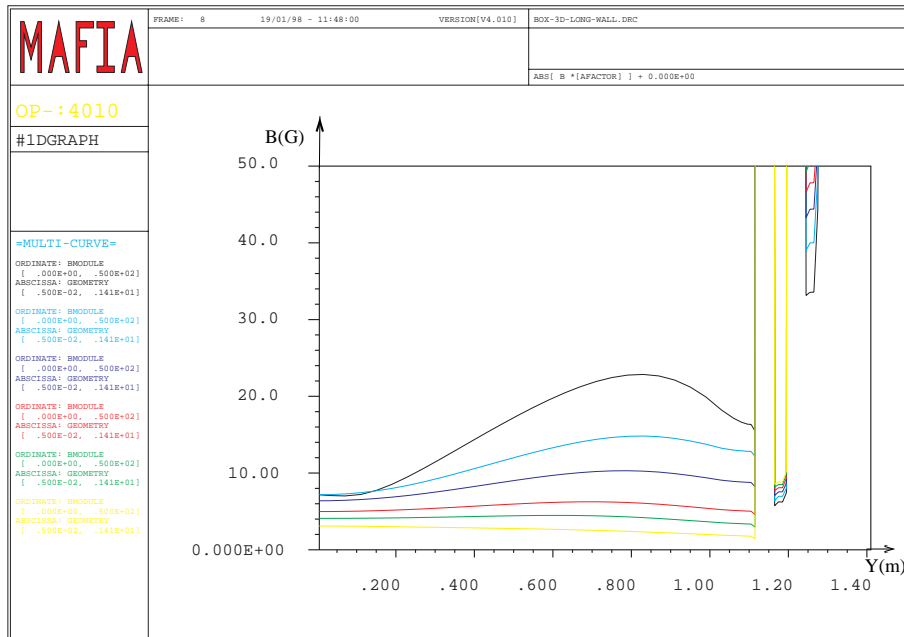
Figure 6.7: Residual B field (on the ordinate in gauss) vs. (on the abscissa in meter) y for different rows of photodetectors in the box of Fig. 6.5. The external field is of 150 gauss along y.

solution with a reduction factor of 15.

The main characteristics of the different models are in table 6.1.

Proj. nbr:	# of layers	thick. of layers (cm)	interspace (cm)	Other characteristic
1	2	1.5	10	-
2	3	4	4	smoothed angles, +1 m along z
3	3	4	4	as 2, front-wall, +1 m along z
4	3	4	4	house shaped, front-wall, +1 m along z

Table 6.1: Property of different photodetector housing.

The computation for the shielding effect on 50 G transverse field has been performed. The residual B field is shown in Fig. 6.10 for an external field along x (parallel to the beam axis) and in Fig. 6.11 for an external field along z (perpendicular to the beam axis). The shielding is very good for B parallel to x (the residual field goes from 1 to 3 gauss). It is not as satisfactory for B parallel to z (the residual field goes from 6 to 25 gauss). Therefore a further study has to be carried out in case the z-component of the magnetic field in the detector will be greater then 20 gauss.

Fig. 6.12 summarize the evolution of the models, showing for each design the range of the residual B field in the region of the photodetectors plane for an external field of 150 gauss along y. The optimal solution is clearly the last design (Fig. 6.8). Therefore a scaled prototype 1:8 was build and measured.

6.3   Prototype results

In Fig. 6.13 are shown the three different shells produced for the scaled prototype. They are 0.5 cm thick and the interspace between them has been fixed to 0.5 cm in different point by many small bricks of aluminum. The material used is soft iron[2]. The front wall has not been included.

This prototype was tested at the DELPHI experiment, using the residual field of the DELPHI magnet as external field of 130 gauss.

---

[2]SCEM: 44.50.050.8 on the CERN catalog.
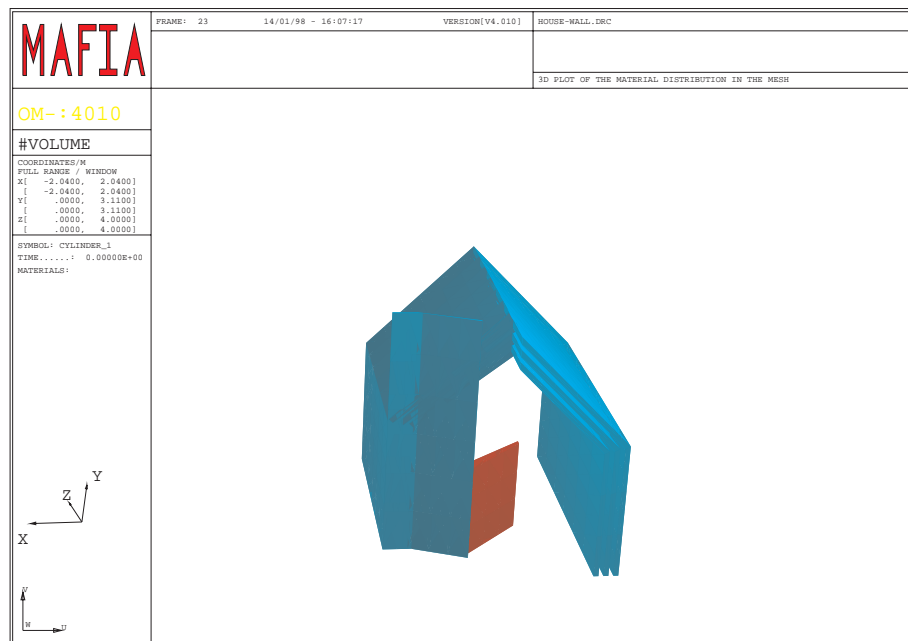
Figure 6.8: House-shaped box (last project). In red (black) the photodetector plane
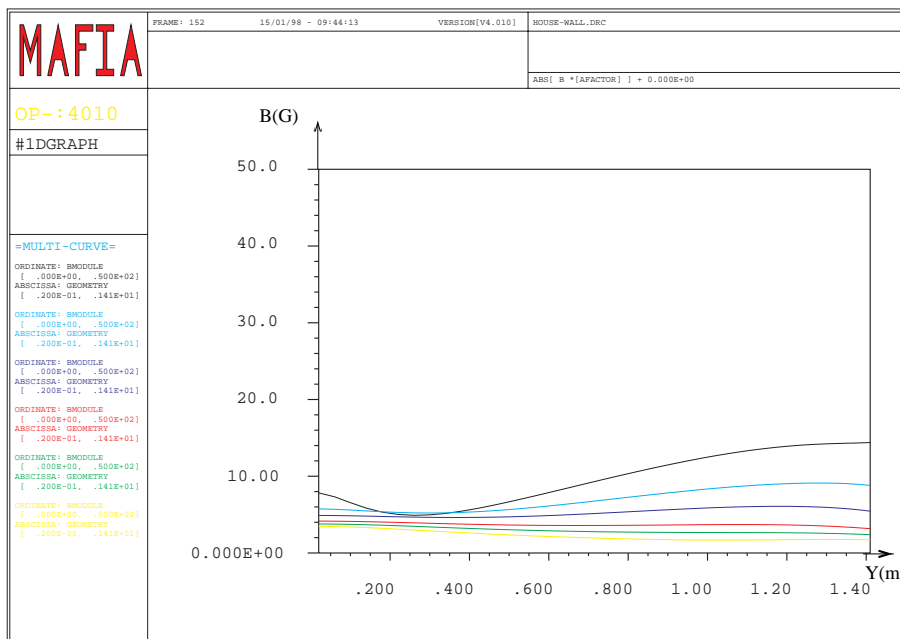
Figure 6.9: Residual B field (on the ordinate in gauss) vs. (on the abscissa in meter) y for the box of Fig. 6.8. The external field is of 150 gauss along y.
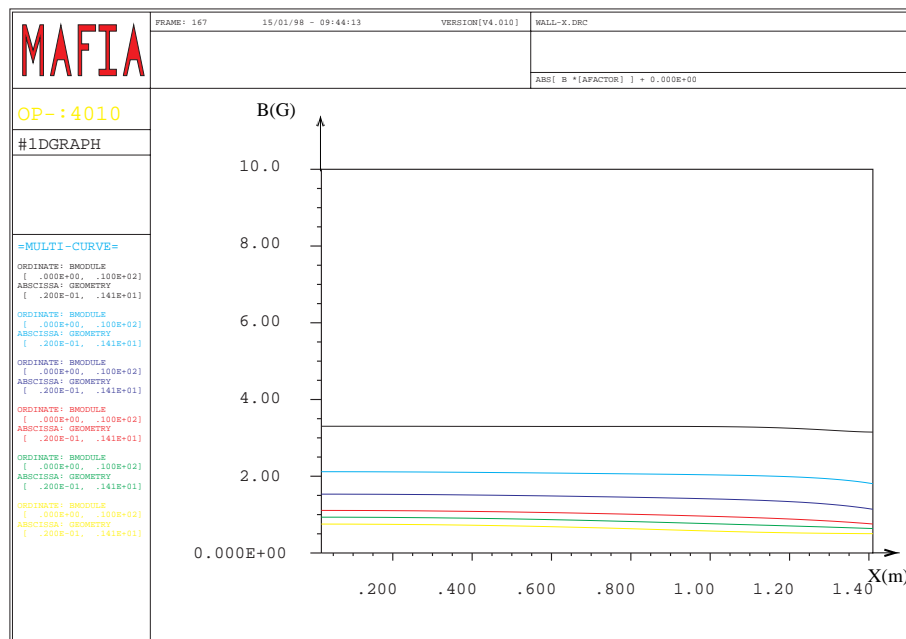
Figure 6.10: Residual B field (on the ordinate in gauss) vs. (on the abscissa in meter) y for the box of Fig. 6.8. External field of 50 gauss along x
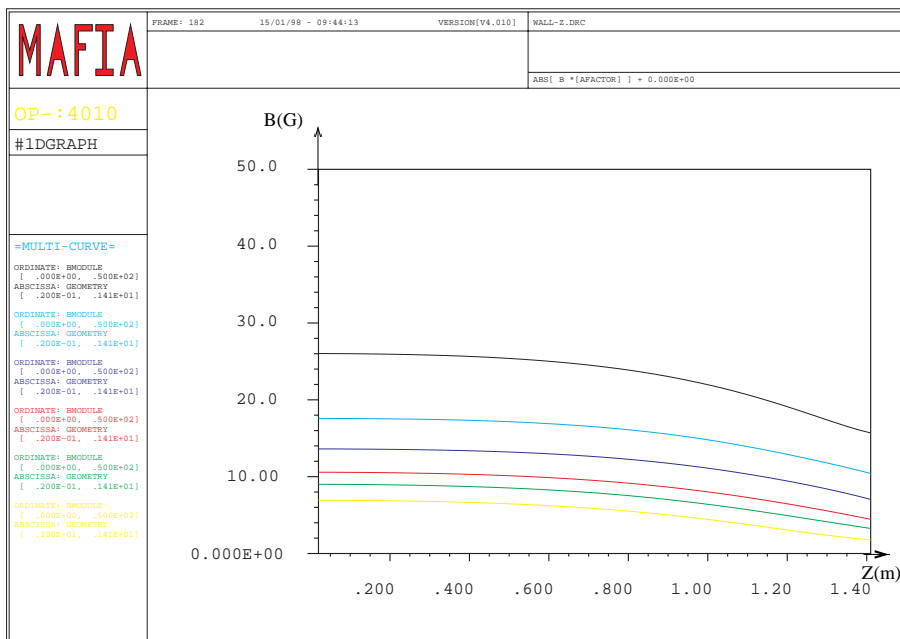
Figure 6.11: Residual B field (on the ordinate in gauss) vs. (on the abscissa in meter) y for the box of Fig. 6.8. External field of 50 gauss along z
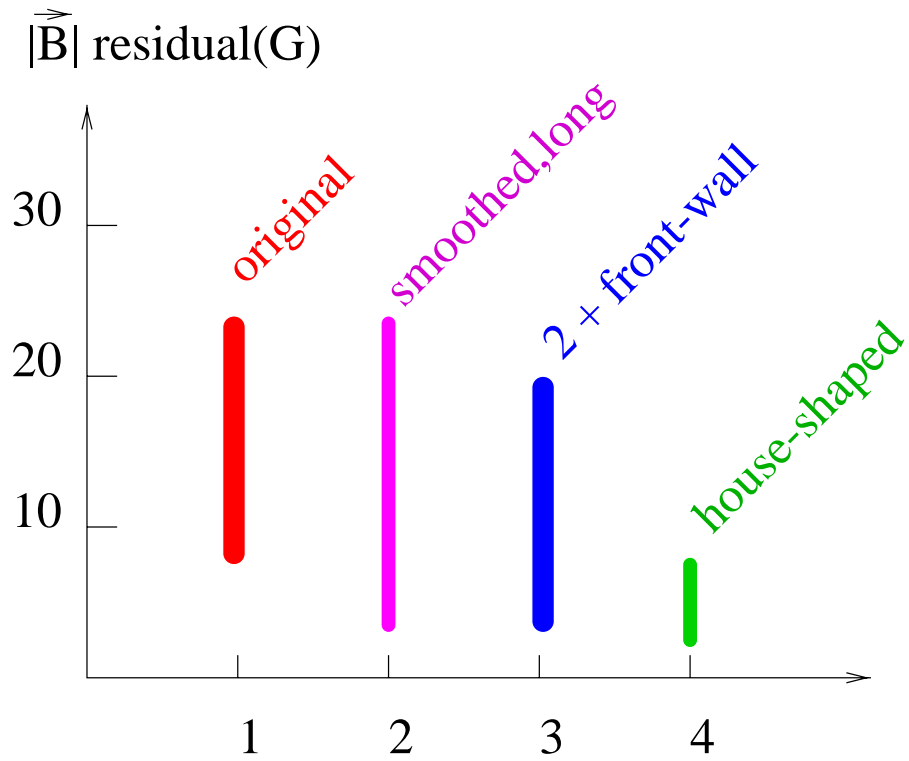
Figure 6.12: Evolution of the models. Range of variation of the residual B field in the region of the photodetector plane. The external field is of 150 gauss along the y direction. 1 → Fig. 6.1, 2 → Fig. 6.5 (without wall in front), 3 → Fig. 6.5, 4 → Fig. 6.8.

The shielded field was measured on two matrix of 5×4 points laying on two different plane parallel to the external field direction.

The measurements are shown in Fig. 6.14: $|B|$(gauss) is plotted for the 20 points on the two planes. On the same picture there is the results obtained with MAFIA imposing the same external field and using a magnetic permeability $\mu = \mu_A$ ($\mu_A = 4000$ before saturation, see Fig. 6.2). The shape of the fields is similar. In the simulation the shielding factor is almost twice that of the measurements. Therefore the magnetic permeability has been changed in order to have a better agreement. For $\mu = \mu_B$ ($\mu_B = 2000$ before saturation, see Fig. 6.2) the difference between calculation and measurement is marginal (Fig. 6.15). Therefore for any further simulation $\mu = \mu_B$ has been used.

6.4   Adjustment of the geometry of RICH2

The last simulation carried out had to take in account new informations:

- The last magnet design, still not the final one, showed that the field in the RICH2 region has a vertical component of about 45 gauss and a non zero component along the other two direction.

- The engineering design of RICH2 has reached a more advanced stage, giving new constraints to the shape of the magnetic shielding.

Therefore a new external vertical field of 90 gauss has been imposed and the design slightly modified: the interspace between the middle and the external layer has been changed from 4 to 10 cm, all the layers have been reduced by 50 cm along the z (Fig. 6.16).

It was important, at this stage, to estimate the field in the photodetectors region in order to find an optimal position for them. In Fig. 6.17 there is a contour plot of $|B|$ on two horizontal planes. The first is placed in the symmetry plane and the second at the maximum hight of the photodetector plane (y=70 cm). It is clear that photodetectors placed on the limit of the 300 mrad horizontal acceptance are in a critical position (Fig. 6.18: the most external column of photodetector sees a magnetic field ranging from 15 to about 25 gauss).

The geometry of RICH2 proposed in the LHCb Technical Proposal was for a pure ideal detector: it was not taken into account the thickness of the gas vessel walls and of the mirror supports, the space for the front-end
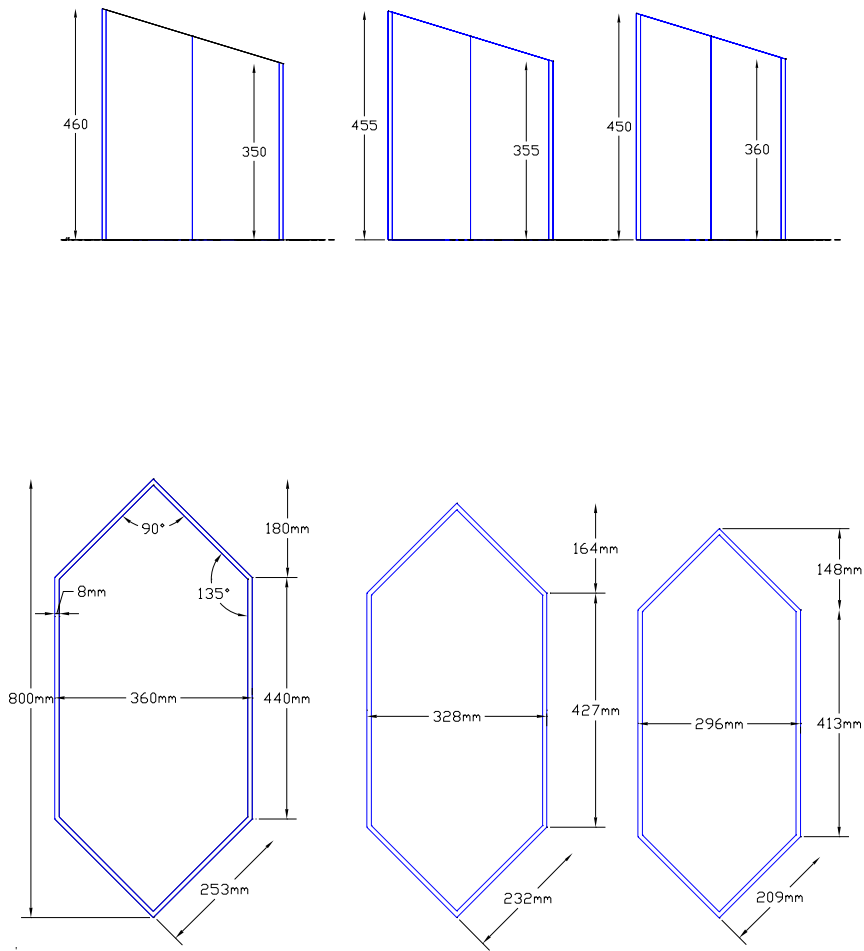
Figure 6.13: Dimension of the scaled prototype 1:8 tested with 130 gauss.
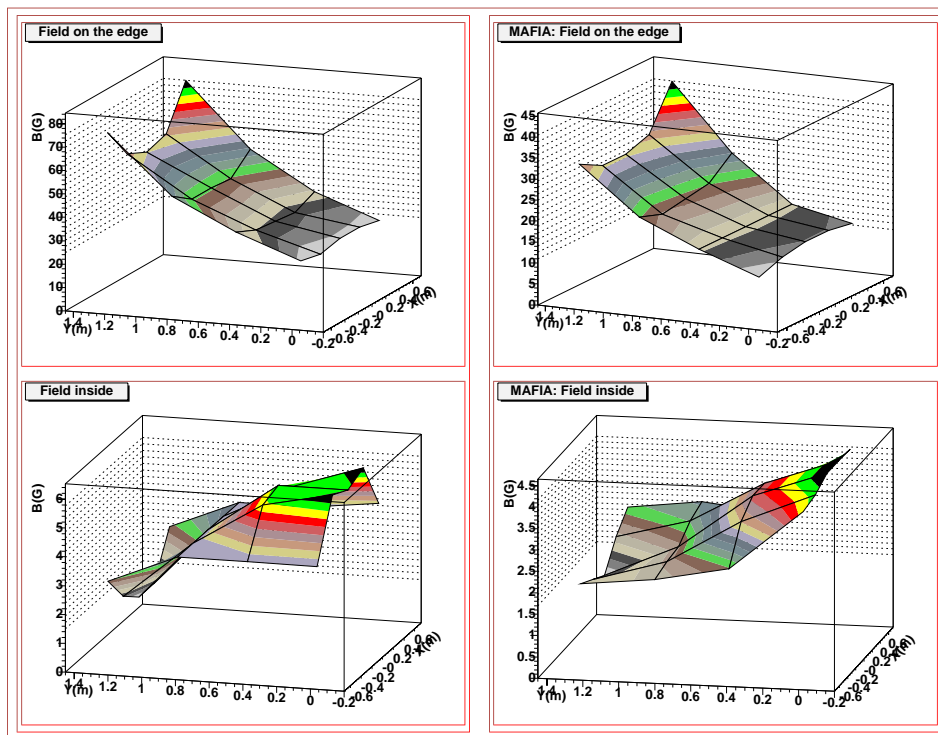
Figure 6.14: Shielding properties of the prototype: measured (left) and simulated (right). On the z axis the residual field in gauss is plotted. The magnetic permeability used is μ_A.
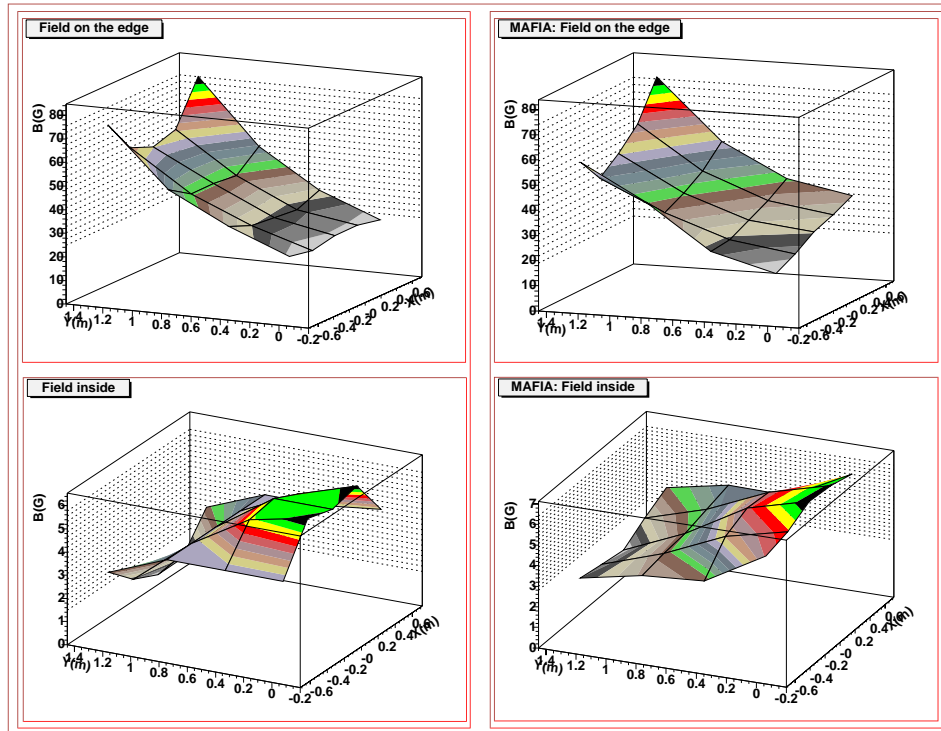
Figure 6.15: Shielding properties of the prototype: measured (left) and simulated (right). On the z axis the residual field in gauss is plotted. The magnetic permeability used is μ_B.
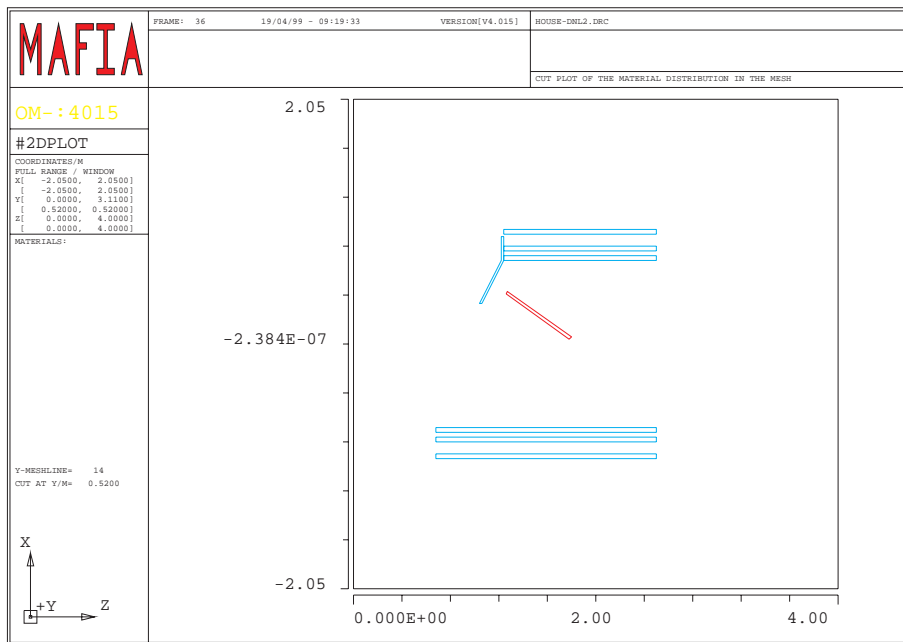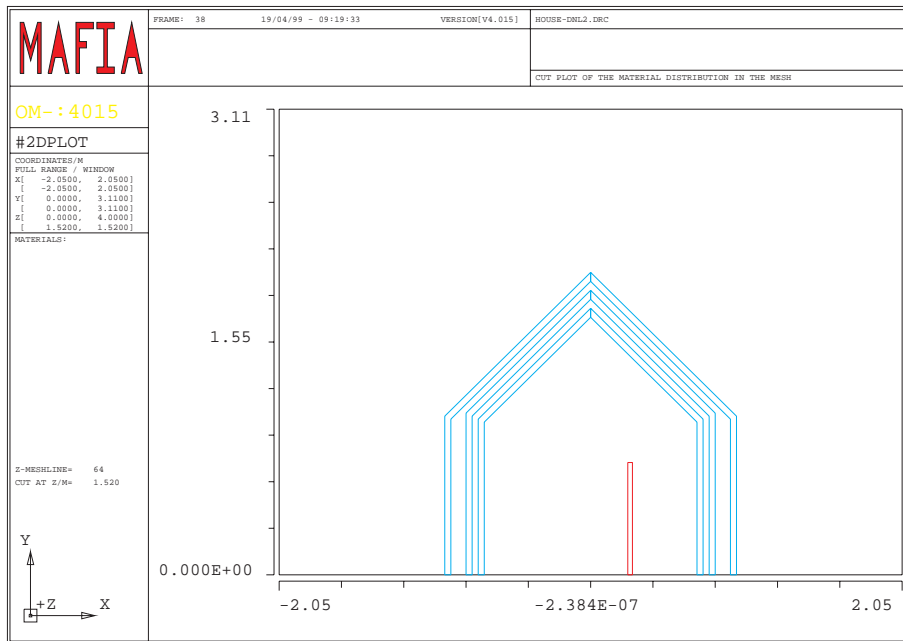
Figure 6.16: z and y cut of the last design simulated: for mechanical reason the interspace between the middle and the external layer has been changed from 5 to 10 cm.
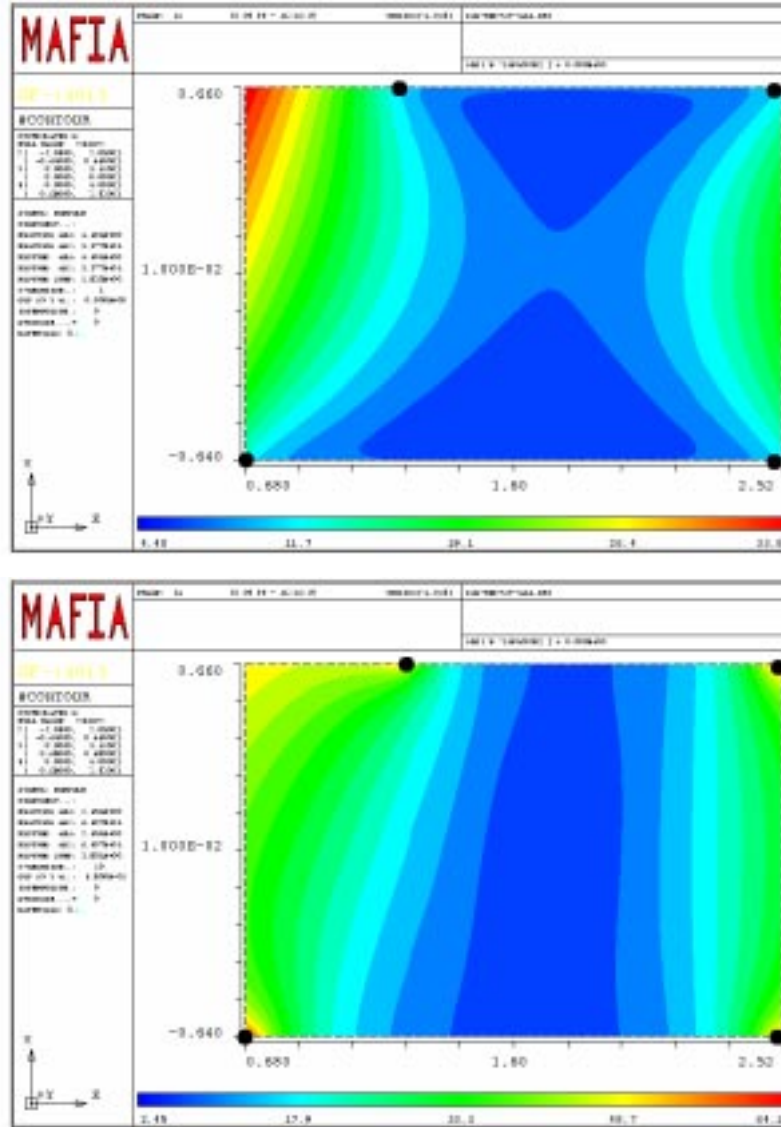
Figure 6.17: Value of $|B|$ for two $y = 0$ (the symmetry plane) and $y = 70$ cm (the hight of the photodetector plane). The four edges of the box are indicated with the black spots. The underlying color table indicates the field in gauss.
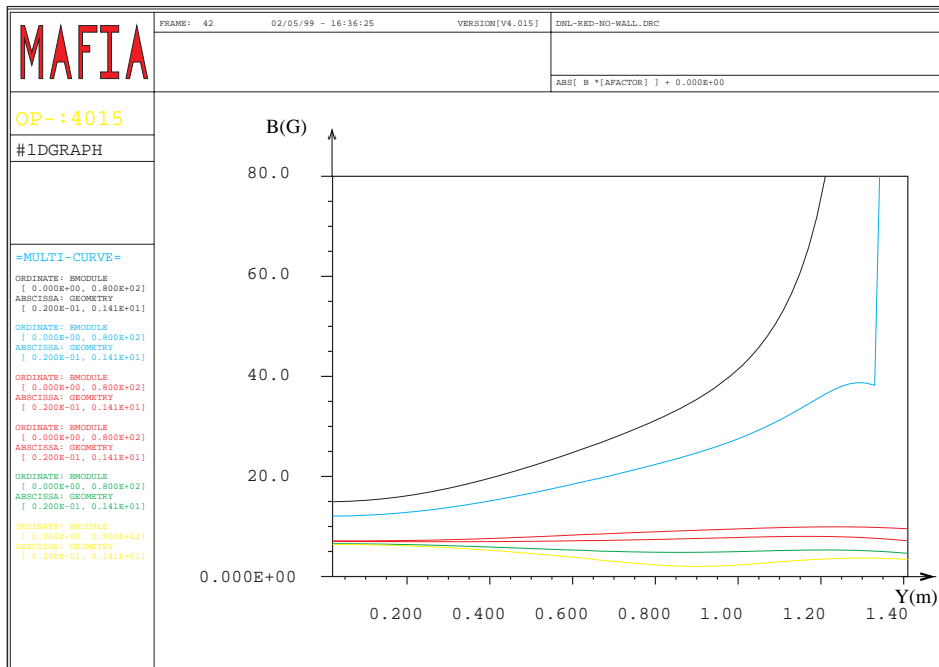
Figure 6.18: Residual B field (on the ordinate in gauss) vs. (on the abscissa in meter) y for the last design. The position of the photodetectors is the one of the technical proposal.

electronics of the photodetectors, and the location of the former was as close as possible to the acceptance region, especially exposed to the fringe field of the magnet.

We have to consider that the magnetic shielding presented can not be considered as a final version. A field map was not available: the choice of a purely vertical field was made on symmetry considerations, but last estimates of the fringe field give horizontal component varying from 0 (on the symmetry plane) to 15 gauss (at y=50 cm).

Nevertheless this structure shows that the biggest component of the fringe field can be strongly reduced. It shows as well that the photodetectors near the acceptance region are in a critical position. To reduce the field seen by these detectors one can:

- put a wall along the 300 mrad acceptance as long as it does not disturb photon detection

- move the whole photodetector plane further inside the shielded volume.

All these considerations (mechanical problems and magnetic shielding) has lead to a new RICH2 geometry, shown in Fig. 6.19 (note that LHCb coordinate system is used).

6.5 Conclusion

The presented work proposes a solution for the magnetic shielding of ROCH 2. The used field map for the external field is symplified (but not irrealistic). It indicates as well which re-arrangement of the RICH2 geometry one has to do.

Figure 6.20 shows the magnetic field for the six rows of photodetectors with this new geometry (photodetector plane further inside and additional wall) for an imposed external field of 90 gauss. The field stays always below 7 gauss.
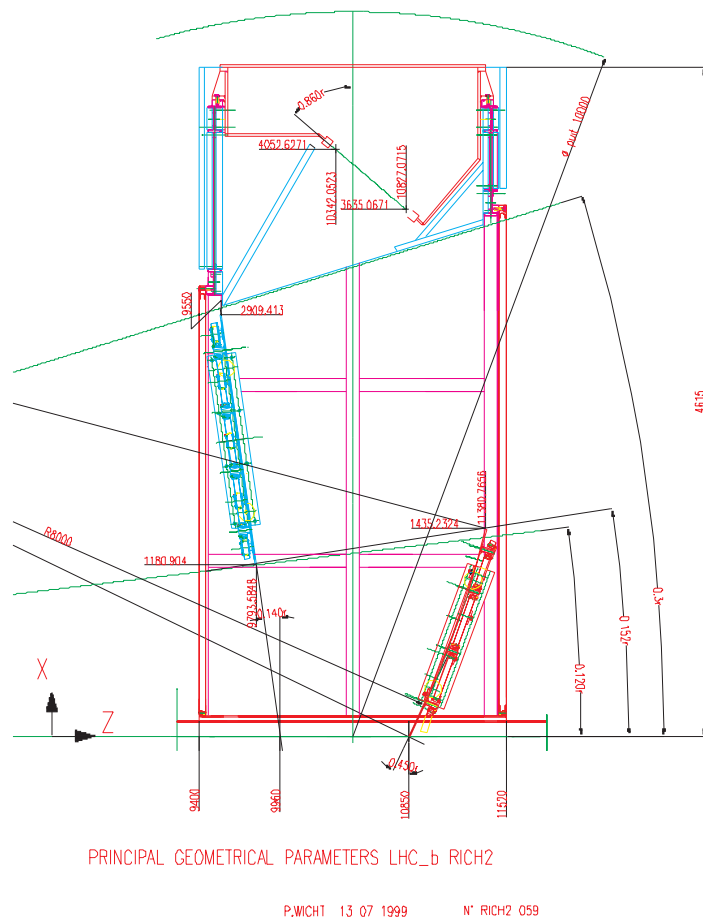
Figure 6.19: Last geometry proposed.
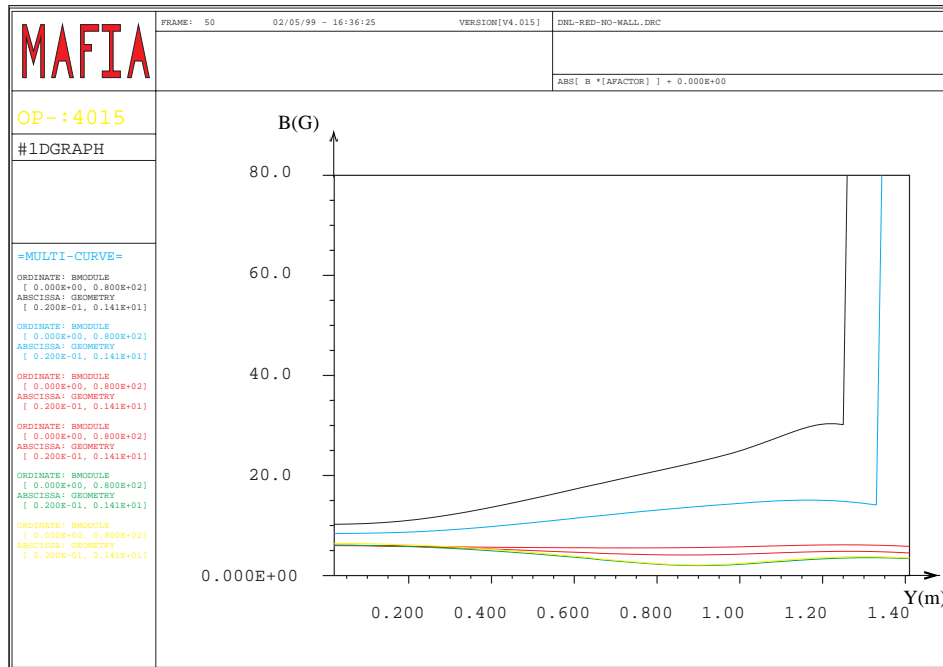
Figure 6.20: Residual B field (on the ordinate in gauss) vs. (on the abscissa in meter) y for the last design. The new position of the photodetectors is used (previous figure) and an external vertical field of 100 gauss is imposed.

Bibliography

[1] MAFIA is a product of the CST GmbH, Lauteschaegerstr. 38, D-64289 Darmstadt. WWW: *http://www.cst.de.*

[2] T. Rikitake, Magnetic and electromagnet shielding. Terra Scientific Publishing Tokyo, 1988.

Chapter 7

Half and Full scale Pixel HPD

The requirements for the photodetectors of LHCb where described in Chap. 3. Two research and development programs are carried out, oriented towards the manufacturing of HPD's optimized for this application. Pad HPD's are one option. In Chap. 5 is described the work made for the electrostatic configuration of these detectors and a general introduction about HPD's is also presented.

Pixel HPD's are the other option. They are based on a cross-focussed image intensifier tube geometry and are developed in close collaboration with industry (the Dutch Company DEP [1]). This option will be discussed here. In Sec 7.1 there are the result obtained on a half scale prototype; in Sec 7.2 are described the properties of the final 80 mm diameter design and the tests done on a tube equipped with a phosphor anode; the last section is dedicated to the analysis of a test-beam carried out in June 1999 with a RICH2 prototype with three Pixel HPD equipped with commercial 61-pixel anodes read-out.

7.1 The Half Scale Prototype

7.1.1 Characteristics

A half-scale cross-focusing prototype tube has been developed [3],[4], and is shown schematically in Fig. 7.1. Its input window is made of quartz and is 40 mm in active diameter. The photocathode is deposited on a spherical surface. The photoelectron image is focused onto the flat surface of a

silicon detector chip mounted in the die cavity of a standard ceramic car-
rier[1]. The silicon detector is a pixel structure bump-bonded to the LHC1
chip developed by the RD19 collaboration at CERN[2]. This comprises an
array of 128×16 pixel of 50×500 μm^2 giving a total silicon active surface
of 6.4×8.0 mm^2. The cathode is one-to-one mapped to the anode with a
factor of about 4.3 in demagnification. The granularity on the photocathode
is therefore about 0.2×2.0 mm^2. The nominal operating voltage of the tube
is 20 kV.
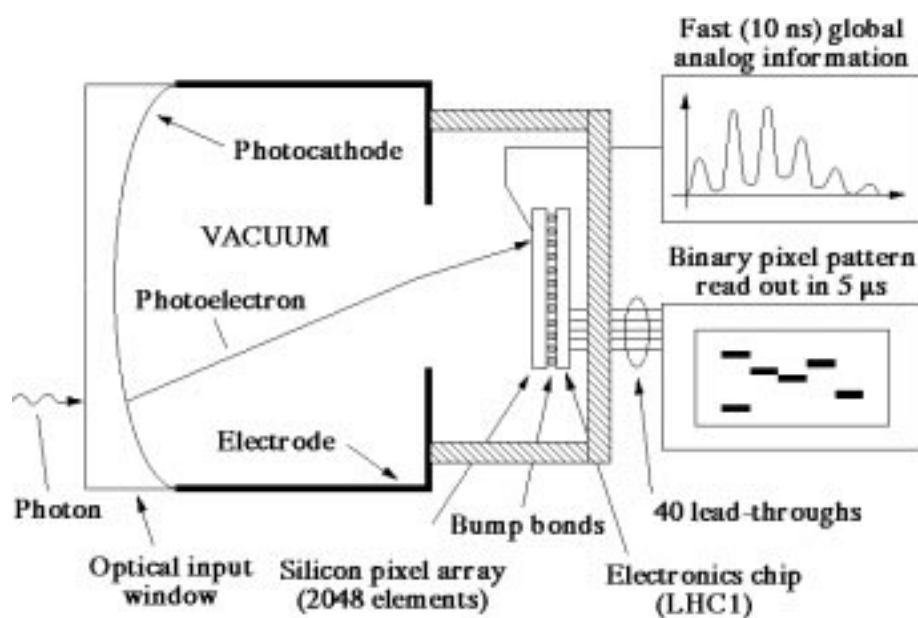
Figure 7.1: Schematic design of a 40:11 prototype tube. The electron optics
are based on a diode structure with cross-focusing. The anode is mounted
LHC1 chip comprising 2048 pixels 50×500 μm^2 and their associated front-end
electronics.

The LHC1 chip is being used for charged particle detectors. Each detector
pixel is individually connected to a read-out chain containing amplifier 100 ns
peaking time, a discriminator with a globally adjustable threshold and a
globally adjustable delay line with local fine tuning coincidence logic and
memory. Every cell can be individually addressed for electrical test and

---

[1]Kyocera Fine Ceramics, Japan

masking. The power consumption is below 50 μW per channel.

Electron optics simulation have been done at DEP and at CERN [4]. The demagnification factor is 4.7 near the axis and 4.0 at the edge. The point spread function for photoelectrons emitted near the axis is 32 μm.

Two tubes where successfully produced. Photocathode response was measured by DEP and was stable over two weeks. They have been used with an accelerating voltage of 20 kV without problems. No difference where observed for the performance of the electronics included in the tube before and after the encapsulation.

7.1.2   Photoelectron detection efficiency

Figure 7.1 shows the set-up used for the measurement of the photoelectron detection efficiency. Signal from the back-plane of the silicon detector anode were read out with an electronics chain consisting of an ORTEC 142A amplifier, an ORTEC 579 fast-filter amplifier and a SILENA multichannel analyzer. This analog information allowed measurement of the photoelectron signal spectrum. The light source consisted of a blue low-intensity LED operated in pulse mode. Figure 7.2 shows a typical spectrum with a detector bias voltage of 55 V and a tube high voltage of 20 kV.

The pixel detector was then read out by the LHC1 chip operating at minimum threshold setting 3000 e$^-$. 239 pixel had noise signal above threshold and were masked. 353 were inactive, due to bad bump bound connection or too high threshold. There are finally 1456 (71%) active pixel. The number of active pixels as function of the high voltage is shown in Fig. 7.3. This function differentiated with respect to the high voltage gives the threshold distribution (the number of pixel that becomes active for a given high voltage, see Fig. 7.4). This distribution has a Gaussian shape with an average of 10 kV (2800 e$^-$) and a standard deviation of 1.6 kV . A non Gaussian tale in the high threshold region is clearly visible.

The mean number of photoelectrons measured via the back plane is $\mu = 1.57$ (Fig 7.2). The probability that two photoelectrons hit in the same event the same pixel is $\approx 10^{-4}$ and can be considered zero, therefore the number of fired pixel per event gives the mean number of photoelectrons detected via the pixel detector. Figure 7.5 shows the number of fired pixel per event. The Poisson distribution fits very well ($\chi^2/\text{dof} = 5.9/9$) and gives a mean number of photoelectron $\mu' = 0.9$. Considering that there are 71% active
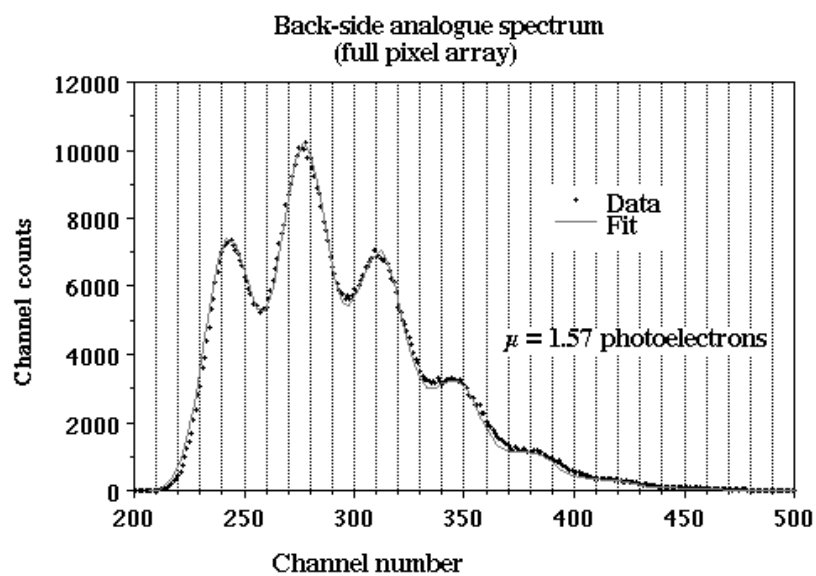
Figure 7.2: Backplane analog spectrum with a detector bias voltage of 55 V and a tube high voltage of 20 kV.
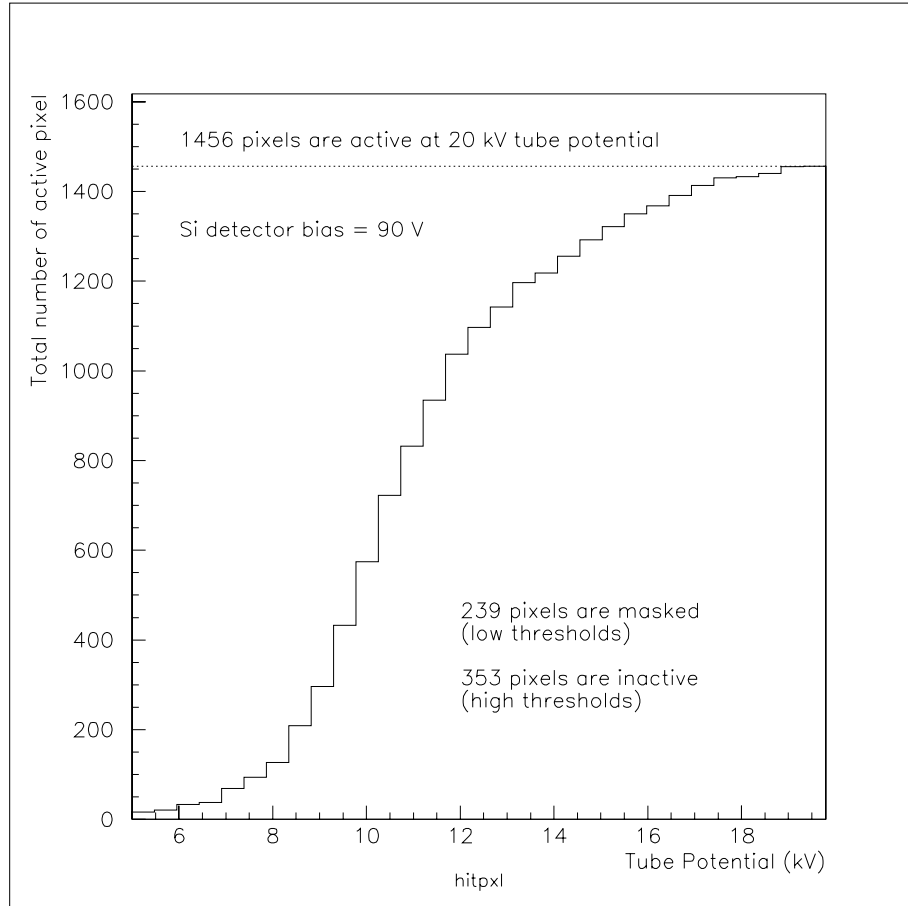
Figure 7.3: Number of active pixels as function of the high voltage.
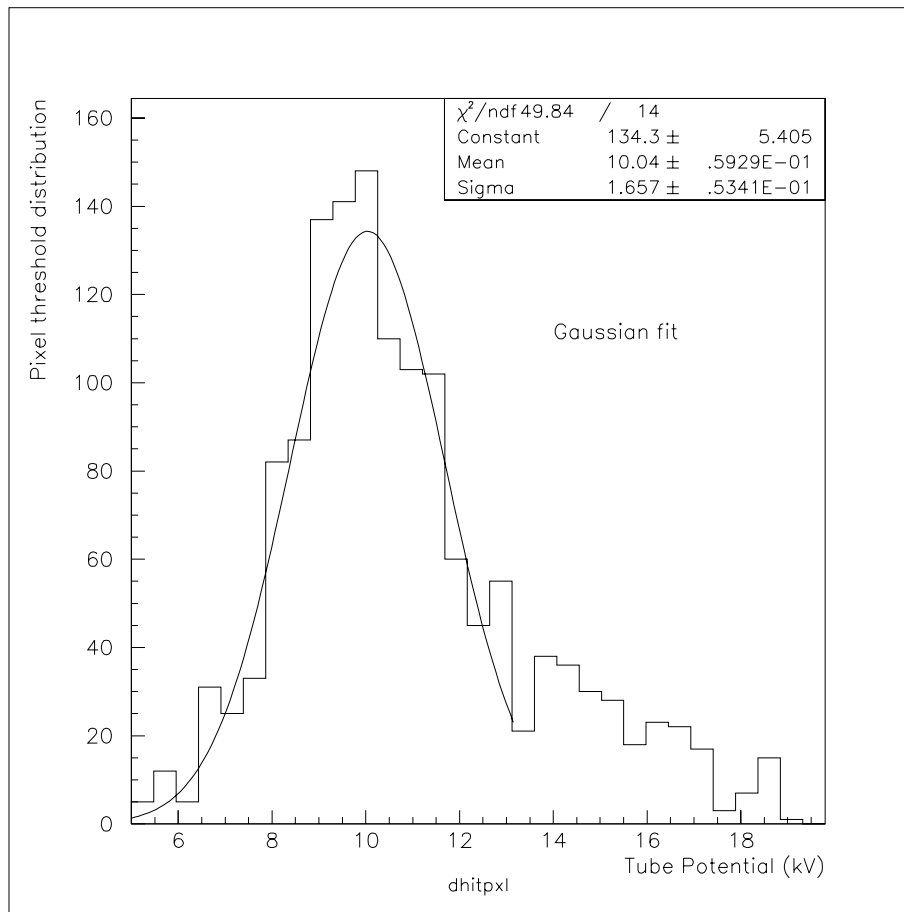
Figure 7.4: Threshold distribution: the number of pixel that become active for a given high voltage. The Gaussian fit gives an average threshold of 2800 e$^-$ with a sigma of 500 e$^-$

pixel, the probability that a fired active pixel gives a signal is

$$Eff. = 0.9/(1.57 \times 0.71) = 0.80$$

This inefficiency has two causes:

- Back scattering: a photoelectron hitting the diode can be back scattered without having deposited a sufficient amount of energy to create a detectable charge;

- Charge sharing: the electron cloud produced by the photoelectron inside the diode can be shared between two pixel, and the detected charge can be below threshold in both pixel.

The last effect is enhanced by the 50 μm pitch. It also appears, at a level of few percent, as two adjacent pixel responding to a single photoelectron. When the two pixel are adjacent along the 500 μm side the effect is called vertical double pixel cluster. Horizontal along the 50 μm side, and diagonal along the edge. The fraction of double pixel cluster, as function of the applied bias voltage, are shown on Fig. 7.6 for 20 kV high voltage. Horizontal and diagonal cluster are some per mill. The fraction of vertical cluster augment from V_{bias}=0 to V_{bias}=60 V, then decrease for higher voltage. Measurement of the back-plane spectrum at 60 and 90 V are identical, which shows that there is no increase in the amount of charge detected at higher bias voltage. The reason of such a behavior is the following. Detection efficiency increases with V_{bias} until the diode is pratically fully depleted at 60 V, then the number double cluster increases. The efficiency does not increase appreciably above V_{bias}=60 V, but the electrical field in the diode let the electrons drift faster, resulting in a better definition of the electronic cloud. Therefore the electron cloud has a lower probability to be shared between two pixels.

The charge sharing effect would be less important for square pixel 500×500 μm^2. The number of vertical adjacent boundaries would go down by a factor ten. In Ref. [4] a more detailed analysis is done and the electron transport in silicon has been simulated. The result are in good agrement with the data.

Conclusion

A half scale prototype of a Pixel HPD with cross-focussed electron optics and integrated pixel read-out has been developed in close collaboration with

Figure 7.5: Number of fired pixel per event.
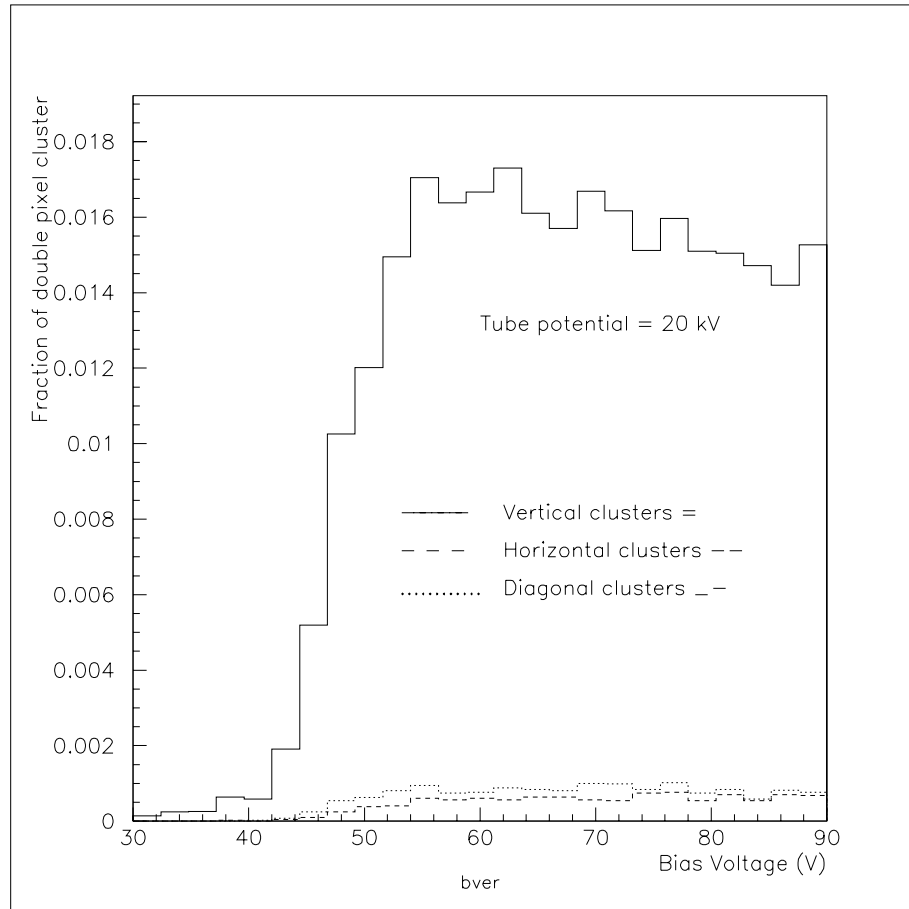
Figure 7.6: Number of double pixel cluster as function of the applied bias voltage.

industry. The efficiency of an active pixel, to detect a single photoelectron has been measured to be 80%. The inefficiency i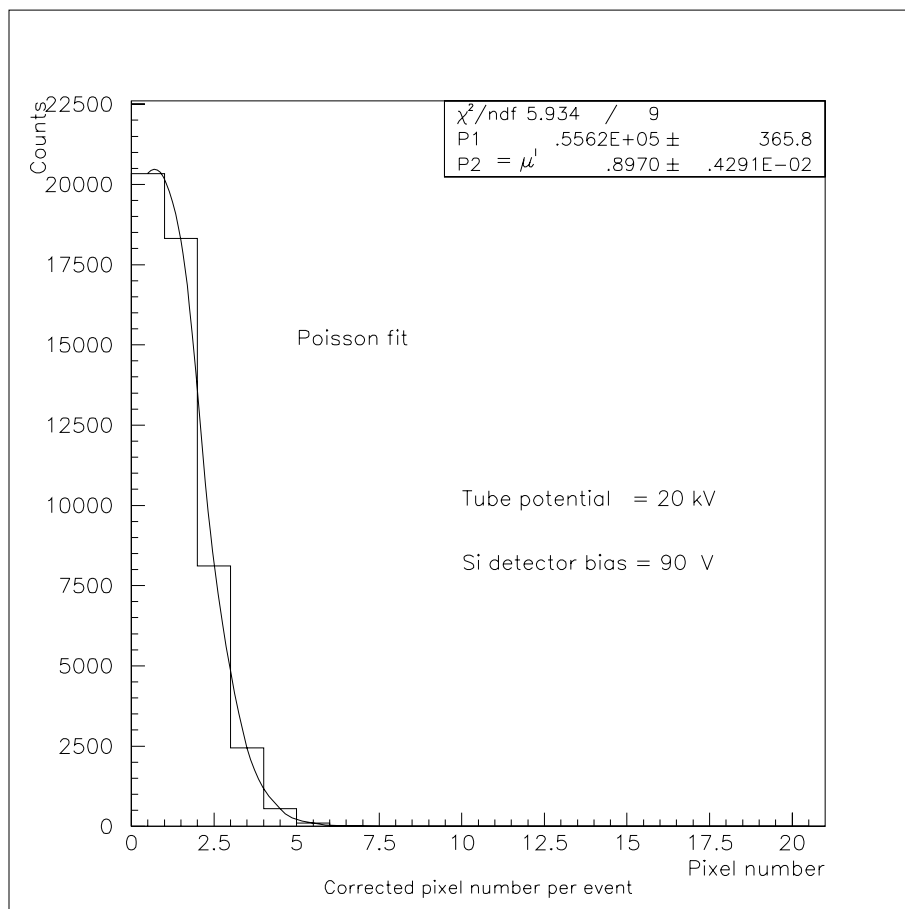s attributed to the combined effects of the discriminator threshold distribution, charge sharing at the pixel boundaries and photoelectrons backscattering at the silicon surface.

The 40:11 mm prototype has been manufacturated with existing parts and its ratio total-to-active area (50%) does not fulfill the LHCb requirements.

The pixel structure has a not necessary definition of $50{\times}500\ \mu m^2$, that contributes to an increased charge sharing.

For this reason a larger tube geometry as well as new pixel electronics are under development.

A new pixel chip is currently under development with a shaping time of 25 ns or less and a discriminator threshold $< 2000\ e^-$ with an RMS spread of $200\ e^-$ to uniformly identify the low signal generated by single photoelectron. A 3-bit adjustment of the discriminator threshold per pixel would reduce this spread to less than $40\ e^-$.

7.2　Full Scale Tubes

As concluded in the last section, the silicon detector for the final Pixel HPD is still under development. The electrostatic lay-out tube is ready and different samples have been produced.

The optical window is spherical, with an inner radius of curvature of 55 mm and is 7 mm thick. The outer diameter of the tube is 80 mm. All the photoelectrons emitted at $r < 72$ mm (r is the distance from the symmetry axis) are focused on the anode with $r < 18$ mm.

The design studies of the electron optics have been carried out exclusively by DEP. A cross check of the final design was made at CERN. Figure 7.7 shows a schematic lay-out of the tube. The electron optics is based on a tetrode structure with cross focusing. The trajectories of 9 photoelectrons emitted with a polar angle between $\pm 45°$ and with an initial energy of 1 eV, are in Fig. 7.8. The computation are done with the MAFIA[5] package. The electrons are emitted at $R = 36$ mm on the photocathode and they are perfectly focused on the anode surface. The focal surface is not flat as the photocathode has a spherical shape. Therefore the point spread function is not constant, but remains always below 100 μm. The demagnification factor varies from 4.2 at the edge to 4.5 near the axis.
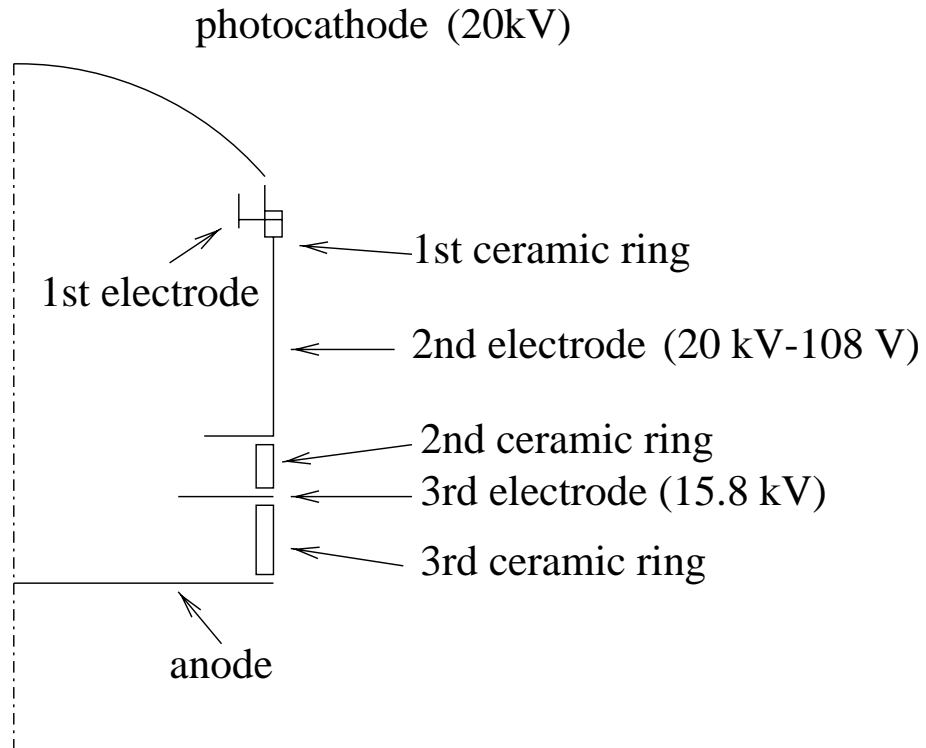
Figure 7.7: Scematic drawing of a 72:18 Pixel HPD prototype tube. The electron optics are based on a tetrode structure with cross focusing. The samples produced until now have been mounted on the anode a phosphor screen coupled to a CCD camera (one sample) or a 61-pixel silicon detector (three samples).
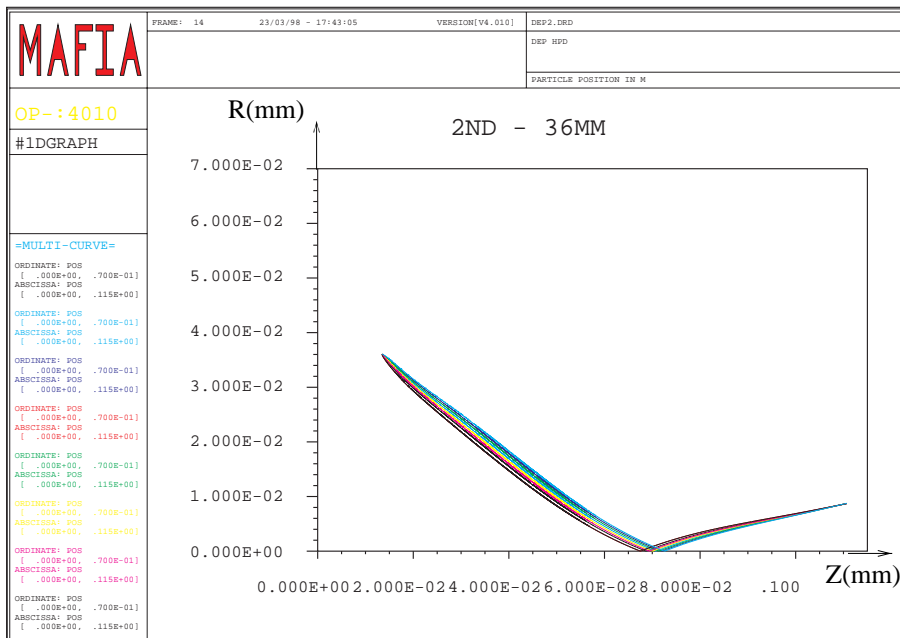
Figure 7.8: Trajectories of 9 photoelectrons emitted with a polar angle between $\pm 45°$ and initial energy of 1 eV, computed with MAFIA. The trajectories are computed in radial coordinates. The abscissa is the symmetry axis of the tube and the ordinate is r, i.e. the distance from the axis. Because r is always positive the trajectories are displied as reflected when they pass through the axis.

7.2.1 Phosphor screen tube

To test the photo-cathode homogeneity and the focussing properties, the first tube had a phosphor screen anode coupled to a CCD camera.

The photocathode window is made of fused silica. The phosphor screen is deposited on an optical fiber taper demignifing the output image by a factor of 3.2 at the CCD window. The final resolution is 49 μm in one direction (x) and 35 mm along the other (y). This corresponds to a precision on the photocathode of less than $\approx$ 200 μm.

A blue LED, was mounted on a XY translation table system for the optical characterization. The source was 90 mm from the quartz window of the tube. A cylindrical collimator, 20 mm long, 0.2 mm in diameter, limited the source divergence to $\approx$5 mrad, resulting in a light spot $\approx$1 mm in diameter and a RMS of 1 mm/$\sqrt{12}$ =290 μm on the window axis. The source was moved horizontally and vertically in a matrix of 176 points with 5 mm pitch. The maximum distance from the axis of the spots is 36.4 mm. In Fig. 7.9 the position of the light spots is shown together with the computed emission points of the photoelectron on the photocathode. The last are computed taking in account the refraction of the light in the quartz. Average and RMS of the distribution of the position of the produced photoelectrons for every run is computed. Figure 7.10 shows the average detection point for all the runs together with the emission points. A small pincushion distortion is due to the non perfect linearity of the demagnification function.

The demagnification function used has 5 free parameter: x and y shift, the linear demagnification along x and y and the quadratic factor to parameterize the pincushion distortion. The first two parameters would indicate a misplacement of the anode. They are both less then 20 μm and therefore negligible. The linear demagnification factor is the same in both x and y direction. The transformation function can be written as:

$$r_{cathode} = 4.6 \times r_{anode} \Leftrightarrow 6.3 \; 10^{-2} \times r_{anode}^2 \qquad (7.1)$$

Therefore the pincushion distortion is very small and in good agreement with the simulation. It is always possible to reconstruct the photoelectron emission point with a good precision, as shown in Fig. 7.11.

Figure 7.12 shows the RMS of the point spread function of the photoelectrons on the anode. It varies from 50 to 65 μm, then the uncertainty on the emission point on the photocathode is less than 65$\times$4.6=300 μm. Knowing

that the light spot has an RMS of ≈290 μm the absolute uncertainty on the emission point results to be $\sqrt{300^2 \Leftrightarrow 290^2} \approx 80$ μm.

Figure 7.13 shows the number of detected photoelectrons with respect to the distance of the light source from the tube axis. Because of reflection on the interface air-quartz and on the interface quartz-photocathode there is a loss of efficiency of 13%. This has to be taken in account for quantum efficiency consideration as the value provided by DEP for every tube are referring to a central zone of 25 mm in diameter.
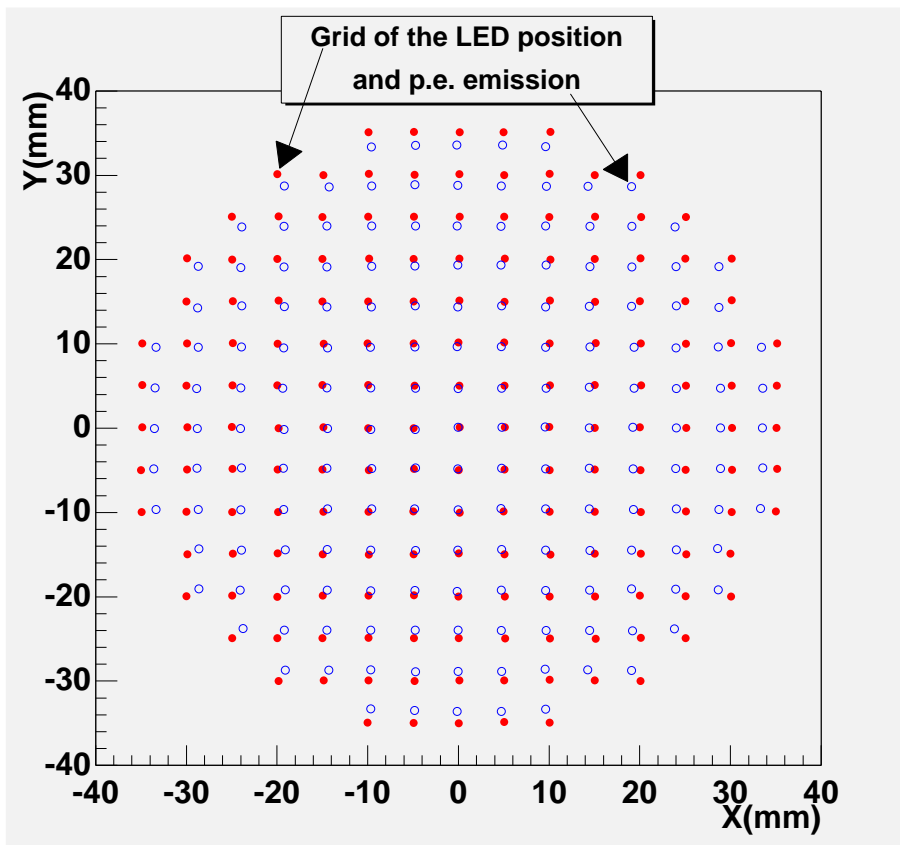
Figure 7.9: Phosphor-anode tube: position of the light spots on the optical and photoelectrons emission point (in mm).
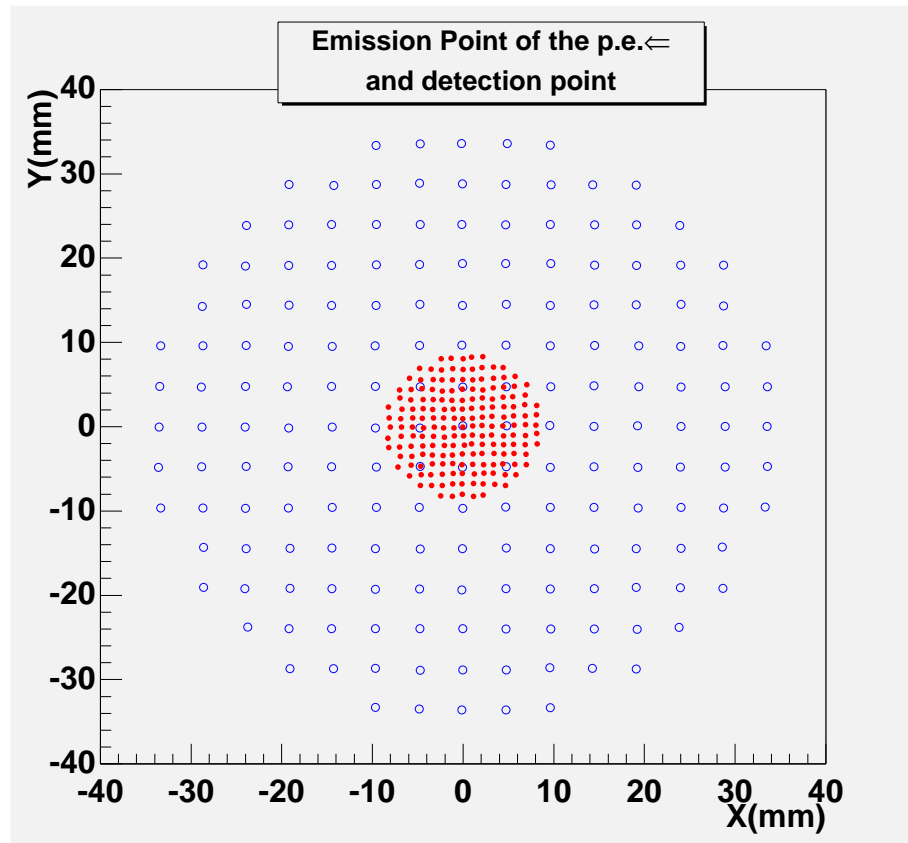
Figure 7.10: Phosphor-anode tube: photoelectrons emission point and detection point (in mm).
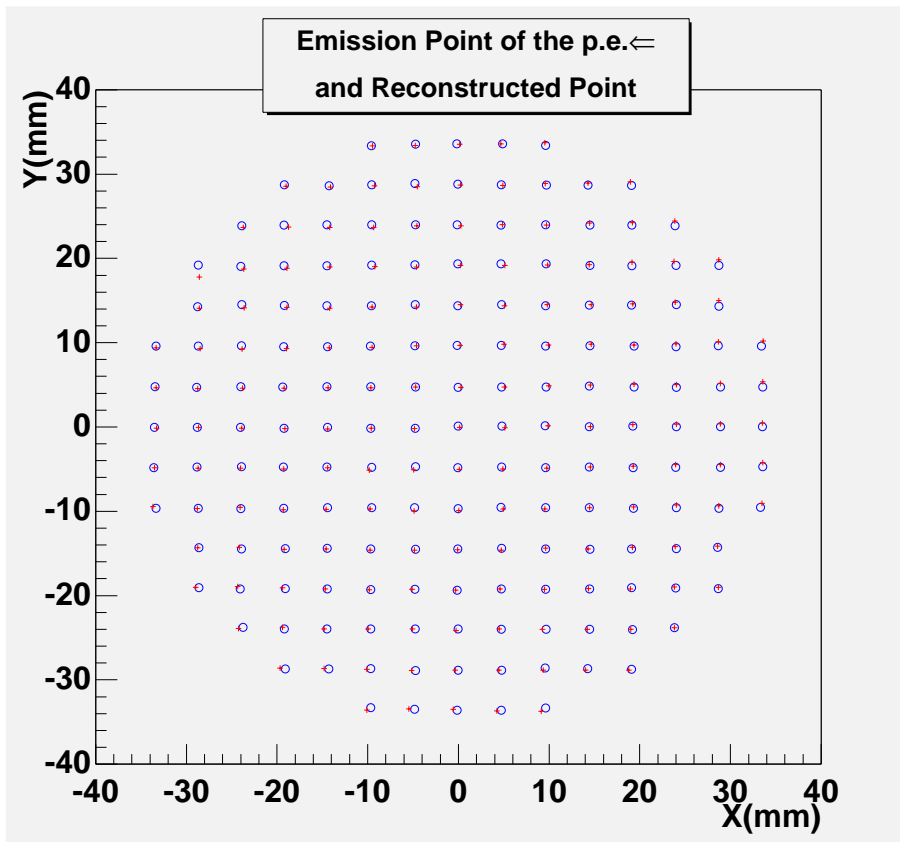
Figure 7.11: Phosphor-anode tube: photoelectrons emission point and reconstructed emission points from the detection coordinates. With one exception (due probably to a misplacement of the LED) the reconstructed emission points are always less than 0.5 mm distant from the emission point (in mm).
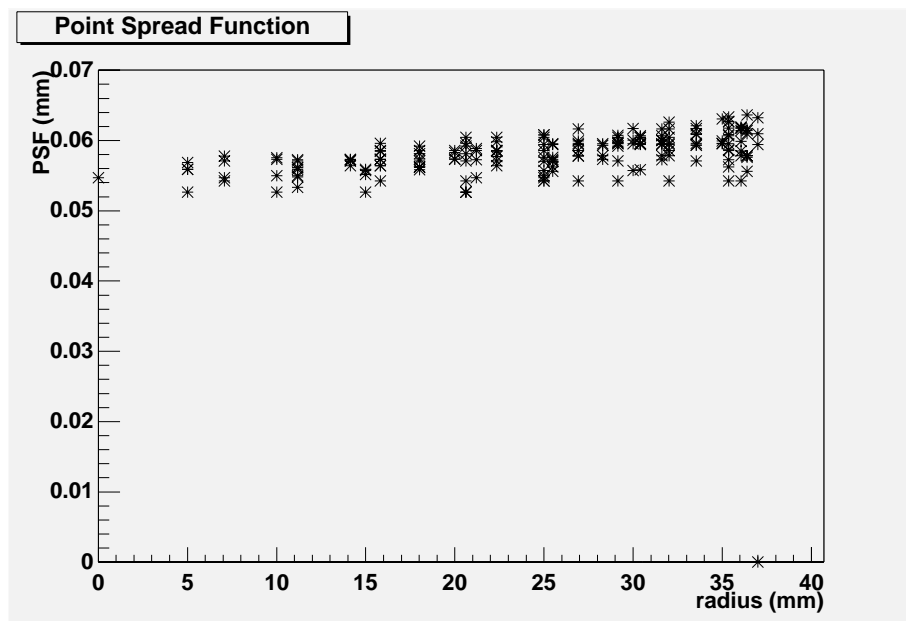
Figure 7.12: RMS of the point spread function of the photoelectrons on the phosphor-anode vs. the distance of the light source from the tube axis.
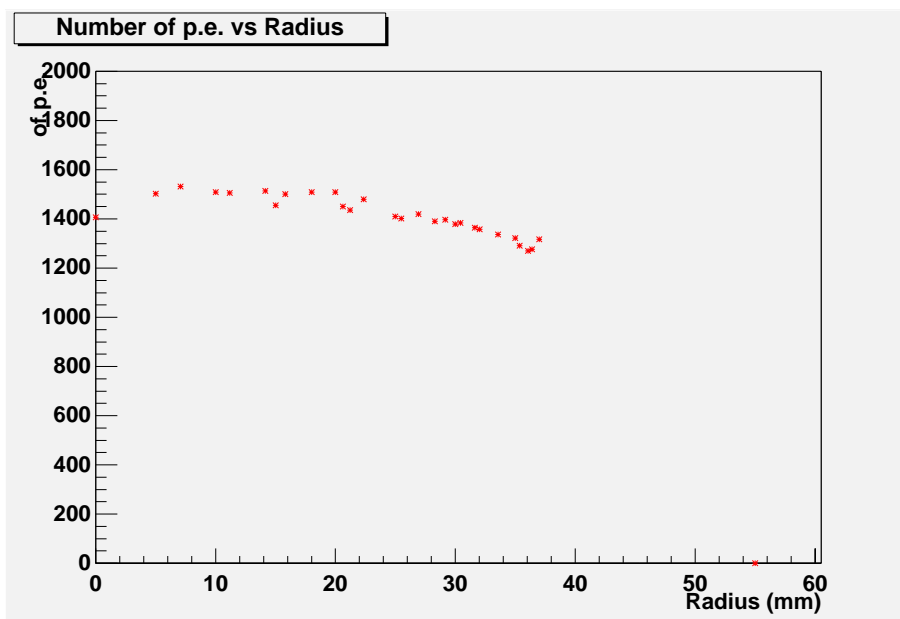
Figure 7.13: Number of detected photoelectrons vs. the distance of the light source from the tube axis.

7.2.2   61-pixel HPD prototypes

Three full scale tubes have been manufactured and equipped with 61-pixel detectors. They are read externally with the VA2 chip (1.2 μs peaking time). The quantum efficiency is shown in Fig. 7.16. It reaches a maximum of 26% for $\lambda = 270$ nm. The pixel are hexagonal with dimension 2 mm flat to flat. The optical properties of these devices have been measured with the same system as for the phosphor-anode HPD, but the light source was moved only along one direction. The density of measurement points was increased around the pixel boundaries. The results are shown in Fig. 7.14. The experimental values are fit to a stair-case function to model the data. The light spot image on the pixel array is the result of the convolution between the tube point spread function and the LED finite spot size, the latter scaled by the demagnification factor. This image is modeled as a 2-dimensional Gaussian centered at r_{anode} and and with standard deviation assumed to be constant over the silicon detector. Informations about the electron optics are coming when the light spot is near the pixel boundaries. Here it is integrated over two pixel, and precise information of its center-of-gravity position can be obtained. The result of 61-Pixel HPD the demagnification function is:

$$r_{window} = (5.08 \pm .03) \cdot r_{anode} \Leftrightarrow (0.0077 \pm .007) \cdot r_{anode}^2 \qquad (7.2)$$

the quadratic factor is smaller than in the previous relation because r_{window} gives the coordinate of the light source on the window and not the photo-electron emission point. The pincushion distortion is then attenuated by the window lens effect.

HPD cluster test in the LHCb RICH1 prototype

In June 1999 beam test were performed at CERN in the T1-X7b facility which provides 120 GeV/c negative pions. The Cherenkov counter used in the test beam was a full scale prototype of the LHCb RICH1 detector (see Fig.7.15). The beam particles enter the prototype box along a tube of 90 mm internal diameter and the beam axis intersects the mirror center at an angle of 18° to the mirror axis. The detector plane is fixed at a distance of 1143 mm from the mirror center. The radius of curvature of the mirror is 1117 mm and reflectivity curve is shown in Fig. 7.16. The radiator is a C_4F_{10} contained within a cylinder of length $L = 1000$ mm. This volume is sealed with a 25 mm thick quartz plate (its transmission is shown in Fig. 7.16). The mean wave length of detected photon, for a uniform spectra in energy, is 293 nm.
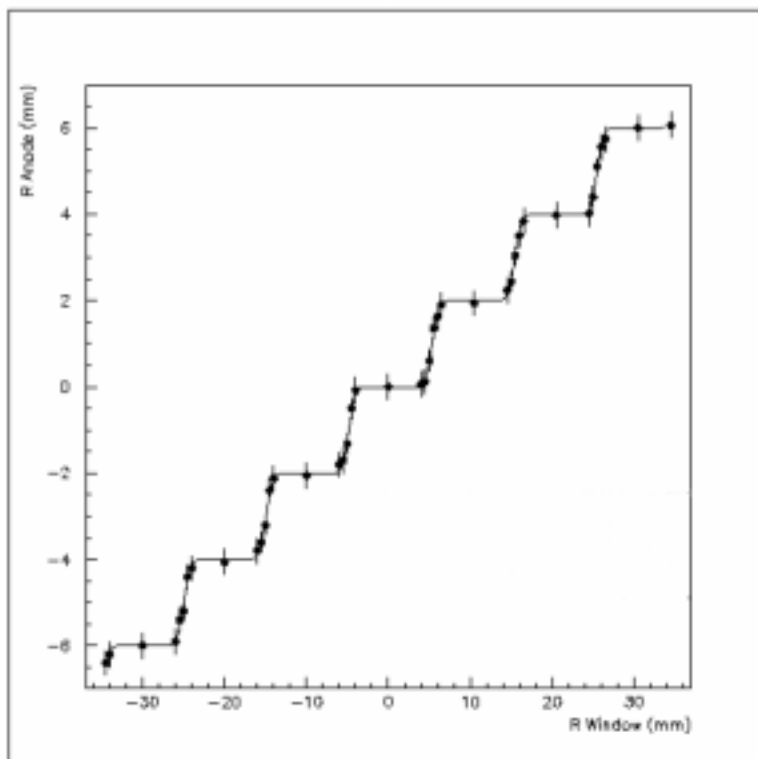
Figure 7.14: Measured demagnification function of the HPD electron optics resulting from a scan of a LED spot over the photocathode active diameter. The staircase function fit gives $r_{win} = (5.08 \pm .03) \times r_{anode} \Leftrightarrow (0.0077 \pm .007) \times r_{anode}^2$.. The uncertainty on the quadratic parameter is as big as the parameter itself.

All three tubes were operated at nominal high voltage (20 kV) and silicon detector bias (60 V). The cluster consisted of the tubes close packed with a 2 mm gap between them. No tracker was present for determining the pions trajectory.

All the data where stored on an Objectivity/DB system (see App. B. Three kinds of run has been analyzed:

a) Air radiator at 968 mbar (Average n=1.000275). In this case the ring is focused on a single HPD and three runs (Nbr. 13, 15, 17) has been analyzed, one for every tube.

b) C_4F_{10} radiator at 164 mbar (Average n=1.000225). Three runs (Nbr. 40, 42, 44), same situation as case *a*.

b) C_4F_{10} radiator at 1100 mbar (Average n=1.0015). The ring cover all the three tubes. Two similar runs (22, 93) has been analyzed.

One event display for each type of run is shown in Fig. 7.17, 7.18 and 7.19.

In Fig. 7.20 is shown the ADC spectra of a pixel on the Cherenkov ring. Signal up to 6 photoelectron are resolved. Every photoelectron peak has been fitted with a Gaussian. Signal-to-noise ratio is ≥ 10. For every event a 4-sigma cut has been done above pedestal, then a weight n was given depending if the signal was laying in the n-photoelectron signal region.

As explained in Chap. 4 the images are not perfect circles if the focusing mirror is tilted. The reconstruction was carried out fitting event per event the Cherenkov photon hits with a circle using the Linear Regression Method explained in App. A. The radius distribution for a C_4F_{10} atmospheric-pressure run (number 22) is shown in Fig. 7.21. For comparison the radius distribution has been computed minimizing the χ^2 with a NAG ([2]) function. No significant difference has been observed (see Fig. 7.22).

The detecting element size is ≈ 10 mm on the entrance window. The difference between x and y axis of the ellipse-like images is 2 mm for air and low-pressure C_4F_{10} and 5 mm for atmospheric-pressure C_4F_{10} . In the first two cases it is impossible to resolve the eccentricity of the image. In the last case the same method as discussed in Sec. 4.3.4 was used. The distance of the photon hits to the fitted circle versus the azimuthal angle ϕ was plotted. It does not show any correlation between the two variables. This is due to

---

[2]NAG: The numerical Algorithm Group provides standard mathematical C library at CERN

Cherenkov Ring at Focal Plane

Light tight Box

Focal Plane

Pivot point

Interface Board

Quartz Plate and Vacuum seal

Board B

C4F10

3 x 80mm Pixel HPDs

Sketch of prototype layout for cluster test of Pixel HPDs

1117 mm Focal length Mirror
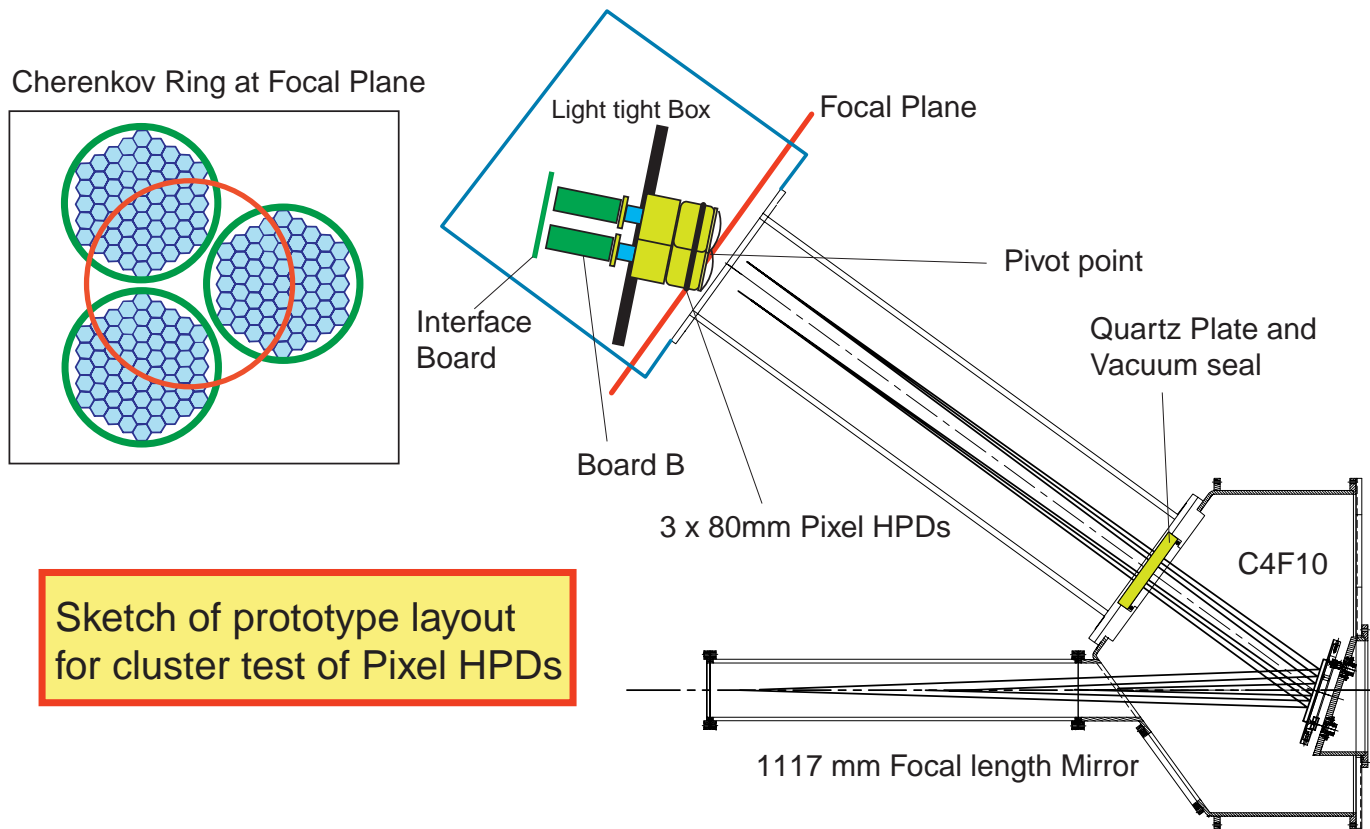
Cherenkov angle is 53 mrad with C4F10 radiator at 1000mbar

Figure 7.15: Full scale prototype of the LHCb RICH1 detector used for the Pixel HPD cluster test.
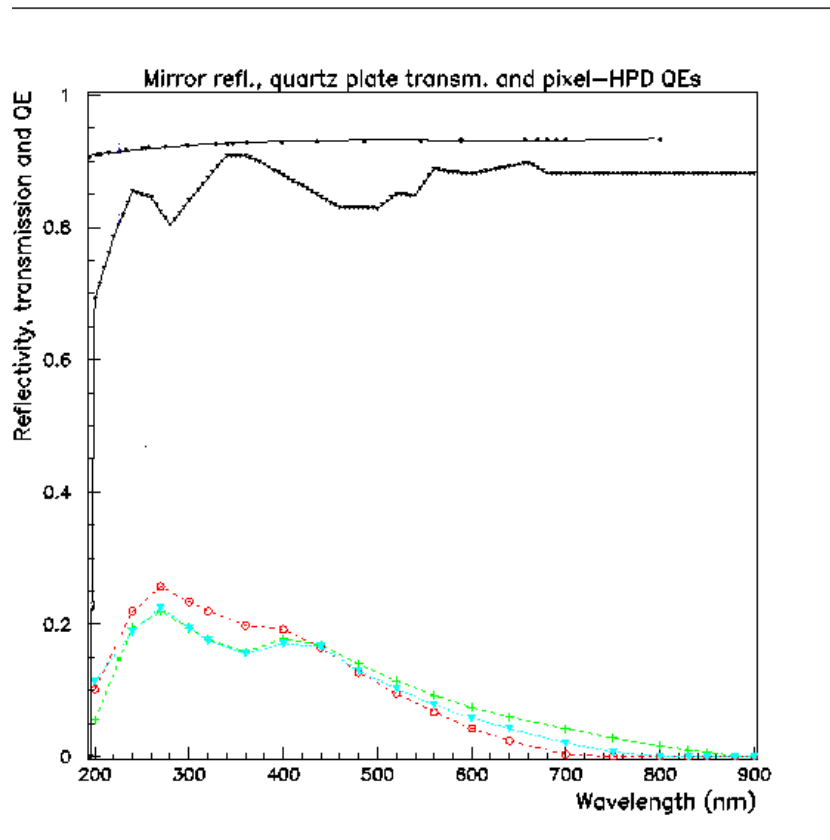
Figure 7.16: Quantum efficiency of the three 61-Pixel HPD (lower curves). The mirror reflectivity (middle curve) and the quartz plate transmission (highest curve) of the RICH1 prototype used in the beam test are also shown.
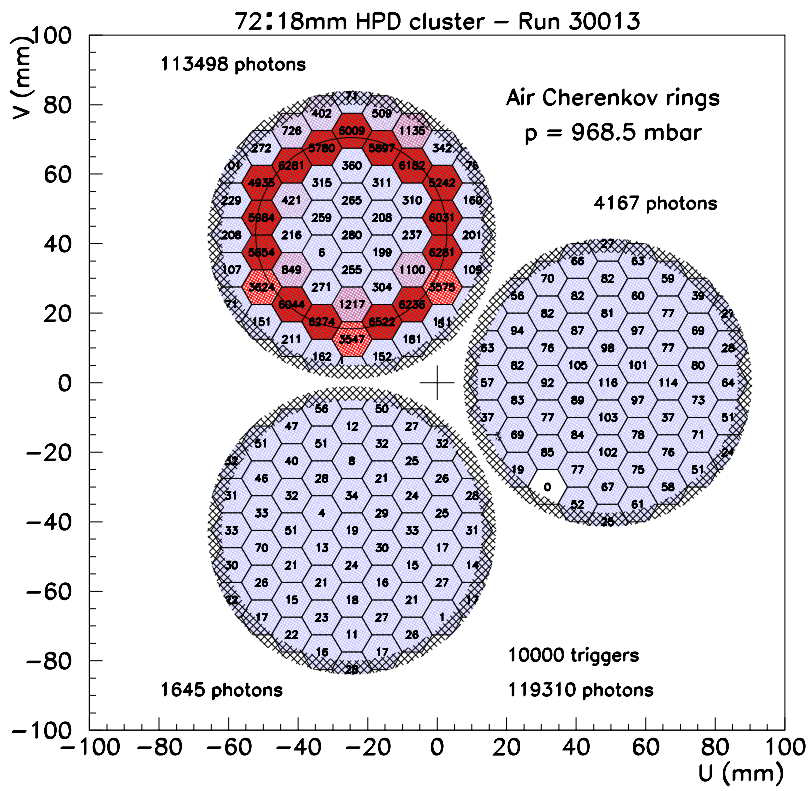
Figure 7.17: Event display of one Air radiator at 968 mbar run.
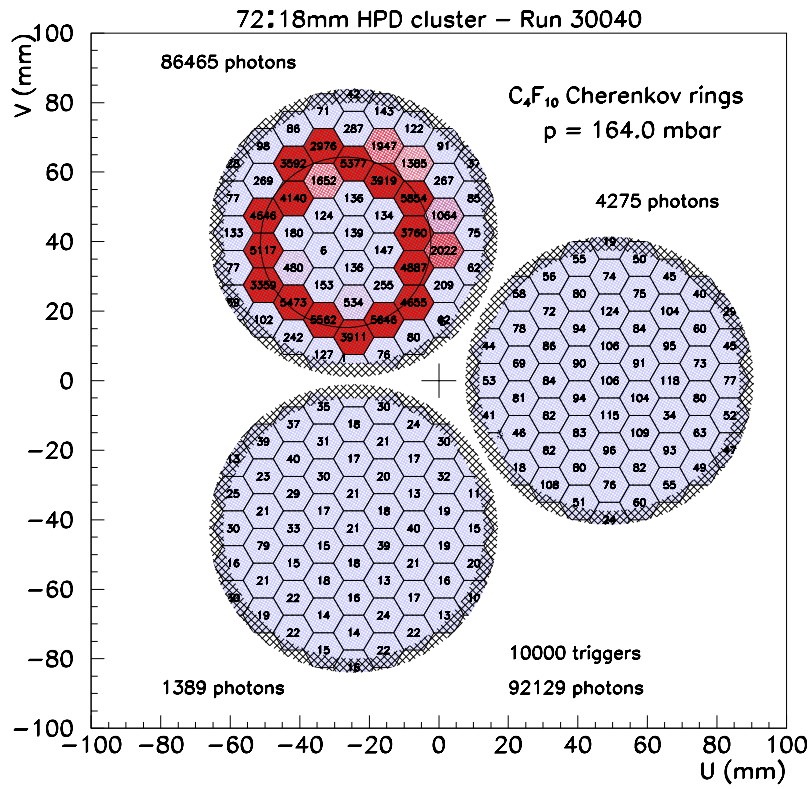
Figure 7.18: Event display of one C_4F_{10} radiator at 164 mbar run.
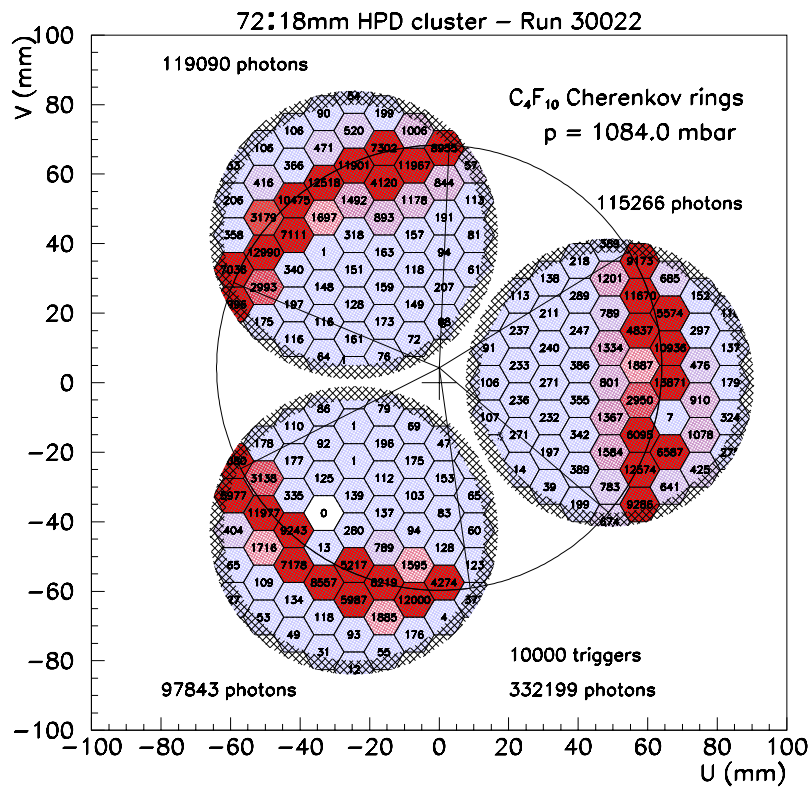
Figure 7.19: Event display of one C_4F_{10} radiator at 1100 mbar run.
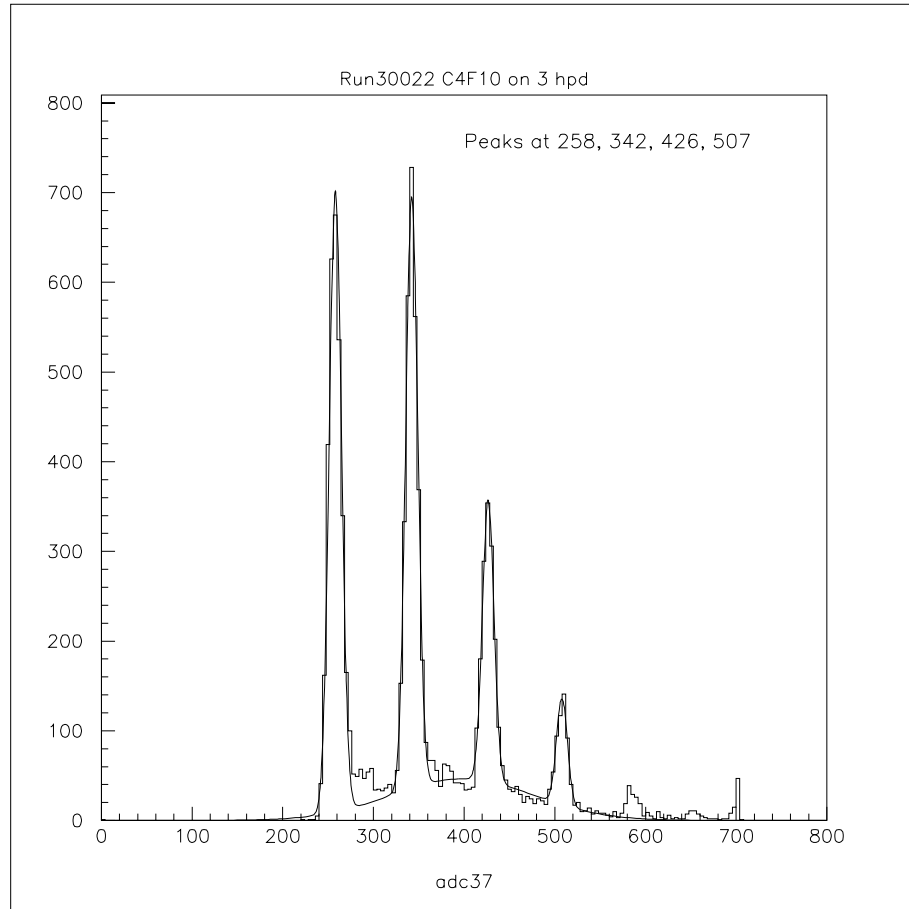
Figure 7.20: ADC spectrum for a pixel laying on the Cherenkov ring. Every peak is fitted with a simple Gaussians to get the signal-to-noise ratio ($\approx$10).

the fact that, as one can see from the event display, the angular coverage in ϕ for this configuration is 59%. Another attempt has been tried. The integrated hit distribution (see Fig. 7.23) has been fitted with an ellipse with Gaussian spread plus background (see Fig. 7.24):

$$Z = A + B \cdot e^{-\frac{(X-X_c)^2 + \alpha^2(Y-Y_c)^2 - R^2}{2\sigma^2}}.$$

The term α turns out to be 1.007. This means that the ellipse is seen as a circle. Therefore the informations coming from the event per event fit are used. The Cherenkov angle θ_C^{meas} is obtained dividing the radius of the circle by the distance mirror-HPD's. The index of refraction n of both air and C_4F_{10} at a given pressure is known[6], therefore the expected Cherenkov angle is computed from the relation $\cos(\theta_C^{exp}) = 1/n\beta$, with $\beta = 1$. In Tab. 7.1 to 7.4 the two angles, for all the runs, are tabled.

The final number of photoelectrons μ is measured using the relation

$$\frac{Signals\ below\ threshold}{Total\ number\ of\ signal} = 1 \Leftrightarrow e^{-\mu}$$

coming from Poisson statistic. The number of photoelectrons seen in empty target run is subtracted. This gives the measured number of photoelectrons N_{meas}. In Tab. 7.1 to 7.4 N_{meas} is compared to the expected number of photoelectrons computed with the formula (Eq. 3.8):

$$N_{exp} = \left(\frac{\alpha}{\hbar c}\right) L \, \epsilon_A \int QE \times \mathcal{R} \times \sin^2 \theta_C^{exp} \, dE_\gamma$$

For the expected number of photoelectrons the reflection on the photocathode quartz window is not taken in account. This could explain that the measured number of photoelectron about 10% lower than the expected one.

Conclusion

Within the framework of the research and development work for the RICH detector of LHCb, full scale prototypes have been manufactured and tested. Tubes equipped with phosphor anode have shown a precision of the photon hit on photocathode window of 80 μm and an active-to-total area ratio 82%. Three samples have been equipped with 61-pixel silicon detector anodes and external read-out. A cluster has been installed in a LHCb RICH1 prototype with C_4F_{10} radiator and used in a test beam. On this particular configuration (59% of geometrical coverage) the mean number of photoelectrons was 35.

HPD	N_{exp}	N_{meas}	θ_C^{exp} (mrad)	θ_C^{meas} (mrad)
1	12.2	11.1	23.4	24.1 $\pm$.3
2	11.0	9.4	23.4	24.0 $\pm$.3
3	10.8	11.0	23.4	24.0 $\pm$.3

Table 7.1: Air (968.5 mbar)

HPD	N_{exp}	N_{meas}	θ_C^{exp} (mrad)	θ_C^{meas} (mrad)
1	10.0	8.5	21.24	21.4 $\pm$.25
2	9.0	7.4	21.24	21.4 $\pm$.25
3	8.9	8.4	21.20	20.6 $\pm$.25

Table 7.2: C_4F_{10} (164.0 mbar)

HPD	N_{exp}	N_{meas}	Cov.	θ_C^{exp} (mrad)	θ_C^{meas} (mrad)
1	12.8	11.7	70°	54.6	56.0 $\pm$.3
2	11.8	10.1	71°	54.6	idem
3	11.8	11.8	72°	54.5	idem

Table 7.3: C_4F_{10} (1084.0 mbar)

HPD	N_{exp}	N_{meas}	Cov.	θ_C^{exp} (mrad)	θ_C^{meas}. (mrad)
1	13.2	12.5	70°	55.4	56.1 $\pm$.3
2	11.9	11.1	70°	55.4	idem
3	12.1	11.5	72°	55.3	idem

Table 7.4: C_4F_{10} (1114.5 mbar)
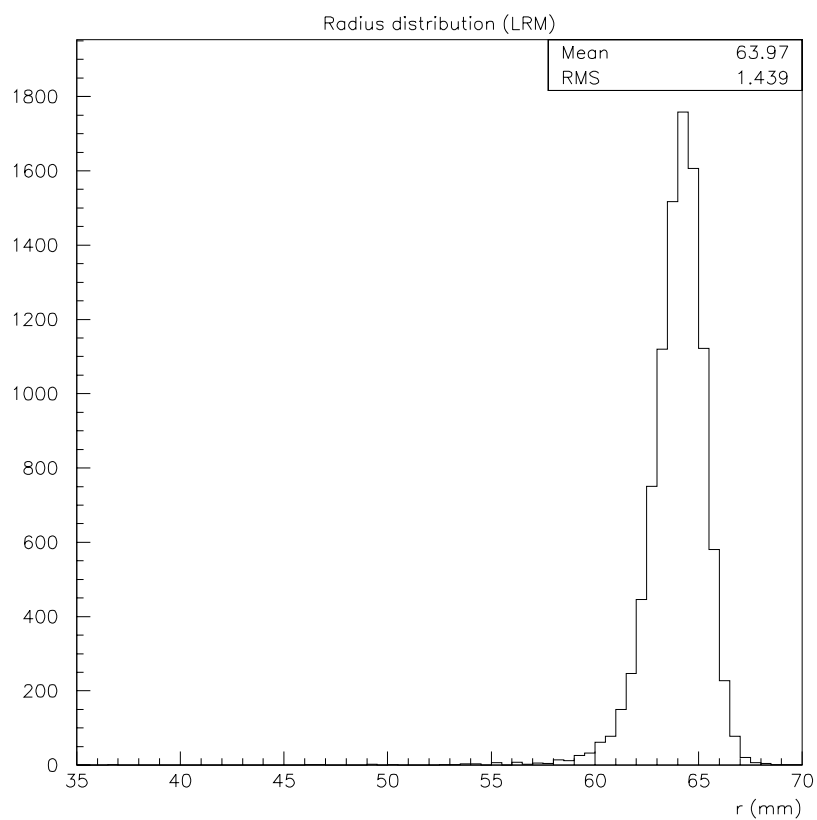
Figure 7.21: Radius fitted event per event with the Linear Regression Method for a C_4F_{10} atmospheric-pressure run.
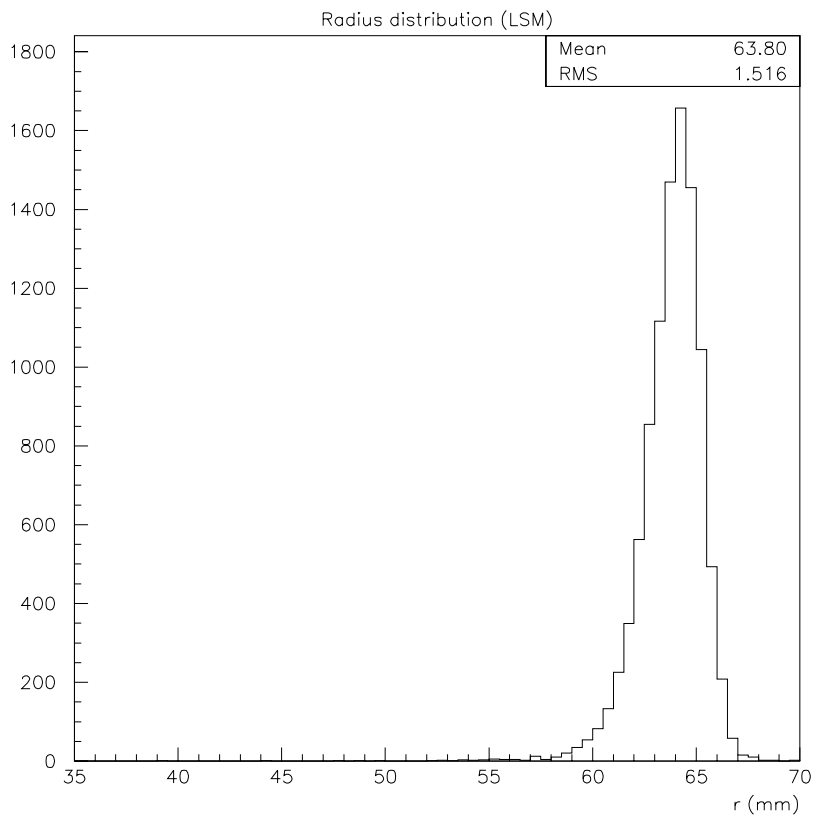
Figure 7.22: Radius fitted event per event with the Least Square Method for a C_4F_{10} atmospheric-pressure run.
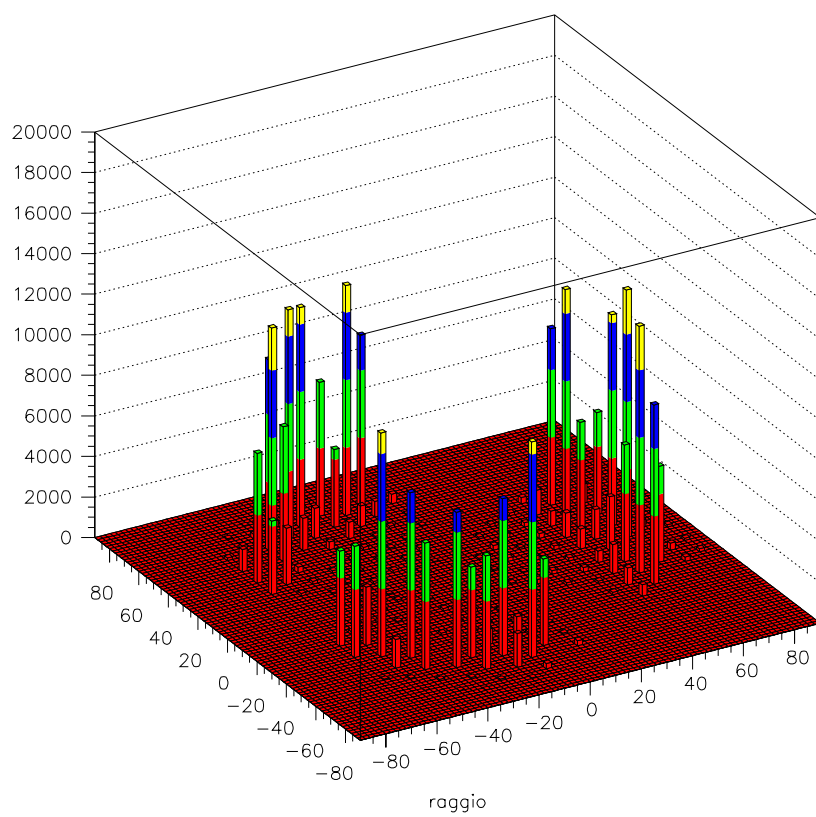
Figure 7.23: Integrated hit map for a C_4F_{10} atmospheric-pressure run.
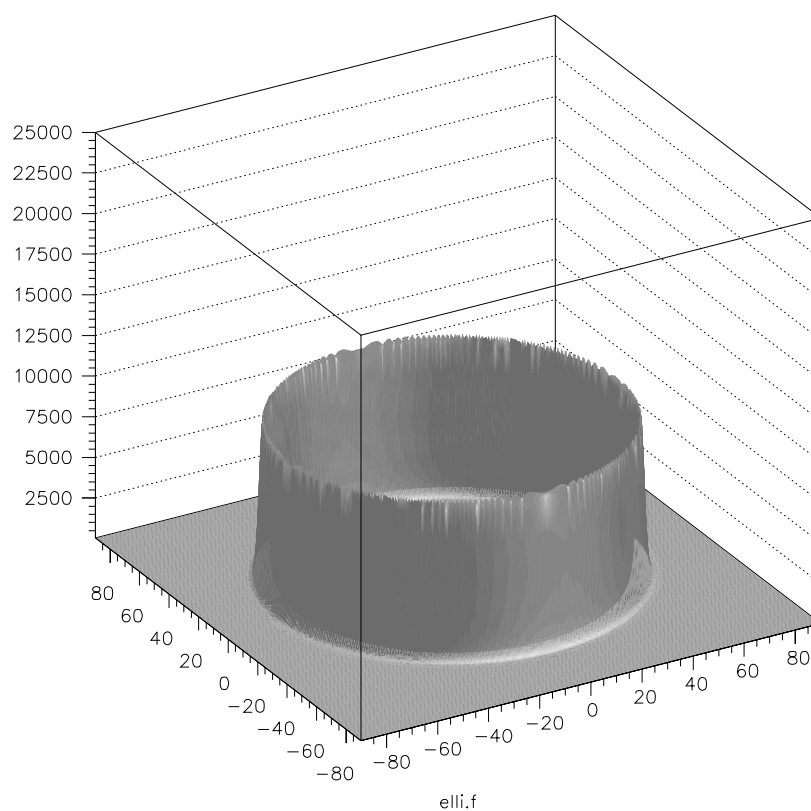
Figure 7.24: Ellipse with Gaussian spread plus background used to fit the integrated hit map for a C_4F_{10} atmospheric-pressure. Due to the detection element size (10 mm) and the low angular coverage (58%) it is impossible to resolve the ellipse and the result is a circle

Bibliography

[1] Delft Electronics Products (DEP) B.V., P.O. Box 60, Dwazziewegen 2, NL-9300 AAB Roden, The Netherlands.

[2] E. Heijne *et al.*, Nucl. Instr. and Meth. A 383 (1996) 55.

[3] M. Alemi *et al.*, Performance of a hybrid photon detector with electrostatic cross-focusing and integrated silicon pixel read-out for Cherenkov detection, proceeding of the 6th International Conference on Advanced Technology and Particle Physics, October 5-9, 1998, Como, Italy, to be published in *Proc. Suppl. Nucl. Phys. B*.

[4] M. Alemi *et al.*, First operation of a hybrid photon detection prototype with electrostatic cross-focusing and integrated silicon pixel read-out, CERN-EP/99-110, 12 July 1999. Submitted to Nuclear Instruments and Method A

[5] MAFIA is a product of the CST GmbH, Lauteschaegerstr. 38, D-64289 Darmstadt. WWW: *http://www.cst.de*.

[6] R. Abjean *et al.*, Nucl. Instr. and Meth. A292 (1990) 593.

Appendix A

Analytical circles fit

In many data handling problems there is a need to fit data points to a circle (e.g. the trajectory of a charged particle moving in a uniform magnetic field). In other cases a circle is used as an approximating curve that possesses some advantage when compared with other curves for its simplicity in fitting, as is the case of the fit procedures used in Chapt. 4 and 7.

A.1 Analytical solution of the problem

The problem one has to deal with is that: for N given points (x_i, y_i) on a plane, we must find the circle:

$$(x - a)^2 + (y - b)^2 = R^2 \tag{A.1}$$

that minimizes the mean square distance from the given points, i.e., if the uncertainties σ_i on every point are the same, we must find the minimum of the functional

$$L(a, b, R) = \sum_{i=1}^{N} \rho_i^2, \tag{A.2}$$

where

$$\rho_i = \sqrt{(x_i - a)^2 + (y_i - a)^2} - R \tag{A.3}$$

This is the Least Square Method fitting (LSM from here on). The LSM is very attractive if the theoretical model implies a *linear* dependence on the

parameters and if the uncertainties are independent from them. In this case it provides an *exact* and *unique* solution.

In our case, due to the nonlinear dependence of ρ_i on the circle parameters the application of the LSM leads to analytically unsolvable equations. That is why the LSM is usually carried over as an iterative procedure, applying linearization at each step and demanding an accurate choice of the starting values.

Under certain conditions, explained later, another method called the Linear Regression Method (LRM) ([1] and [3]) can be used.

The LRM is based on introducing the new variable $z = x^2 + y^2$ in the circle equation A.1, to transform it to the linear regression equation:

$$z = \alpha x + \beta y + \gamma,$$

where $\alpha = 2a$, $\beta = 2b$, $\gamma = R^2 - a^2 - b^2$ are treated as the new unknown parameters. Evaluating them by the LSM the parameters a, b, R are determined.

It is clear that using the LSM for the last equation corresponds to minimizing the functional

$$M(a, b, R) = \sum_{i=1}^{N} \left((x_i - a)^2 + (y_i - a)^2 - R^2 \right)^2. \tag{A.4}$$

Differentiating this equation with respect to a, b and R, and equalizing to zero, one obtains:

$$a = \frac{([x, x^2] + [x, y^2])[y, y] - ([y, x^2] + [y, y^2])[x, y]}{2([x, x] \cdot [y, y] - [x, y]^2)},$$

$$b = \frac{([y, x^2] + [y, y^2])[x, x] - ([x, x^2] + [x, y^2])[x, y]}{2([x, x] \cdot [y, y] - [x, y]^2)},$$

$$R^2 = [x^2] + [y^2] - 2a[x] - 2b[y] + a^2 + b^2, \tag{A.5}$$

with the notation

$$[x^p y^q] = \sum_{i=1}^{N} x^p y^q.$$

Eq. A.4 is, according to Eq. A.3

$$M(a, b, R) = \sum_{i=1}^{N} \left((R + \rho_i)^2 \Leftrightarrow R^2 \right)^2 =$$

$$4R^2 \sum_{i=1}^{N} \rho_i^2 (1 + \rho_i/2R)^2 \tag{A.6}$$

From this equation one sees that LSM and LRM coincide if $\rho_i/2R << 1$. Therefore the above mentioned condition to be satisfied for using LRM is that it can be used only for $\rho_i << R$, because of a high sensitivity to errors in measurements.

An iterative method can be used to improve the accuracy of LRM in case some points have $\rho_i \approx R$. For Cherenkov imaging this cleaning procedure of the photon sample relies on the fact that photons, actually emitted by the charged particle, have error distribution which can be well approximated by Gaussian. In this case a suitable criterium in removing fake signal (as Rayleigh scattered photons or electronic noise) is to eliminates all hits giving a contribution to M greater than some maximum value.

The LRM provides a fast, simple and elegant way for fitting focalized Cherenkov rings to a circle. Under the condition that fake signals are not too far away from the predicted circle it gives the same value that the LSM would give.

The LRM has been used for the data of the prototypes described in Chapt. 4 and Chapt. 7. In these cases the geometrical acceptance of the detectors put an intrinsic cut on the detected photons, therefore no significant difference can be observed with an iterative method.

In Chapt. 7 a fit obtained with Eq. A.5 have been compared with the result obtained minimizing the functional of Eq. A.2 with a NAG [1] function and no significative difference has been observed.

---

[1]NAG: The numerical Algorithm Group provides standard mathematical C library at CERN

Bibliography

[1] N.N. Govorum *et al.*, JINR-2036, Dubna (1965) (in Russian, quoted in [2])

[2] N. Chernov et G. Osokov, Computed Physics Communications **33** (1984) 329

[3] J. Crawford, Nucl. Instr. Meth. **A 211** (1983) 223.

Appendix B

BOSS: a Test Beam Object Storage System

The relational model for the storage of data used in the 80's is now obsolete. The complexity of the structure of the event for the LHC era, and more important the amount of data that will be taken (PBytes/year) are considerably increased. Data must be accessible by different machine architectures and operative systems. The mean life of LHC experiments will be about 20 years, then the software must be modifiable as easyly as possible for new needs or for hardware upgrading. About 200 collaborations, distributed world wide in the more developed countries, must access the data.

The solution proposed by RD45 (a CERN R&D project established in 1995 to investigate the question of object persistency for high energy physics) is an object database management system (ODBMS) with a Mass Storage System.

The philosophy adopted by RD45 is that whenever a commercial solution exists, it must be preferred to a non commercial one. Objectivity/DB, produced by the homonym society, has been chosen, because it seems to meet the main requirements.

In order to test the possibility to store test beam data on a database the data of the beam test described in Chap. 7 were stored using the Objectivity/DB.

Objectivity is one of the two libraries used at CERN for object persistency. The other option, ROOT [1], developed at CERN, has been successfully used by other groups (e.g. the LHCb Outer Tracker Testbeam Software [2]).
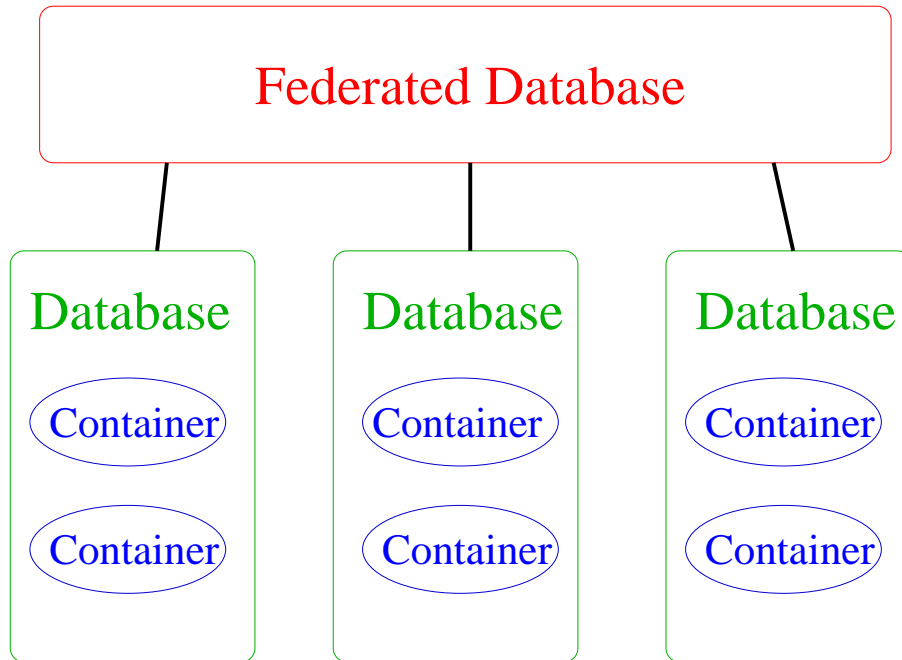
Figure B.1: Logical storage hierarchy of an Objectivity ODBMS

An Objectivity/DB system consists of multiple processes and files that can be distributed across multiple host machines on a network. The logical storage hierarchy is shown in Fig. B.1. A federated database is a file where all the informations about the different databases are stored. Different databases can be on every machine connected to Internet. Every database has different containers where different kind of information are stored.

In our case one database was created for storing the data of one run. Two containers, the `EventContainer` and the `DataBlockContainer`, are created in every database.

Objects of type `DataBlock` have the following persistent data member:

- `NbrOfChannel`

- `ChannelId[NbrOfChannel]`

- `AdcCharge[NbrOfChannel]`

- `ooRef(Event) event <-> hpdBlock[];`

and methods:

- `PixelId(NbrOfChannel)`

- `PixelCoordinate(NbrOfChannel)`

- `NormalizedAdcCharge(NbrOfChannel)`

For every detector (HPD, PMT, Silicon Tracker) a new class is inherited for providing all the informations. The last data member associates to every datablock the event it is belonging to and vice versa.

Objects of type `Event` have as persistent data members the number of the event and the association to all the data belonging to them:

- `EventNumber`

- `ooRef(HpdBlock) hpdBlock[] <-> event :  propagate(delete);`

- `ooRef(PmtBlock) pmtBlock[] <-> event :  propagate(delete);`

and methods to compute physical characteristic of the event:

- `nbrOfTrack()`

- `nbrOfPhoton()`

- `cherenkovAngle()`

In case an `Event` is deleted all the corresponding `DataBlocks` are deleted thanks to `propagate(delete)`.

Figures B.2 and B.3 show the structure of the two containers through the output of Objectivity database browser `ootoolmgr`.

All the databases are stored on a disk connected to a PC with Linux Red Hat 5.1 as operative system, currently supported by Objectivity.

A database management system application has been built using the Objectivity/C++ library to work on the federated database: BOSS (a Beam Object Storage System). With BOSS it is possible, through a simple ASCII interface, to:
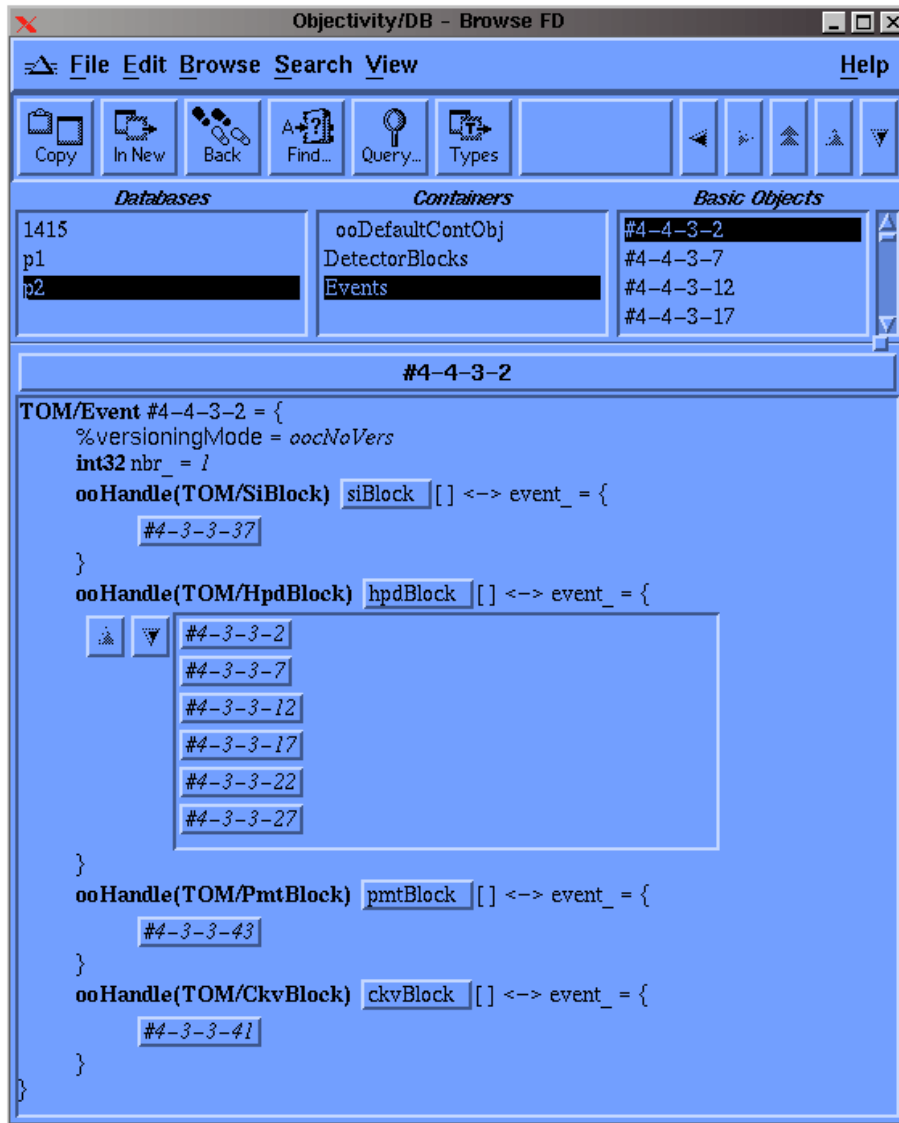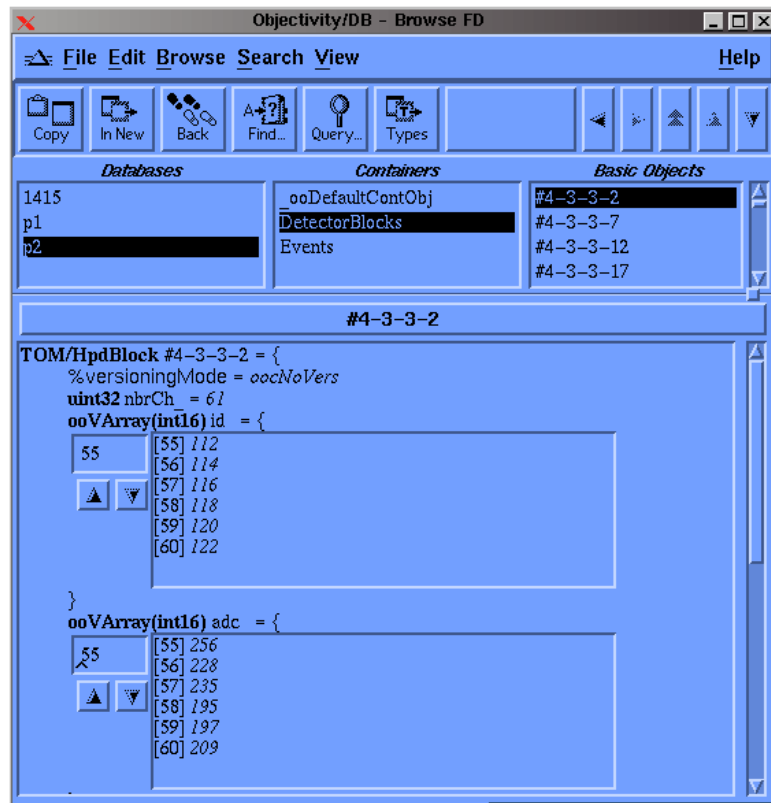
Figure B.2: Structure of the `EventContainer`

Figure B.3: Structure of the DataBlockContainer

- Read raw data files and save data in the federated database;

- Have data accessible from everywhere;

- Have the possibility to do a pre-analysis;

- Produce HBOOK files for the final analysis;

Data are accessible from everywhere thanks to the Objectivity Advanced Multithreated Server (AMS), which is an alternative to the Network File System and to the Microsoft Windows Network.

AMS runs on the Linux machine where the disk for storage is installed. BOSS can run on every machine with Objectivity installed (all CERN official nodes). In this way BOSS reduces the needs to be connected on the machine used for the test beam, where currently the raw data files are stored. It offers the possibility to have data with a pre-built structure available from everywhere even on a cheap mass storage system as the hard disk of a PC.

Bibliography

[1] Rene Brun and Fons Rademakers, ROOT - An Object Oriented Data
    Analysis Framework, Proceedings AIHENP'96 Workshop, Lausanne,
    Sep. 1996,
    Nucl. Inst. & Meth. in Phys. Res. **A 389** (1997) 81-86.
    See also http://root.cern.ch/.

[2] LHCb week; Data Handling Meeting (15 September 1998).